

SPIN DYNAMICS AND OPTICAL NONLINEARITIES IN LAYERED GaSe AND
COLLOIDAL CdSe NANOCRYSTAL QUANTUM DOTS

By

Yanhao Tang

A DISSERTATION

Submitted to
Michigan State University
in partial fulfillment of the requirements
for the degree of

Physics – Doctor of Philosophy

2017

ABSTRACT

SPIN DYNAMICS AND OPTICAL NONLINEARITIES IN LAYERED GaSe AND COLLOIDAL CdSe NANOCRYSTAL QUANTUM DOTS

By

Yanhao Tang

In this thesis, we studied spin dynamics, optical nonlinearity and the optical Stark effect in bulk GaSe, mono- and few-layer GaSe, and colloidal CdSe nanocrystal quantum dots (NQDs), respectively.

Control of the spin has been a long-term goal due to its potential applications in quantum information processing. Candidates for spintronics should have a long spin lifetime and allow for generation of a high initial spin polarization. GaSe caught our attention due to its orbitally nondegenerate valence bands, which are in contrast to the degenerate heavy and light hole valence bands in conventional III-V and II-VI semiconductors, like GaAs and CdSe. With time- and polarization-resolved photoluminescence, we demonstrated the generation of initial spin polarization as high as 0.9 followed by bi-exponential spin relaxation at 10 K (~ 30 ps and ≥ 300 ps), owing to such orbitally nondegenerate valence bands in GaSe. We also directly revealed the initial spin and population relaxation as transitions from triplet excitons to singlet excitations via spin-flip of the electron or hole.

Contrary to semiconductor transition metal dichalcogenides, MX_2 ($\text{M}=\text{Mo}, \text{W}$; $\text{X}=\text{S}, \text{Se}, \text{Te}$), GaSe is a direct band gap semiconductor in bulk, but transforms to an indirect band gap semiconductor in a monolayer as the maximum of the valence band is shifted away from the Γ point. Associated with such a valence band in monolayer GaSe, ferromagnetism has been predicted upon hole doping due to a strong electronic exchange field. To study the electronic structure of GaSe in mono- and few-layer GaSe, we measured layer- and frequency-dependent second-harmonic generation (SHG) in GaSe from monolayer to ≥ 100 layers and determined a second-order optical nonlinearity $\chi^{(2)}$ in the multi-slab system. We found reduced a $\chi^{(2)}$ in GaSe with thickness $\lesssim 7$ layers, tentatively attributed to the predicted increase in the band gap.

How quantum confinement affects the light-matter interaction in colloidal CdSe nanocrystal quantum dots (NQDs) has been a long-standing puzzle. The effective mass approximation (EMA) with $k \cdot p$ method has been successful in describing the energies of size-dependent optical transitions and the fine structures of the lowest-energy excitons. However, in contrast to the EMA's prediction of a nearly size-independent oscillator strength of the lowest-energy exciton, numerous experimental studies reported strongly reduced oscillator strength in CdSe NQDs as the size decreases, and failed to give an explanation. We developed a method based on the optical Stark effect to extract the oscillator strength of the lowest-energy excitons in semiconductor nanocrystals, and demonstrated a nearly constant oscillator strength from 6.7 nm to 2.5 nm, consistent with the prediction of the EMA. The optical Stark effect has been used as a method of transiently manipulating the spin. With circularly polarized off-resonant pump, we achieved an energy splitting of ~ 9 meV between transitions with different helicities, corresponding to an effective magnetic field of 110 T.

In this thesis, I will first introduce the background for all the optical studies, and then talk about the optical techniques before discussing the three projects mentioned above.

Copyright by
YANHAO TANG
2017

ACKNOWLEDGEMENTS

The time in an ultrafast lab seems to be gone ultrafastly. I can still remember my fresh moment as a graduate student that I tried to clean optics without knowing anything about the coating and John immediately stopped me and showed me the right way, which seems like yesterday.

I would like to greatly thank my advisor, John A. McGuire, for his continuous support and guidance from day one. When I had any questions or stupid ideas, I could just walk into his office and have a discussion with him. I very appreciate that John has trained me as an independent physicist. John gave me a lot of freedom and trust for projects, as well as research assistantship support. He let me choose the project I am interested in and design the experiments. He encouraged me to think of ideas and discussed with me about how practical these ideas are. Writing is one of my weaknesses. He has spent enormous time in revising my manuscripts, from which I have learnt how to express a story scientifically. His enthusiasm and commitment towards science, his extreme honesty to the data, and his willing to help colleagues and students are ones of his characteristics that have deeply influenced me. I also would like to thank Chih-wei Lai, who also has co-directed and financially supported me for a while. Working with Chih-wei has made my research areas and skills more diversified. His high standards and tough styles for students have definitely boosted my growth as a physicist.

My life of graduate school could have not been smooth if without help from graduate students and postdoctors. I would like to give special thanks to Tung-wu Hsieh for his generousities in sharing his rich research experience with GaSe when I took over the projects from him, even though he had left Chih-wei's group at that time. The manpower from Wei Xie, especially working with me on a 24 hour schedule, helped me to speed up the spin studies of GaSe. Our pre-experimental discussions saved me a lot of time from unnecessary experiments. Shunhao Xiao, a good talker and physicist, shared a lot about his doctoral experience and physics knowledge, and enlightened me about how to be a productive graduate student. Feng-kuo Hsu helped a lot for blending me in Chih-wei's lab and shared his technique experiences, particularly about the optical polarization

control. The routine Friday dinners with Shunhao, Tung-wu, Yung-hsiu, Feng-kuo in my initial years were undoubtedly the happy hours, relieving me from graduate-school pressure. Cheng Sun, aka the littlefinger in “a song of ice and fire”, told me a lot of living skills in the USA, as well as walked me through the transient absorption setup. Florian Figge, a team player and a cool biker, taught me how to use the home-built NOPA. I would like to thank my chemistry colleagues from Prof. Rémi Beaulac’s lab, Poulami Dutta, Chenjia Mi, Mersedeh Saniepay and Zhihui Liu, for the knowledge of colloidal growth and their generousities about samples and time of instruments. I would like to thank Reza Loloee, who gave me many helps in AFM measurements and substrate preparation. I would like to thank all my friends in Michigan. Without them, my life here will be boring and colorless.

I am truly indebted to my wife, Qin Yuan. She gave up her job in a good hospital and came to the USA to be with me and give me support. I could not so easily get through the frustrations and struggles in graduate school without her comfort and encouragement. I would like to thank my parents, who give me total freedom to choose what I like as my career and believe that I can do it well.

TABLE OF CONTENTS

LIST OF TABLES	x
LIST OF FIGURES	xi
CHAPTER 1 INTRODUCTION AND BACKGROUND	1
1.1 Introduction to layered materials	1
1.2 Electronic structure of bulk GaSe and optical selection rules	3
1.3 Introduction to colloidal nanocrystals	7
1.4 Electronic structure of colloidal CdSe nanocrystal quantum dots and optical selection rules	8
CHAPTER 2 OPTICAL TECHNIQUES	13
2.1 Transient absorption	13
2.1.1 Setup	13
2.1.1.1 BBO OPA	15
2.1.1.2 Detection schemes: high-speed CCD and photodiode	16
2.2 Upconversion photoluminescence	17
2.2.1 Setup	18
2.2.2 Detection scheme: Galvanometer mirror	19
2.3 Time-correlated single photon counting	20
2.4 Cryogenics	21
2.4.1 Continuous flow optical cryostat	21
2.4.2 Closed-cycle optical cryostat	22
CHAPTER 3 EXCITON SPIN DYNAMICS IN GaSe SUB- μm THICK SLABS	24
3.1 Introduction	24
3.2 Experimental methods	25
3.2.1 Sample preparation and thickness characterization	25
3.2.2 Time- and polarization-resolved photoluminescence	26
3.2.2.1 Setup	26
3.2.2.2 Pulse train picker based on acousto-optic modulator	27
3.2.2.3 Power and polarization control based on liquid crystal devices	28
3.2.3 Polarization analysis	29
3.3 Near-unity generation of optical spin polarization in GaSe	30
3.3.1 Polarization-resolved photoluminescence at room temperature	32
3.3.2 Polarization-resolved photoluminescence at cryogenic temperature	35
3.4 Spin dynamics at different excitation energies	38
3.5 Mechanism of spin relaxation in GaSe	43
3.6 Conclusion	46

CHAPTER 4	DIRECT OBSERVATION OF TRANSITIONS FROM TRIPLET TO SINGLET EXCITONS	47
4.1	Introduction	47
4.2	Luminescence emerging on the edge	49
4.3	Time-resolved edge photoluminescence	51
4.4	Discussion	55
4.5	Conclusion	56
CHAPTER 5	SECOND-ORDER OPTICAL NONLINEARITY IN ATOMICALLY THIN GaSe CRYSTALS	57
5.1	Introduction	57
5.2	Experimental method	58
5.2.1	Sample exfoliation and characterization	58
5.2.2	SHG setup	60
5.3	Calculation of reflected SHG in a multilayer system	62
5.4	Power- and polarization-dependent SHG	66
5.5	Layer-dependent SHG with 785 nm excitation	67
5.6	Frequency-dependent SHG	68
5.7	Conclusion	70
CHAPTER 6	THE OPTICAL STARK EFFECT IN COLLOIDAL CdSe NQDS	72
6.1	Introduction	72
6.2	Background	74
6.2.1	A brief discussion of experimental size-dependence studies of $f_{1S_{3/2}1S_e}$	74
6.2.2	Why the optical Stark effect?	76
6.3	Experimental methods	78
6.4	The evidence of the optical Stark effect	80
6.5	Excitation-energy- and size-dependence of the optical Stark effect	81
6.6	Saturated differential absorption measurements	84
6.7	Helicity-selective optical Stark effect in colloidal CdSe NQDs	88
6.8	Conclusion	90
CHAPTER 7	SUMMARY	92
APPENDICES	94
APPENDIX A	EXFOLIATION OF GaSe	95
APPENDIX B	CALCULATION OF NUMBER OF TE AND TM MODES IN GaSe SLABS	97
APPENDIX C	EXCITATION-POWER-DEPENDENT EDGE AND FOCAL EMISSION	98
APPENDIX D	CALCULATION OF THE OPTICAL STARK EFFECT IN CDSE NQDS	99
BIBLIOGRAPHY	114

LIST OF TABLES

Table 3.1	Fitting parameters of a bi-exponential decay function, $\rho_c(t) = A_1 \exp(-t/\tau'_s) + A_2 \exp(-t/\tau''_s)$.	40
Table D.1	Calculated contributions to the $1S_{3/2}1S_e$ oscillator strength.	107

LIST OF FIGURES

Figure 1.1	The crystal structure of GaSe.	4
Figure 1.2	The schematic electronic structure of GaSe with (without) spin.	5
Figure 1.3	The crystal structure of wurtzite CdSe.	9
Figure 1.4	The schematic electronic structure and optical selection rules in wurtzite CdSe.	10
Figure 1.5	The schematic electronic diagram of CdSe NCs and fine structure of the $1S_{3/2}1S_e$ excitons.	12
Figure 2.1	The layout of the transient absorption setup.	14
Figure 2.2	The schematic of the double-pass collinear BBO OPA	15
Figure 2.3	The schematic electronic connections and timing of TA setup based on a fast CCD.	16
Figure 2.4	The layout of the upconversion photoluminescence setup.	18
Figure 2.5	The schematic electronic connection of the uPL setup based on the galvanometer scanning mirror (GM).	19
Figure 2.6	The schematic TCSPC setup and the operating principle.	21
Figure 2.7	Schematic of a continuous-flow optical cryostat (LT-3) from Advanced Research Systems.	22
Figure 2.8	Schematic of the closed-cycle optical cryostat (Montana Instruments, Cryostation).	23
Figure 3.1	AFM (a) and optical (b) microscope images of a GaSe slab with thickness of 90 nm.	26
Figure 3.2	The schematic setup for measurements of time- and polarization-resolved photoluminescence.	28
Figure 3.3	The schematic layout for a pulse-train picker based on an acousto-optic modulator.	29
Figure 3.4	The principle of a liquid-crystal variable retarder, showing molecule orientation with (a) and without (b) an applied DC voltage.	29

Figure 3.5	The orientation of modules for the power modulation (a), generation of circular polarization (b), and the polarization detection of the full Stokes parameters (c).	30
Figure 3.6	PL quantum efficiency.	31
Figure 3.7	Polarized time-integrated PL spectra at room temperature.	33
Figure 3.8	PL dynamics and polarization properties versus sample thickness at room temperature.	35
Figure 3.9	Time-integrated and polarization-resolved PL spectra.	36
Figure 3.10	Polarized PL dynamics.	37
Figure 3.11	Schematic of the model for exciton spin dynamics.	39
Figure 3.12	Polarized PL spectra of S540nm under optical excitation at 2.156 eV and 2.214 eV.	40
Figure 3.13	Polarized PL dynamics of S540nm under optical excitation at 2.156 eV and 2.214 eV.	42
Figure 3.14	Polarized time-dependent PL under optical excitation at 3 eV.	43
Figure 3.15	The initial spin decay time τ'_s versus the pump flux P (photoexcited density n) for 90 nm, 540 nm, and 1150 nm thick GaSe slabs.	46
Figure 4.1	Edge emission.	49
Figure 4.2	The schematic model of transitions between triplet (d_{\perp}) and singlet (d_{\parallel}) excitons.	52
Figure 4.3	PL dynamics of focal and edge emission.	53
Figure 4.4	Time-dependent FL (solid black line) and REL (solid red line) in a 200 nm-thick sample (S200nm).	55
Figure 5.1	Optical microscopic images showing results of exfoliation by different approaches.	59
Figure 5.2	AFM measurements of mono- and few-layer GaSe crystals.	60
Figure 5.3	The schematic layout of the SHG setup.	62
Figure 5.4	Nonlinear waves in the multilayer structure.	64
Figure 5.5	Power- and polarization-orientation-dependent SHG.	67

Figure 5.6	The thickness-dependent SHG for a fundamental wavelength of 785 nm.	68
Figure 5.7	Ratio between the reflected SHG power from GaSe nanoslabs and a thick BBO crystal.	71
Figure 6.1	Comparisons between the effective-mass approximation and previously reported results.	73
Figure 6.2	Illustration of the optical Stark effect of a two-level system.	77
Figure 6.3	Differential absorption dynamics of the OSE of 3.6 nm CdSe NQDs with 800 nm excitation.	79
Figure 6.4	Optical Stark effect for CdSe NQDs and co-linearly polarized Stark and probe fields.	81
Figure 6.5	Size-dependent optical Stark shift and oscillator strengths.	82
Figure 6.6	DA dynamics of the $1S_{3/2}1S_e$ peak of 3.6 nm CdSe NQDs.	85
Figure 6.7	Saturation measurements of the absorption cross section at 3.1 eV.	86
Figure 6.8	Ground-state absorption cross section (solid curves) for NQDs of different diameter.	87
Figure 6.9	The OSE for circularly polarized excitation.	90
Figure C.1	The frequency-dependent power-law fitting parameter of the REL and focal emission from S540nm at 10 K.	98
Figure D.1	Optical Stark slopes and oscillator strengths.	105
Figure D.2	$1S_{3/2}1S_e$ contributions to $1S_{3/2}1S_e$ optical Stark effect in CdSe NQDs.	108
Figure D.3	Size-dependent scaling factor γ relating the magnitude of the observed optical Stark shift of the $1S_{3/2}1S_e$ peak to the total oscillator strength of the $1S_{3/2}1S_e$ peak.	112

CHAPTER 1

INTRODUCTION AND BACKGROUND

1.1 Introduction to layered materials

There has long been interest in two-dimensional structures. The first famous example was the 2D electron gas achieved in Si-MOSFET in 1980 [1], where electrons were confined to the interface between oxide and Si via a gate voltage and the integer quantum hall effect (IQHE) was observed. Another example is oxide heterostructures, where novel states emerge at the oxide interfaces, e.g., interfacial superconductivity of SrTiO₃/LaAsO₃ [2].

The discovery of graphene [3], one-atom-thick carbon sheet, kicked off the boom in research in layered materials on the account of its fascinating physical properties [4] and provides a new platform of 2D physics. Graphene hosts massless Dirac electrons with mobility as large as 200,000 cm²/Vs [5, 6], which behave in unusual ways compared to ordinary electrons, as exemplified by the observation of an anomalous integer quantum Hall effect in graphene at half-integer filling factors [7, 8]. The light-matter interaction of graphene is several orders of magnitude stronger than conventional semiconductors. For example, graphene can absorb 2.3% of normally incident near-infrared light and 10-nm-thick GaAs can only absorb 1% near the band gap. However, although a small band gap can be opened via band engineering such as by hydrogenation [9], the gapless nature of intrinsic graphene around the Fermi level limits the potential applications in electronic switching devices. Besides graphene, people were also highly motivated to explore other layered materials, particularly those with a substantial band gap. Monolayer transition metal dichalcogenide (TMD) semiconductors (MX₂: M=Mo,W; X=S,Se,Te) have a direct band gap and exhibit interesting valley physics [10], in which the spin of carriers at the K and K' points of the Brillouin zone are locked to the valley index. The valley polarization can be optically generated by a circularly polarized optical pump [11, 12, 13] and controlled by the optical Stark effect [14, 15, 16]. The valley Hall effect has also been observed in MoS₂ transistors [17]. Compared

to quantum well structures and heterostructures embedded in a dielectric environment, monolayer and few-layer samples of layered materials have highly reduced dielectric screening, which largely enhances excitonic effects. For example, the exciton binding energy in monolayer WS₂ is about 0.3 eV [18]. However, the downside of MX₂ is low carrier mobility [19]. Given the zero band gap in graphene and poor carrier mobility in TMD semiconductors, phosphorus is attractive for its thickness-tunable band gap from 0.3 eV to 2 eV and high carrier mobility, which allows observation of the integer quantum Hall effect [20], albeit still much lower than graphene [21]. However, the instability of phosphorus makes it challenging for fabricating few-layer devices. There are other interesting layered materials, such as TMD metals (NbSe₂), which exhibits coexistence of superconductivity and charge density waves [22, 23], and ZrTe₅, which is predicted to be a 2D topological insulator with an interior band gap as large as 100 meV [24]. Searching for new family members of layered materials with interesting physical properties and potential applications is an important task in the field of 2D materials.

GaSe is one of the III-VI layered semiconductor compounds (MX: M=Ga,In; X=Se,S) and has a quasi-direct band gap around 2 eV. It is well known for its nonlinear optical applications, since it is one of the nonlinear optical crystals with the highest optical nonlinearities ($d_{22}=54\pm 10.8$ pm/V), has extremely low absorption in a wide wavelength range from 0.65 to 18 μm [25, 26], and has a large birefringence that permits phase-matching for wavelengths from 1 to 18 μm . Using difference-frequency generation (DFG) in GaSe, people have demonstrated coherent THz radiation in a wide wavelength range, which includes intense THz fields exceeding 100 MV/cm with tunable center frequency from 10 to 72 THz [27] and continuously tunable frequency from 0.08 to 5.2 THz and from 7.8 to 111 THz [28]. However, the downside is that GaSe is a soft material with (100) cleavage plane, which makes it hard to cut and polish in any other planes [26], a necessity for many nonlinear optical applications.

Earlier studies suggested that a high degree of optical orientation in GaSe could be achieved under nearly resonant excitation at low temperatures. Using steady-state measurements and the Hanle effects, Gamarts et al. [29, 30] demonstrated optical orientation and alignment of excitons

in GaSe by showing luminescence with circular or linear polarization above 90% under circularly or linearly polarized optical excitation *in resonance* with direct excitons at cryogenic temperatures. However, given the carrier lifetime of ~ 16 ps, such a high degree of linear polarization of the emission suggests that the coherence time between the states $|1, +1\rangle$ and $|1, -1\rangle$ (see the insert of Fig. 1.1) can be as long as 160 ps, which is much longer compared to optical dephasing times in other systems, such as GaAs [31] and its quantum wells [32]. This raises questions about the source of the emission, which might be the Raman signal of the resonant excitation. Time-resolved studies (Chap. 3,4) are needed to shine light on the questions like how much spin polarization can be generated, how long the spin can be maintained, and what the spin-flip mechanism is.

Recently, physics in 2D materials with broken inversion symmetry has drawn a lot of interest. For example, inversion-symmetry breaking in MoS₂ lifts the spin degeneracy of the maximum of the valence band at the K or K' points, which can lead to interesting valley physics as mentioned above. Although ϵ -GaSe is non-centrosymmetric regardless of the thickness, the uppermost valence band (UVB) maximum in bulk ϵ -GaSe is at the Γ point where the spin states remain degenerate. However, as GaSe goes to mono- and few-layer regime, quantum confinement can dramatically modulate its physical properties. Theoretical studies [33, 34, 35] reveal a direct-to-indirect band-gap transition, with the maximum of the UVB shifting away from the Γ point and a Mexican-hat-like UVB forming around the Γ point. There could interesting phenomena associated with such UVB, like the predicted ferromagnetic ground state modulated by hole doping [36]. In Chap. 5, we will utilize second-harmonic generation as a probe to study the thickness-tunable electronic structure.

1.2 Electronic structure of bulk GaSe and optical selection rules

The structure of GaSe is shown in Fig. 1.1. In a single layer, two Ga sublayers are sandwiched by two Se sublayers. The bonding within each layer is covalent. The bonding between neighboring layers is primarily of van de Waals type with a component of ionic-covalent character, which

makes the electronic structure three-dimensional [37, 38]. Compared to conventional II-VI (III-V) semiconductors without extra electrons, the excess electrons of GaSe (III-VI) are compensated by the Ga-Ga bonding (cation pairs) and a typical semiconductor band structure forms (the valence bands are fully filled) [39]. Distinguished by different stacking orders, there are four polytypes of GaSe: γ -, ϵ -, δ - and β -GaSe. All polytypes of GaSe break inversion symmetry except β -GaSe crystals with an even number of layers.

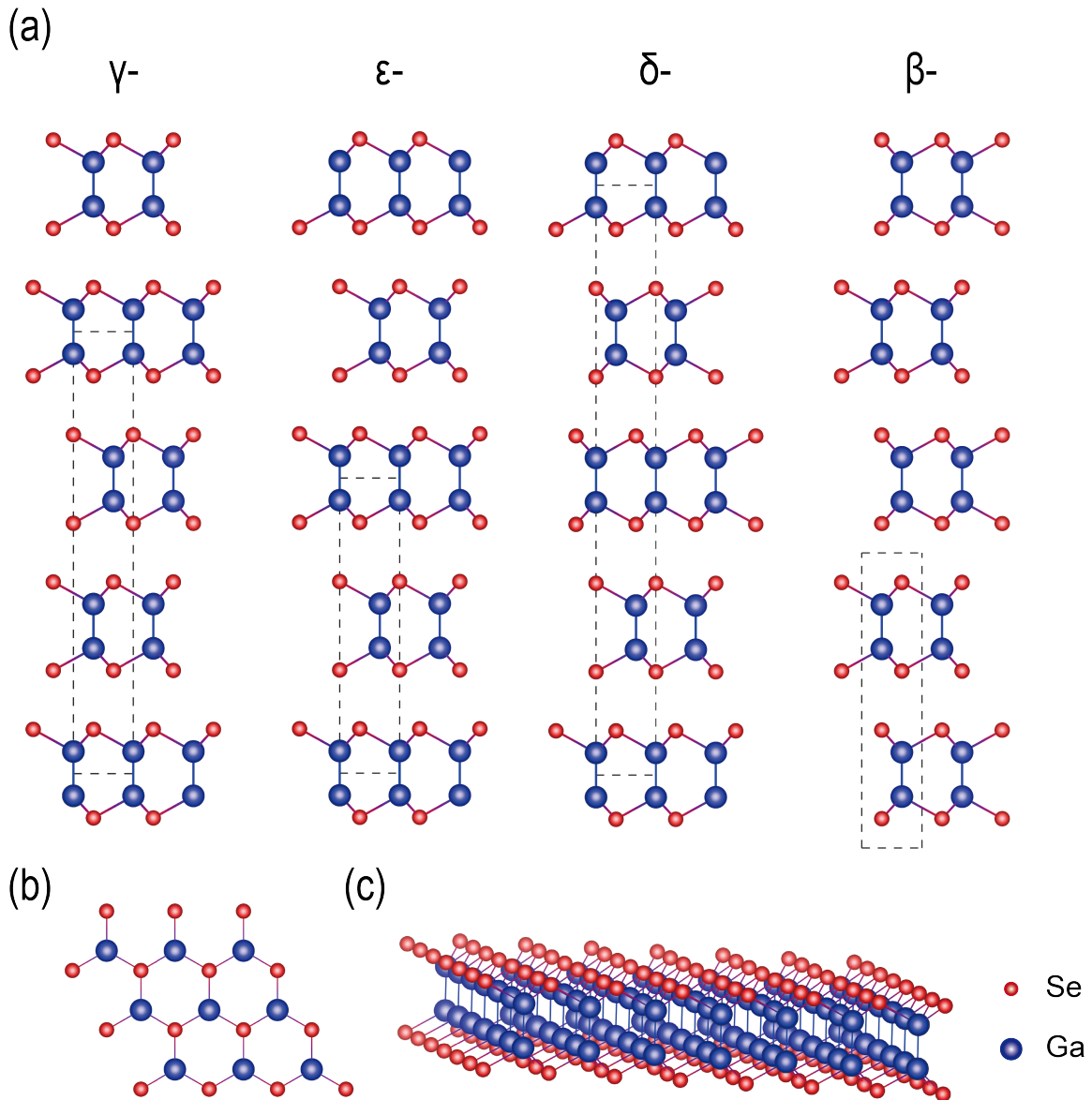


Figure 1.1 **The crystal structure of GaSe.** (a) The side-view of γ -, ϵ -, δ - and β -GaSe. The dashed squares represent unit cells. Top-view (b) and side-view (c) of monolayer GaSe.

Early research focused on understanding the electronic structure of GaSe. Fig. 1.2 shows a schematic band structure of bulk ε -GaSe. It has been widely accepted that GaSe is an indirect-gap semiconductor, but one in which the indirect band gap (the Γ point of the valence band to the M point of the conduction band) is just 10-20 meV lower than the direct band gap at the Γ point [40, 41, 42, 43, 44]. The lowest conduction band (LCB) and uppermost valence band (UVB) near the Γ -point are derived primarily from Ga s -like and Se p_z -like orbitals and have respectively Γ_4 and Γ_1 symmetry. The valence bands are split by crystal-field anisotropy and spin-orbit interaction, leading to two bands with Se p_x, p_y symmetry about 1.2 and 1.6 eV below the UVB maximum.

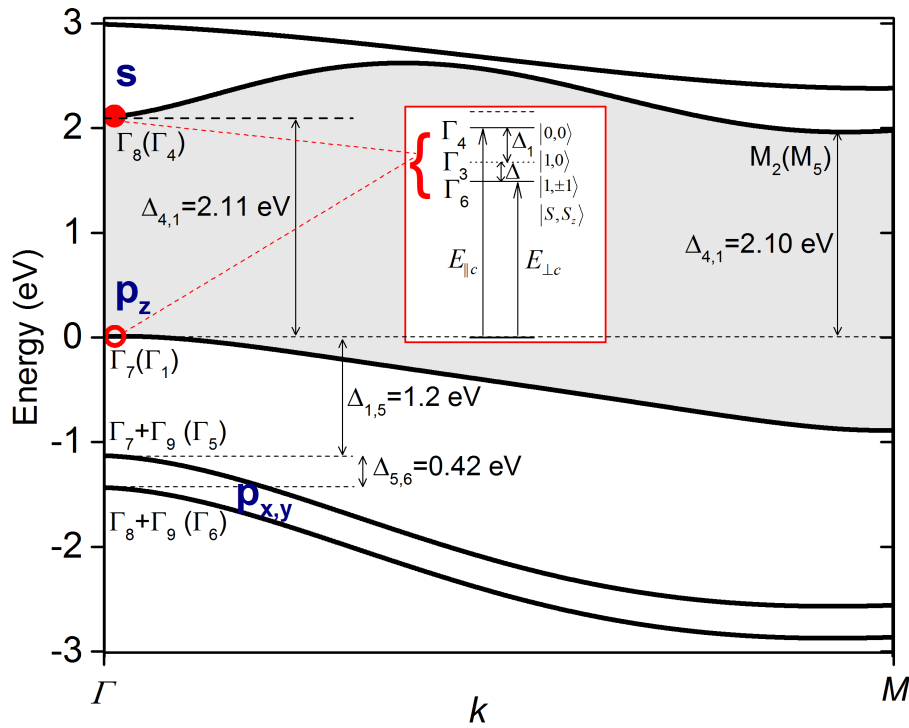


Figure 1.2 **The schematic electronic structure of GaSe with (without) spin.** The group-theoretical symbols (Γ_n and $n=1,4\dots$) are taken from [45]. The symbols with (without) parenthesis represent states with (without) spin. Inset are the optical selection rules for transitions at the Γ point.

The following discussion of exciton fine structure and optical selection rules are mainly based on the work of Mooser, et al. [38]. The strongly anisotropic crystal structure leads to correspondingly anisotropic optical properties. The polarization vectors $\vec{E} \parallel c$ and $\vec{E} \perp c$ belong to the Γ_4 and Γ_6 representations, respectively. Disregarding spin, the transition between UVB (Γ_1 representa-

tion) and LCB (Γ_4 representation) generates an excitation belonging to the $\Gamma_1 \times \Gamma_4$, which belongs to the Γ_4 representation of D_{3h} . Therefore, the direct transition $\Gamma_1 \rightarrow \Gamma_4$ is optically allowed only for $\vec{E} \parallel c$.

Taking into account spin, the representations of the LCB, UVB, and $p_{x,y}$ -like valence bands respectively become the Γ_8 , Γ_7 , $\Gamma_7+\Gamma_9$, and $\Gamma_8+\Gamma_9$ representations of the double group \bar{D}_{3h} (see Fig. 1.2). A complete accounting of the optical response requires an excitonic (two-particle) picture. To a first approximation, one can regard band-edge excitons derived from carriers only in the conduction band and the UVB. The direct transition from the electronic ground state to an electron (Γ_8) and hole (Γ_7) in an s -like (Γ_1) direct-gap exciton state yields an exciton belonging to the following (degenerate) representations [38, 46, 29, 30, 47]:

$$\Gamma_X^{(s)} = \Gamma_7 \times \Gamma_8 \times \Gamma_1 = \Gamma_4 + \Gamma_3 + \Gamma_6, \quad (1.1)$$

where Γ_4 is a pure spin singlet, and Γ_3 and Γ_6 are pure spin triplet states (see the insert of Fig. 1.2). As $\vec{E} \parallel c$ belongs to the Γ_4 representation, the Γ_4 exciton can be excited by light with $\vec{E} \parallel c$. However, even though $\vec{E} \perp c$ belongs to the Γ_6 , the Γ_6 exciton requires a spin-flip of the excited electron and the dipole operator has no effect on the spin, which makes the oscillator strength of the Γ_6 exciton zero.

To account for the nonvanishing absorption of the band-edge exciton (Γ_6) for $\vec{E} \perp c$, we need to consider the valence-band mixing between the UVB (Γ_1) and the lower $p_{x,y}$ -like valence band (Γ_5) due to spin-orbit coupling. After accounting for such valence-band mixing, the s -type band-edge excitonic wavefunctions become approximately [38]

$$\begin{aligned} \Gamma_4 &= |0,0\rangle + \alpha_4 |1,\pm 1\rangle, \\ \Gamma_3 &= |1,0\rangle, \\ \Gamma_6 &= |1,\pm 1\rangle + \alpha_6 |0,0\rangle, \end{aligned} \quad (1.2)$$

where $|S, S_z\rangle$ is used to label states, $|0,0\rangle$ represents the singlet exciton, and $|1,0\rangle$ and $|1,\pm 1\rangle$ represent the triplet excitons. Using Δ_{SO} measured by Sasaki et al. [48, 49], the coefficients

$\alpha_4 \approx \alpha_6 \approx (\Delta_{SO}/E_{BA}) \approx (0.44 \text{ eV}/1.27 \text{ eV}) \approx 0.35$. The Γ_5 state is mixed into the UVB at about the 10% level, consistent with the ratio of the oscillator strengths (absorbance) of $\vec{E} \perp c$ and $\vec{E} \parallel c$. The upper level Γ_4 corresponds approximately to a total exciton spin $S = 0$ and experiences a splitting from the Γ_3 and Γ_6 states of $\Delta_1 \approx 2 \text{ meV}$ because of electron–hole exchange [38]. The states Γ_3 and Γ_6 correspond approximately to a total exciton spin $S = 1$, and $S_z = 0$ and ± 1 are nearly degenerate (energy splitting $\Delta \approx 0$). These states are thus labeled by the indices 0 and ± 1 . The Γ_4 state still can be excited by light with $\vec{E} \parallel c$. For optical excitation with wave vector $\vec{k} \parallel c$, Γ_6 ($S_z = \pm 1$) states can be excited by circularly polarized light with $\vec{E} \perp c$, whereas the Γ_3 state is optically inactive [29, 30].

1.3 Introduction to colloidal nanocrystals

A natural progression from two-dimensional systems is to reduce the dimensions further, which leads eventually to a zero-dimensional system, quantum dots. Quantum dots were discovered as CuCl nanocrystals in glass and alkali-halide matrices [50, 51, 52] and colloidal CdS nanocrystals in aqueous solution [53, 54, 55]. There are generally two kinds of approaches to synthesizing quantum dots. One is via epitaxial techniques, such as self-assembled growth [56] and lateral confinement in 2D heterostructures [57]. The other is via wet chemical techniques [58, 59], typically a hot-injection method, i.e., introduction of organometallic precursors into an organic solvent at a high temperature by rapid injection, initially developed by C. B. Murray et al. [60]. We will focus on quantum dots synthesized by the latter method, referred to as colloidal nanocrystal quantum dots (NQDs), which can generally exhibit larger quantum confinement effects, compared to epitaxial quantum dots.

Owing to the great tunability of quantum confinement and various choices of materials, colloidal NQDs have been viewed as promising building blocks for various novel devices and materials. Despite ultrafast multi-exciton Auger recombination, optical gain and stimulated emission have been demonstrated in the multi-exciton region in colloidal NQDs [61, 62], which suggests

colloidal NQDs as potential laser media with the advantages of tunable optical band gap and temperature insensitivity due to their highly discrete states. Efforts have been focused on suppressing multi-exciton Auger recombination [63] and pushing the lasing threshold to the single-exciton regime [64]. Colloidal NQDs have been studied as emitters for light-emitting diodes and successfully commercialized as TV displays. Colloidal NQDs have also been explored for other applications such as solar cells, field-effect transistors, and photodetectors [65].

NQDs are a test bed for studying physics in a three-dimensionally confined case, especially in a strong quantum confinement region that can not be reached by 2D systems. A key feature of colloidal NQDs is the discrete optical transitions, like transitions between atomic levels, which can be widely tuned by the quantum size effect. For example, the lowest-energy absorption peak of CdSe NQDs can be tuned from 660 nm to 320 nm [66]. The studies of the effects of quantum confinement on physical properties, such as the exciton energy [67, 68, 69] and the light-matter interaction [70, 66, 71, 72], will be discussed in details in Chap. 6. One interesting consequence of quantum confinement is the enhanced carrier-carrier Coulomb interaction due to the strong carrier-carrier overlap that leads to novel phenomena, such as large electron-hole exchange interaction [69], ultrafast non-radiative decay by Auger recombination, and multi-exciton generation by single high-energy photons [63].

1.4 Electronic structure of colloidal CdSe nanocrystal quantum dots and optical selection rules

In this section, I discuss the electronic structure and optical selection rules of colloidal NQDs using CdSe as a representative.

Before discussing the electronic structure of colloidal NQDs, let us first start with the electronic structure of bulk wurtzite CdSe, which belongs to the space group $P6_3mc$. The crystal structure is shown in Fig. 1.3 [73]. CdSe is a direct band gap semiconductor with the lowest-energy direct transition at the Γ point. The two electrons in the 5s orbital of Cd are given to Se to fill the 4p

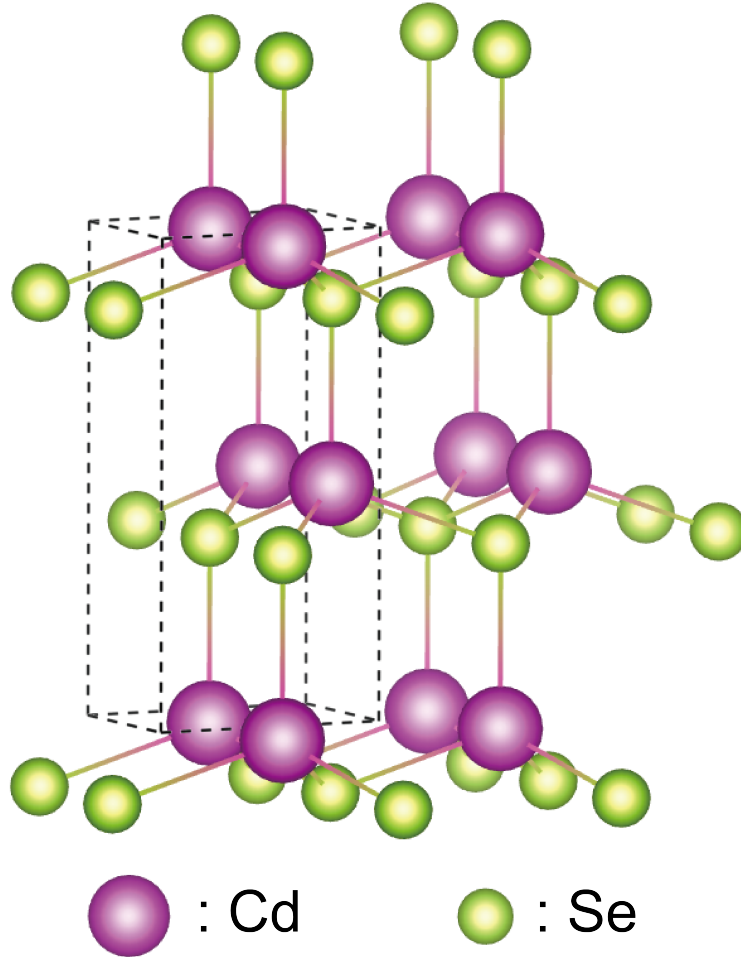


Figure 1.3 **The crystal structure of wurtzite CdSe.** The dashed lines represent the unit cell.

orbital. Thus the 4p orbital of Se forms the valence bands, and the 5s orbital of Cd forms the conduction band. In Fig. 1.4, we plot the schematic electronic structure of CdSe around the Γ point. Due to the spin-orbit interaction, the good quantum number is the total angular momentum $\vec{J} = \vec{l} + \vec{s}$ ($l = 1$, $s = 1/2$) where \vec{l} and \vec{s} are respectively the orbital and spin angular momenta. The upper two valence bands ($J = 3/2$) are known as the heavy (HH) and light hole (LH) band with $M_J = \pm 3/2$ and $\pm 1/2$, respectively. The degeneracy of HH and LH at the Γ point is lifted by the crystal field splitting of ~ 31 meV. Away from the Γ point, the HH and LH bands are further separated due to their anisotropic orbital overlap. The lowest valence band is separated from the LH band by 400 meV at the Γ point due to the spin-orbit interaction. As the conduction band is formed by s-like orbitals, it is just spin degenerate.

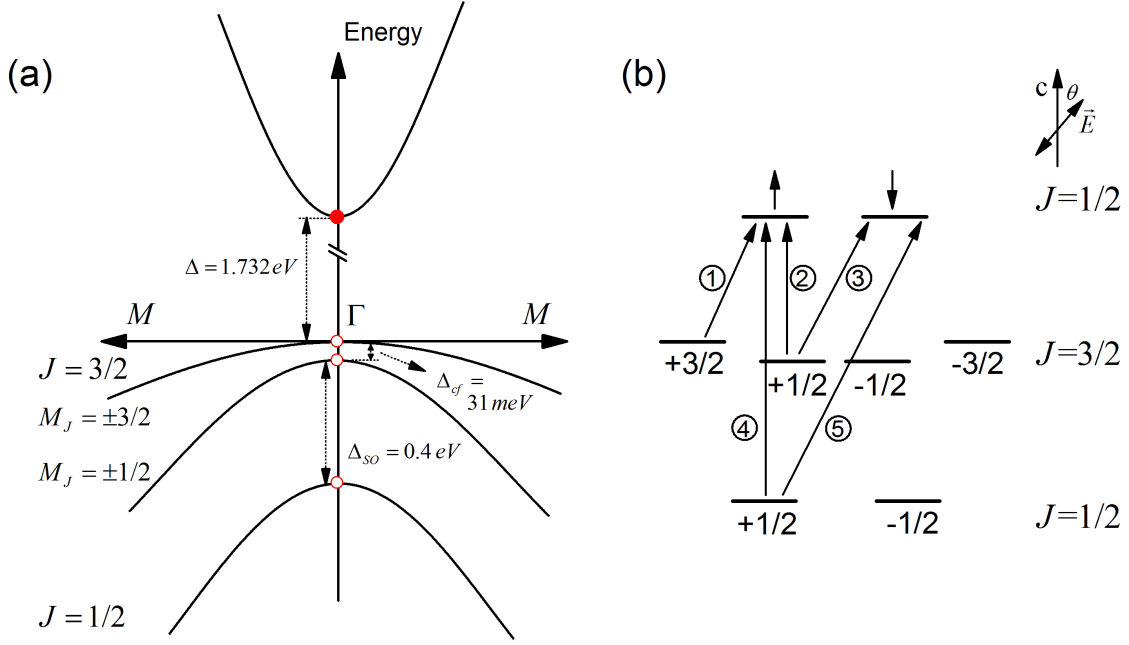


Figure 1.4 **The schematic electronic structure and optical selection rules in wurtzite CdSe.** (a) The schematic electronic structure of wurtzite CdSe at 300 K [74], just showing conduction and valence bands. (b) The circled numbers represent allowed transitions for linearly polarized electric field \vec{E} with an angle θ to the c axis, without showing the conjugate transitions, e.g., $-3/2 \rightarrow \downarrow$.

In Fig. 1.4 (b), we show the possible direct transitions from the three valence bands to the conduction band at the Γ point with optical excitation by light polarized linearly at an angle θ relative to the c axis. The corresponding Bloch functions are

$$\begin{aligned}
 u_{\uparrow}^c &= S \uparrow, & u_{\downarrow}^c &= S \downarrow, \\
 u_{3/2,3/2}^v &= \frac{1}{\sqrt{2}}(X + iY) \uparrow, & u_{3/2,-3/2}^v &= \frac{i}{\sqrt{2}}(X - iY) \downarrow, \\
 u_{3/2,1/2}^v &= \frac{i}{\sqrt{6}}[(X + iY) \downarrow - 2Z \uparrow], & u_{3/2,-1/2}^v &= \frac{1}{\sqrt{6}}[(X - iY) \uparrow + 2Z \downarrow], \\
 u_{1/2,1/2}^v &= \frac{1}{\sqrt{3}}[(X + iY) \downarrow + Z \uparrow], & u_{1/2,-1/2}^v &= \frac{i}{\sqrt{3}}[-(X - iY) \uparrow + Z \downarrow].
 \end{aligned} \tag{1.3}$$

The transition probability is proportional to the squared magnitude of the transition momentum matrix element $|\langle f | \mathbf{e} \cdot \vec{p} | i \rangle|^2$, where $|i\rangle$ and $|f\rangle$ represent the initial and final states, \mathbf{e} is the unit vector of the polarization of the electric field, and \vec{p} is the momentum operator. As an example, the squared magnitude of the momentum matrix elements of the five transitions shown in Fig. 1.4

are given in Eq. 1.4.

$$\begin{aligned}
\left| \langle u_{3/2,3/2}^v | \mathbf{e} \cdot \vec{p} | u_{\uparrow}^c \rangle \right|^2 &= \left| \langle \frac{1}{\sqrt{2}}(X + iY) \uparrow | \mathbf{e} \cdot \vec{p} | S \uparrow \rangle \right|^2 = \frac{1}{2} |e_x \langle X | p_x | S \rangle - ie_y \langle Y | p_y | S \rangle|^2 \\
&= \frac{1}{2} |e_x - ie_y|^2 P^2 = \frac{1}{2} \cos^2 \theta P^2 \\
\left| \langle u_{3/2,1/2}^v | \mathbf{e} \cdot \vec{p} | u_{\uparrow}^c \rangle \right|^2 &= \frac{2}{3} \cos^2 \theta P^2 & \left| \langle u_{3/2,1/2}^v | \mathbf{e} \cdot \vec{p} | u_{\downarrow}^c \rangle \right|^2 &= \frac{1}{6} \sin^2 \theta P^2 \\
\left| \langle u_{1/2,1/2}^v | \mathbf{e} \cdot \vec{p} | u_{\uparrow}^c \rangle \right|^2 &= \frac{1}{3} \cos^2 \theta P^2 & \left| \langle u_{1/2,1/2}^v | \mathbf{e} \cdot \vec{p} | u_{\downarrow}^c \rangle \right|^2 &= \frac{1}{3} \sin^2 \theta P^2
\end{aligned} \tag{1.4}$$

where $P \equiv \langle X | p_x | S \rangle = \langle Y | p_y | S \rangle = \langle Z | p_z | S \rangle$ is the Kane interband matrix element.

The electronic structure of colloidal NQDs can naively be thought of in terms of particles in a three-dimensionally confined sphere with radius R and constant potential inside. There are three confinement regimes: the weak ($R \geq a_e, a_h$), intermediate (e.g. $a_h \leq R \leq a_e$), and strong confinement ($R \leq a_e, a_h$) regime where a_e and a_h are electron and hole Bohr radii. CdSe NQDs in an easily accessible size range usually are in the intermediate confinement regime. Generally, electrons are strongly confined by the potential barrier of NQDs and holes are mostly confined by the Coulomb potential created by the electrons [75]. As stated previously, the direct consequence of quantum confinement is the discrete states, which are illustrated in Fig. 1.5. J is no longer a good quantum number to describe electrons and holes. Instead, we have to take the angular momentum L of the envelope wavefunction into consideration. Now, the good quantum number is $\vec{F} = \vec{J} + \vec{L}$ and nL_F is used to label a state, where n is the number of the state with the same L and F . For example, for the highest-energy hole with $F = 3/2$, L can be 0 or 2 ($L = 1$ is not mixed due to its having the opposite parity), which leads to the hole state $1(S, D)_{3/2}$. To simplify the labelling, only the first letter is kept so that the state ends up as $1S_{3/2}$. To describe the excitonic structure, the good quantum number is $\vec{N} = \vec{F}_h + \vec{F}_e$. Taking the lowest exciton formed by the $1S_{3/2}$ and $1S_e$ states as an example, there are two series of excitons with $N = 1$ and $N = 2$, which are split due to the electron-hole exchange interaction. Due to the asymmetric crystal field and shape, the exciton states are further separated. We label the excitonic states as $M_N^{U,L}$ shown in Fig. 1.5, where M_N is the projection of N along the c axis, and U and L respectively mean upper and lower in energy. 2^U and 0^L are optically passive dark excitons, and 0^U , 1^U and 1^L are optically bright excitons. The

whole size-dependent oscillator strength of the $1S_{3/2} \rightarrow 1S_e$ transition is distributed within those excitons [69].

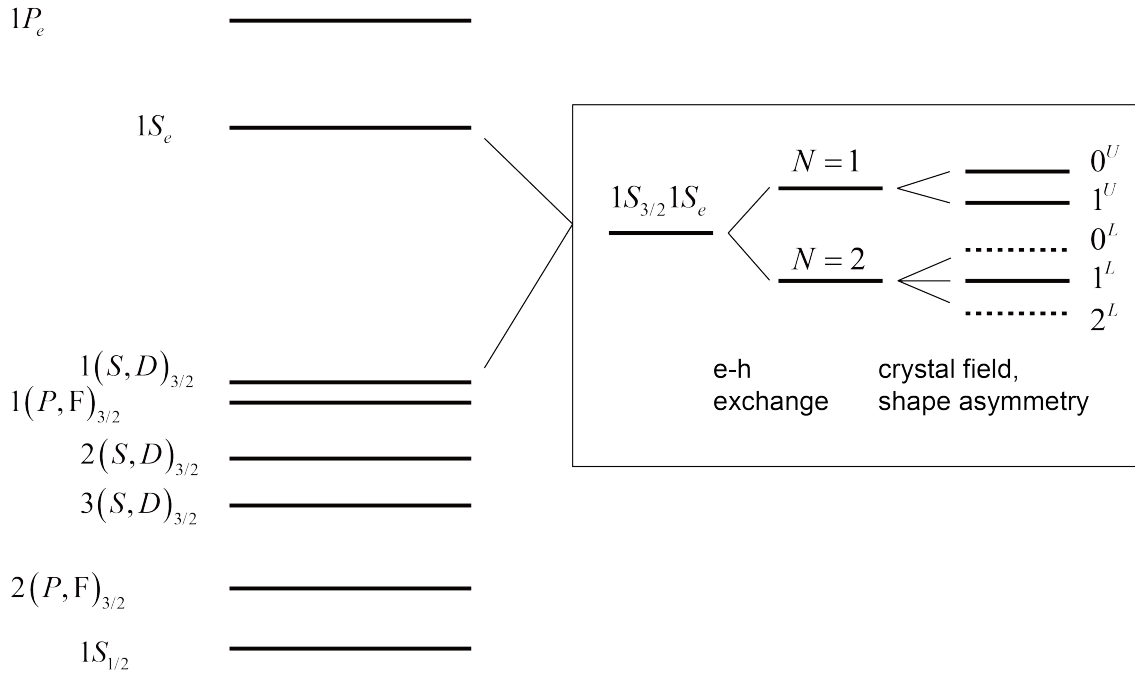


Figure 1.5 **The schematic electronic diagram of CdSe NCs and fine structure of the $1S_{3/2}1S_e$ excitons.** The dashed lines in the rectangle represent dipole-forbidden states, dark states.

CHAPTER 2

OPTICAL TECHNIQUES

2.1 Transient absorption

Femtosecond transient absorption is a well-established technique, which is used to reveal carrier dynamics and optical nonlinearities [76].

2.1.1 Setup

Fig. 2.1 shows the layout of the transient absorption setup, which consists of six modules. The Ti:sapphire laser source is from Spectra-Physics. The MaiTai provides an 80-MHz seed with a central wavelength of 800 nm for the Spitfire Pro amplifier, which is powered by the Nd:YLF laser with 527 nm output. (Empower, ~ 18 W). The output of the Spitfire Pro amplifier is ~ 4 W with a 1-KHz repetition rate, 100-fs time duration and horizontal polarization. In the the time-delay module, the 800 nm pulse is delayed by a retroreflector mounted on a delay stage (Newport ILS250CC). For the probe-generation module, the white light supercontinuum is generated by focusing about $1\mu\text{J}$ of the 800 nm light onto a 1 mm sapphire crystal and collimated by a parabolic mirror, thereby minimizing temporal dispersion over a wide spectral range. The intensity of the 800 nm is adjusted by a half-wave plate and a polarizer. The diameter of the WL is reduced by a factor of three via a telescope consisting of two concave mirrors. The WL is temporally compressed by a pair of prisms, which can minimize the arrival-time difference in the visible region and allow for blocking undesired frequencies. The beams into and out of the compressing prisms have different heights so that a pick-off mirror directs the WL to the next module. We generate a pump of the desired frequencies using a home-built OPA or just doubling the 800 nm output. Similar with the probe, the output of the OPA is also spatially reduced by a telescope consisting of lenses L3 and L4, and temporally compressed by a pair of prisms that also work as a spectral filter to get rid of undesired frequency, such as the signal and idler of the OPA. In the sample module, the pump is modulated

by an optical chopper (New Focus 3501 Optical Chopper) at a frequency of 500 Hz and transmitted through the sample. The collimated WL is focused into the sample with a parabolic mirror (PM2), re-collimated by another parabolic mirror (PM3), attenuated by a neutral density filter and finally focused on a monochromator (Princeton Instruments Acton SP150) configured with a 300 gr/mm grating ($\lambda_{\text{blaze}}=500$ nm) and a linear high-speed CCD with a typical sampling rate of 2327 lines per second (Hamamatsu S11155-2048-01) controlled by a driver circuit (Hamamatsu C11165-01).

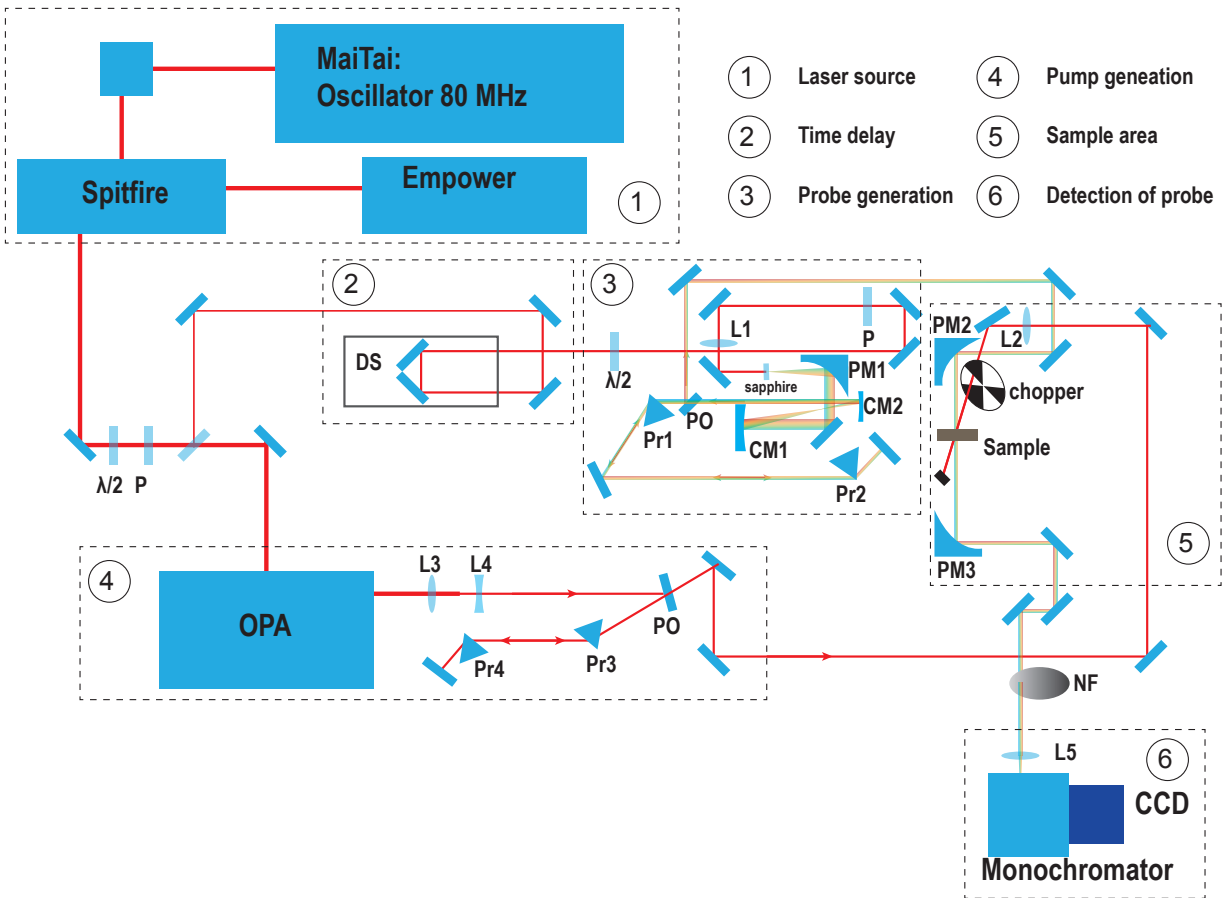


Figure 2.1 **The layout of the transient absorption setup.** The dashed rectangles represent the functional modules, labeled with numbers in circles. The focal lengths of lenses L1, L2, L3, L4, L5 are 100, ~ 300 , 150, -50, and 60 mm. The focal lengths of parabolic mirrors PM1, PM2, and PM3 are 2, 5, and 5 inch. The focal lengths of concave mirrors CM1 and CM2 are 250 mm and 50 mm. DS, Pr, PO, P, and NF represent delay stage, prism, pick-off mirror, polarizer, and neutral density filter.

source (several mW with large fluctuations, $\pm 20\%$) is generated, which is collimated by a concave mirror (CM2) and reflected through the same BBO (BBO1). For the second stage of amplification, another 800 nm beam (~ 600 mW) is collinearly and temporally (with T2) overlapped with the infrared beam. This generates stable signal and idler beams due to the gain saturation (typical power of 150 mW, $\pm 5\%$ over tens of seconds, almost no power drift over hours). Another BBO crystal (BBO2) is used to convert infrared to visible light via second-harmonic generation.

2.1.1.2 Detection schemes: high-speed CCD and photodiode

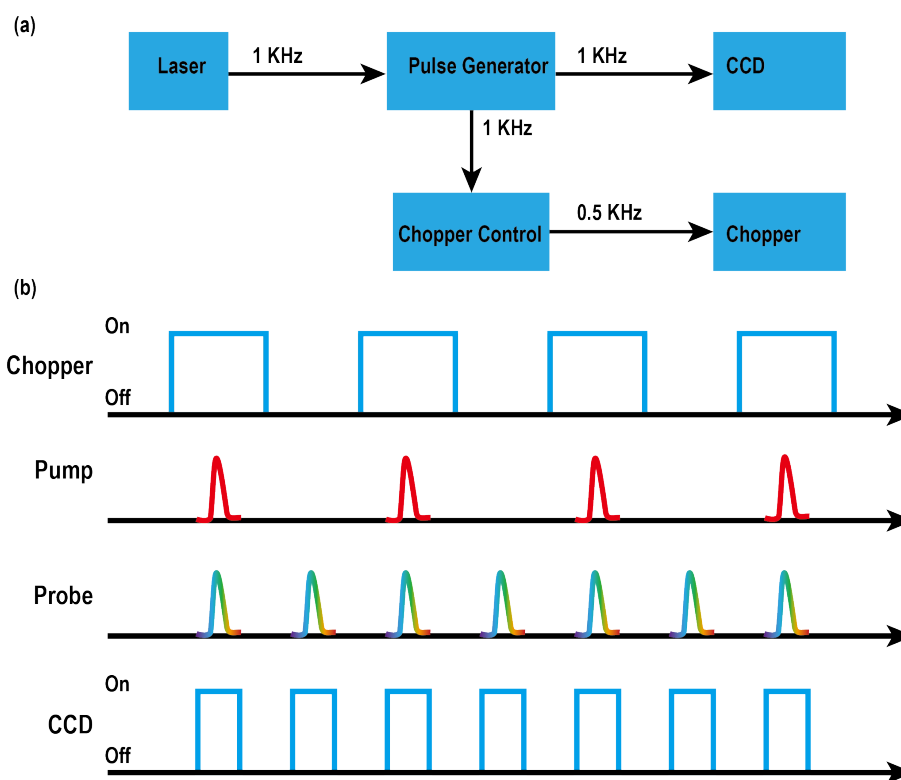


Figure 2.3 The schematic electronic connections and timing of TA setup based on a fast CCD.

To measure the transient absorption over a broad spectral region, we use a high-speed linear CCD array. As shown in Fig. 2.3, the 1 KHz sync signal from the laser is used to trigger the pulse generator (SRS DG535), which generates square waves at a frequency of 1 KHz. The output of the pulse generator is split into two channels: A trigger for the CCD and a reference for the optical

chopper controller (New Focus Model 3501) that generates a synchronized 500 Hz signal to drive the chopper.

To detect the transient absorption response at a single wavelength, especially in the infrared regime where the Si CCD is relatively insensitive, we use a Si (Thorlab, DET36A) or InGaAs (Thorlab, DET10D) photodiode coupled to a monochromator. The output of the photodiode is preamplified by an amplifier (Stanford Research System, SR240) and integrated by a boxcar integrator (SRS, SR 250). The integrated signal is finally acquired by a DAQ card (National Instruments). (This version of transient absorption is used in my early doctoral stage)

2.2 Upconversion photoluminescence

To study time-dependent photoluminescence with sub-picosecond resolution, we built a photoluminescence upconversion (uPL) setup, shown in Fig. 2.4. Compared to transient absorption, which is sensitive to various transitions, uPL is only sensitive to the band edge states. uPL is almost a background-free measurement, as other signals, such as the gate pulse, SHG of the gate pulse, and PL, can be spectrally filtered by the monochromator and filters. Upconversion is a sum-frequency process where two photons with different energies interact with a nonlinear material and generate a photon with energy equal to the sum of the two photons. In our setup, an intense 800 nm beam acts as a temporal gate and upconverts the PL to the ultraviolet region.

Optical Kerr gating (OKG) of photoluminescence is another method to achieve sub-picosecond resolution. The OKG method utilizes the transient birefringence created by intense linearly polarized light in otherwise non-birefringent materials, such as liquids, to modulate the transmission through a pair of orthogonally oriented polarizers between which the Kerr medium is placed [78, 79]. Compared to uPL, which, at a given angle of the upconversion crystal, can only upconvert a narrow spectral region determined by phase matching, OKG can acquire a broad spectrum all at once time and without tricky alignment of the nonlinear crystal. However, due to the finite extinction ratio of polarizers ($\sim 10^5$), the background PL is an issue for a 1 kHz laser system and

materials with PL lifetime $\tau_{PL} \geq 10^6 \tau_{gate}$, because ungated PL will lead to a high background signal.

2.2.1 Setup

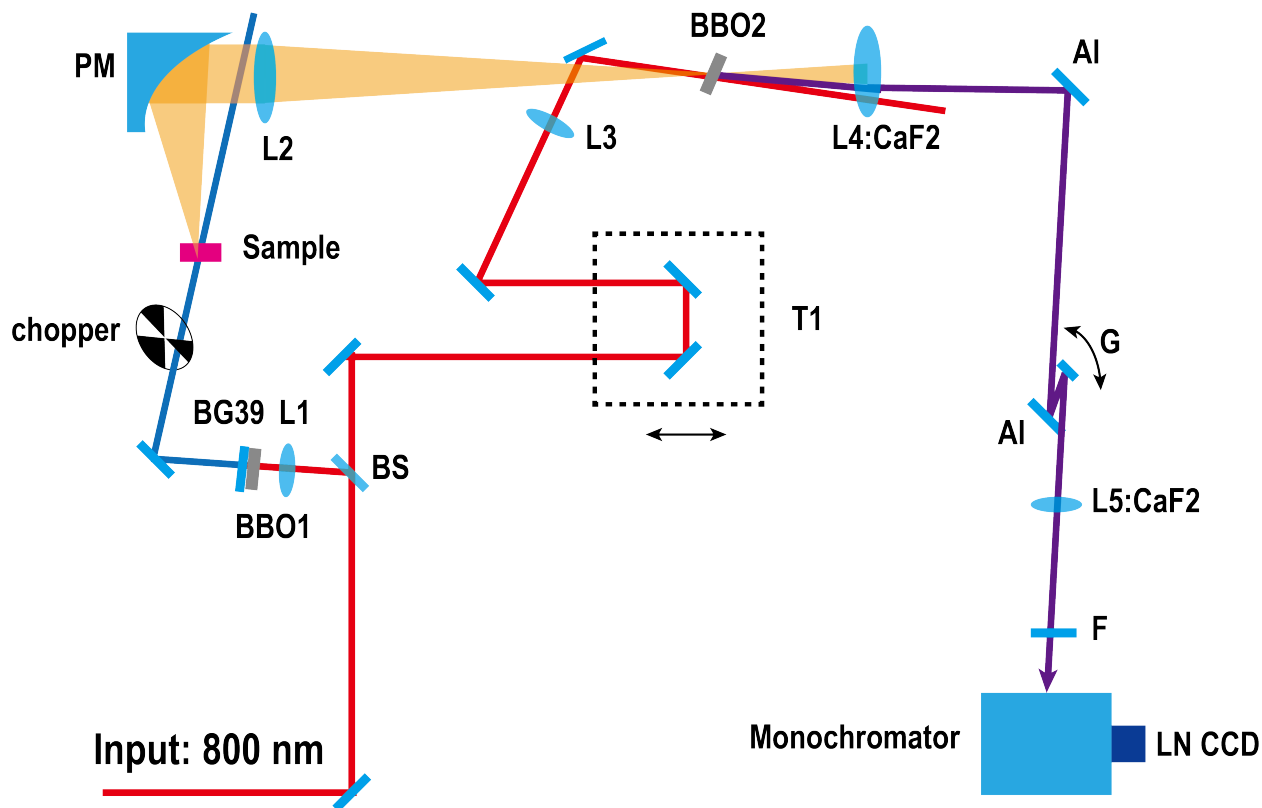


Figure 2.4 **The layout of the upconversion photoluminescence setup.** The real (a) and schematic (b) setup. The unlabeled mirrors are either silver or dielectric coated. Al represents aluminum-coated mirror. PM represents a parabolic mirror, with focal length of 100 mm. The lenses without special labels are made of BK7 glass. The focal lengths of L1, L2, L3, L4 and L5 are 100, 250, 200, 100 and 100 mm. The BS represents a beam splitter with splitting ratio of 50:50. F represents two short-pass filters (Thorlabs, FGUV11). BBO2 is oriented for sum-frequency generation by type-I matching.

In Fig. 2.4, we show the schematic of the uPL setup. The uPL setup is driven by the same 1 kHz laser system used in transient absorption. The input 800-nm beam (~ 700 mW) is split into two beams by a 50:50 beam splitter. One 800-nm beam is used to generate 400-nm excitation via SHG in a BBO crystal (BBO1) and is modulated by an optical chopper. The other beam is delayed

by a translation stage (Newport, ILS200CC) and upconverts the transient photoluminescence in another BBO crystal (BBO2, 2 mm thickness, $\theta=29.2$) via type-I phase matching. The transient uPL is collimated with a CaF₂ lens, directed to a galvanometer mirror (Thorlabs, GVS011) that oscillates about the horizontal axis normal to the beam propagation, and filtered by two bandpass filters (Thorlabs, FGUV11). The uPL is acquired by a liquid-nitrogen cooled CCD coupled to a 300 mm monochromator (Princeton Instruments, Model 300i).

2.2.2 Detection scheme: Galvanometer mirror

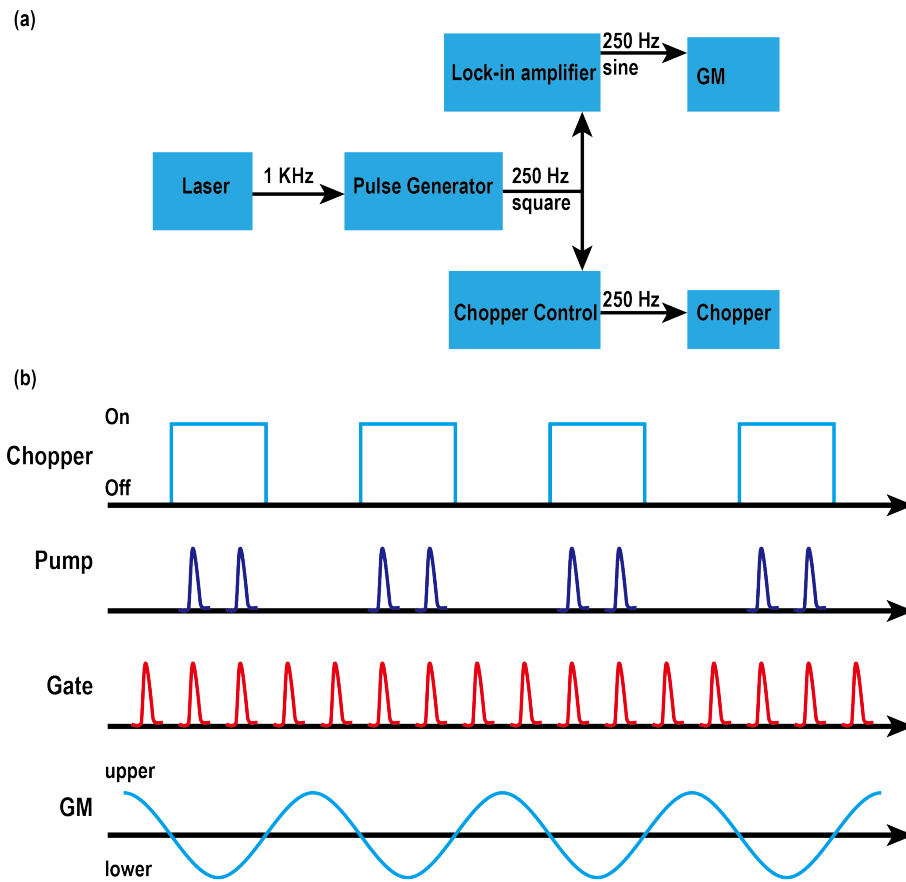


Figure 2.5 The schematic electronic connection of the uPL setup based on the galvanometer scanning mirror (GM).

Even though uPL is nominally a background-free measurement, there is always some background, especially light associated with the intense gate pulse. With the galvanometer scanning mirror, we

can spatially separate the signal associated with the simultaneous presence of pump and gate from the signal from the gate alone; these two signals are imaged on vertically separated rows of the CCD. The electronic connections are shown in Fig. 2.5. Due to the limited scanning frequency of the galvanometer mirror (Thorlabs, GM, GVS011), we choose a scanning frequency of 250 Hz, which is generated by the same pulse generator used in the transient absorption setup. The 250 Hz square waves from the pulse generator are split into two channels: One is sent to the lock-in amplifier (SR830 DSP, SRS) to generate a sine wave, as the driver of the GM can only accept sine waves. The other is sent to the optical chopper. As there are two uPL pulses within one chopper-on period and the CCD array consists of two horizontal rows, we adjust the phase of the pulse generator so that pulse pairs corresponding to, e.g., the pump being on, arrive at the GM at the same angular position of the GM.

2.3 Time-correlated single photon counting

Time-correlated single photon counting (TCSPC) [80] is a simple method for studying time-resolved photoluminescence with time resolution of ≥ 30 ps (mostly related to the limitations of the detector) and single-photon sensitivity. Compared to a streak camera, TCSPC generally exhibits lower dark count rates, higher quantum efficiency and much lower price. It is widely used to study nanosecond PL dynamics down to the single-particle level.

TCSPC is based on the repetitive time registration of single PL photons and a reference for the timing of the corresponding excitation pulse (Fig. 2.6(b)). In Fig. 2.6(a), we show the schematic TCSPC setup. The excitation is from a 405 nm pulsed diode laser with ~ 90 ps time duration and tunable repetition rate from 20 kHz to 20 MHz (Edinburgh Instruments EPL-405 diode laser), which is reflected to a transmissive objective by a dichroic mirror. The photoluminescence is collected by the same objective and focused onto the active sensing area (size $\sim 50 \mu\text{m}$) of an avalanche photodiode with ~ 50 ps time resolution (Micro Photon Devices PDM series cooled avalanche photodiode). The timing electronics is the PicoHarp300 from Picoquant coupled with a

4-channel router (PHR800), which has an electrical time resolution of ~ 12 ps. One thing of which to be careful in TCSPC measurements is to avoid the "pile-up" effect due to the dead time of the electronics by keeping the probability of registering one photon much less than 1, e.g., 0.02.

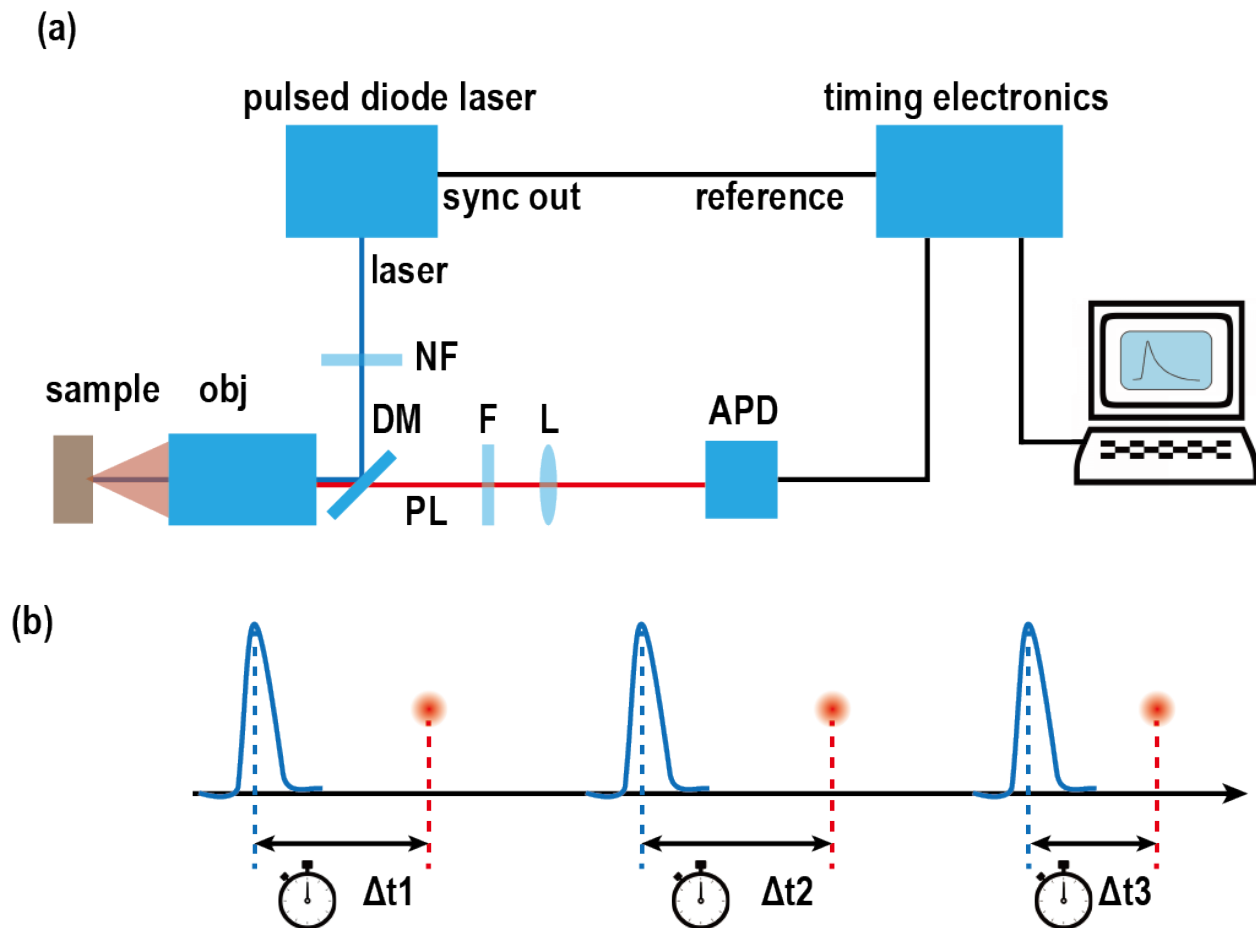


Figure 2.6 **The schematic TCSPC setup and the operating principle.** F, NF, L, and DM represent the filter, neutral density filter, lens, and dichroic mirror. APD represents avalanche photo diode.

2.4 Cryogenics

2.4.1 Continuous flow optical cryostat

The samples are maintained in the optical chamber of a continuous-flow optical cryostat (Advanced Research Systems, LT-3) and placed onto the sample holder, as in Fig. 2.7. The temperature is con-

trolled by adjusting the helium flow rate and heater power, which is controlled by a temperature controller (Lakeshore, Model 325). A microscope objective is placed before the sample chamber for optical excitation and collection. The cryostat is mounted on an XYZ manual stage for positioning the sample. Once thermal equilibrium is achieved, the position of the sample is stable within $2\ \mu\text{m}$. The temperature can be changed from 4.2 K to 500 K.

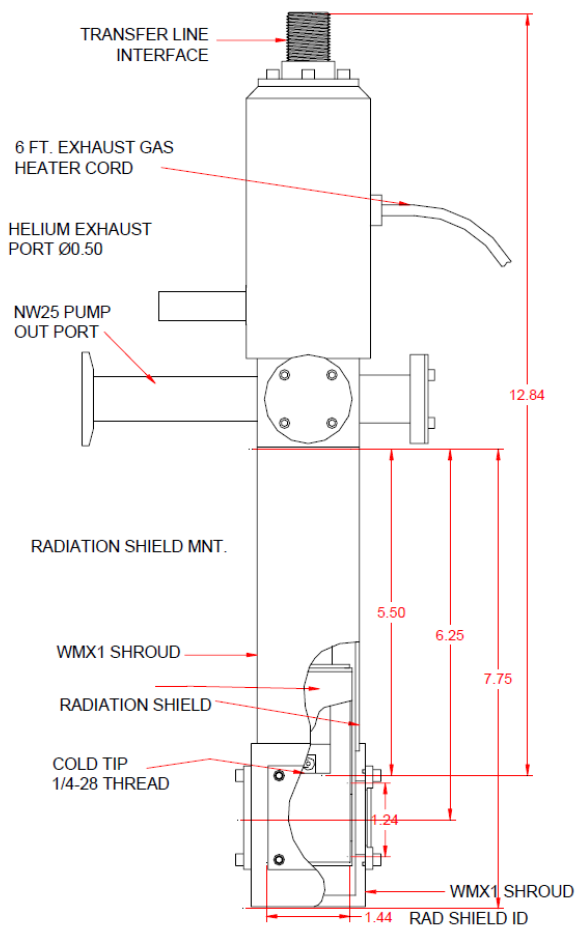


Figure 2.7 Schematic of a continuous-flow optical cryostat (LT-3) from Advanced Research Systems.

2.4.2 Closed-cycle optical cryostat

The samples are mounted on the sample holder in the optical chamber of the closed-cycle optical cryostat (Fig. 2.8). Compared to the continuous-flow cryostat, it is much easier to operate, as it does not require transfer of helium from a dewar and the temperature can be well controlled by

automatically adjusting the helium compression rate and heater power. A microscope objective is placed on the top window, as only the top window allows a short working distance (several mm) for the use of the objective. To position the sample, the cryostat and the objective are mounted on a XY and Z manual stage, respectively. When the helium is compressed in or out of the cryostat, the sample chamber will jitter (tens of μm) in the XY plane due to the instability of the movable stage. Therefore, in our experiments, we need to use several posts to fix the cryostat after we find the sample position. A better solution of sample positioning would be to mount samples on a XYZ piezo stage in the sample chamber, but that is much more expensive. Once thermal equilibrium is achieved, the position of the sample is stable within $3\ \mu\text{m}$. The temperature can be changed from 3 K to 350 K.

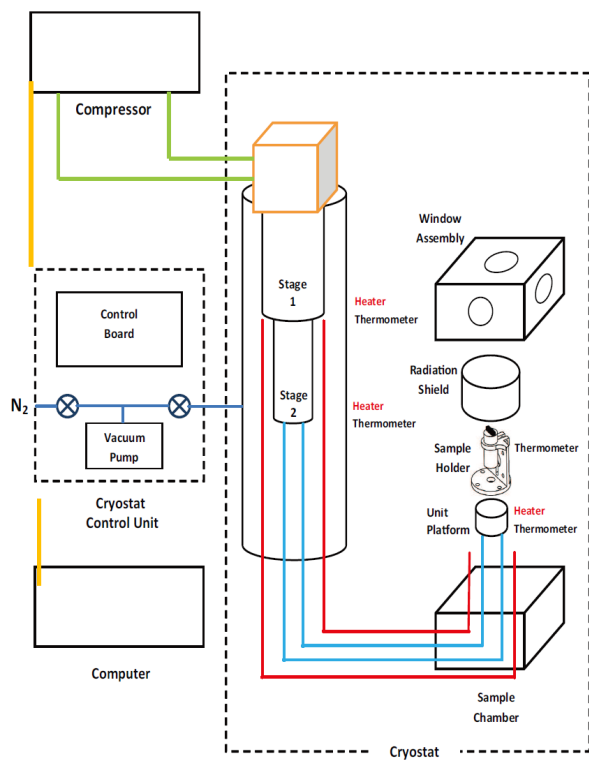


Figure 2.8 **Schematic of the closed-cycle optical cryostat (Montana Instruments, Cryostation).**

CHAPTER 3

EXCITON SPIN DYNAMICS IN GaSe SUB- μm THICK SLABS

3.1 Introduction

Solid-state systems exhibiting high spin polarization and long spin relaxation time are desirable for spintronic applications. Various semiconductors have been studied for creation of long-lived non-equilibrium spin populations and coherences [81, 82, 83, 84, 85, 86]. The most extensively studied system is gallium arsenide (GaAs), partly because of the well developed growth and fabrication techniques, which provides a well-controlled and clean platform to study spin physics. However, owing to the degeneracy of the heavy- and light-hole valence bands and sub-ps hole spin relaxation [87], optically pumped electron spin polarization in bulk GaAs is limited to 1/2, while the maximal degree of circular polarization of photoluminescence is 1/4 [81, 82]. Doping [88] or quantum confinement [89, 90] has been used to quench *electron* spin relaxation. Unity electron spin polarization can be achieved in heterostructures where heavy- and light-hole energy degeneracy is lifted by quantum confinement or strain [91, 92, 93], which will also increase the spin-relaxation time of holes to tens of picoseconds [94, 95].

In analogy to spin polarization, valley polarization has been demonstrated in monolayer transition metal dichalcogenides (TMDs) with potential applications exploiting both spin and the valley degrees of freedom. In monolayer TMDs, inversion symmetry is broken, and a direct gap emerges at the corners (K points) of the Brillouin zone, enabling valley-dependent inter-band transitions under circularly polarized optical excitation [96, 12, 11]. Furthermore, the spin-orbit interaction substantially lifts the spin degeneracy of valence bands at the band edges, leading to that the valley index being totally coupled to the spin (valley-spin locking). Such electronic structure has led to very interesting valley physics, such as reports of a high degree of spin and valley polarization [13, 12, 11], coherence of valley excitons [10, 97], circularly polarized electroluminescence [98], and the valley Hall effect [99]. Although circularly polarized PL with a degree of circular po-

larization from 0.3 to 1.0 was observed in single- and bi-layer TMDs [12, 11, 13, 10, 97] using steady-state near-resonant circularly polarized excitation, which indicates generation and preservation of spin and valley polarization. However, time- and polarization-resolved PL and pump-probe measurements suggest that, at least in MoS₂, circularly polarized PL may result from sub-10-ps recombination lifetimes rather than an intrinsically long-lived valley or hole spin polarization [100, 101]. Additionally, emission at the direct gap becomes dominant only at the monolayer level [102, 103, 104].

In this chapter, we demonstrate GaSe as a material for generating and preserving a high degree of spin polarization under nonresonant optical pumping, owing to the unique bandstructure (Fig. 1.2) of the group-III monochalcogenides, which removes degeneracies between orbital states. In Sec. 3.3, I will discuss the time- and polarization-resolved photoluminescence measurements, which reveal a high initial degree of circular polarization $\rho_0 \cong 0.73 \pm 0.25$ followed by single-exponential spin relaxation (~ 10 ps) at room temperature and $\rho_0 > 0.9$ followed by bi-exponential spin relaxation (~ 30 ps and ≥ 300 ps) at cryogenic temperature. In Sec. 3.4, I will discuss excitation-energy-dependent measurements, which reveal an excitation-energy-insensitive ρ_0 for excitation within 150 meV of the PL peak and $\rho_0 \approx 0.15$ for excitation 1 eV above the PL peak. In Sec. 3.5, I will discuss spin-relaxation mechanisms in GaSe and power-dependent measurements, which show enhanced spin-relaxation rates with increasing excitation intensity and suggest that the Elliott–Yafet (EY) mechanism dominates the spin relaxation of carriers after initial cooling. The results and discussion can also be found in [105, 106].

3.2 Experimental methods

3.2.1 Sample preparation and thickness characterization

Nanometer thick GaSe crystals are mechanically exfoliated from a Bridgman-grown crystal unintentionally *p*-doped at a concentration of $10^{14} - 10^{15} \text{ cm}^{-3}$ [107] and deposited onto a silicon substrate with a 90-nm SiO₂ layer and position markers (Fig. 3.1). To be noted, the method of

exfoliation of thick samples (tens of nm to several μm) is different from that for mono- and few-layer samples (Sec. 5.2.1). Sample thickness is measured by an atomic force microscope in the tapping mode. For AFM tips, one needs to choose higher resonant frequencies when measuring thicker samples ($\sim \mu\text{m}$). Otherwise, the tips cannot respond quickly to a sharp edge and will break the samples. Samples are mounted in vacuum on a copper cold finger attached to an optical liquid-helium flow cryostat for all experiments.

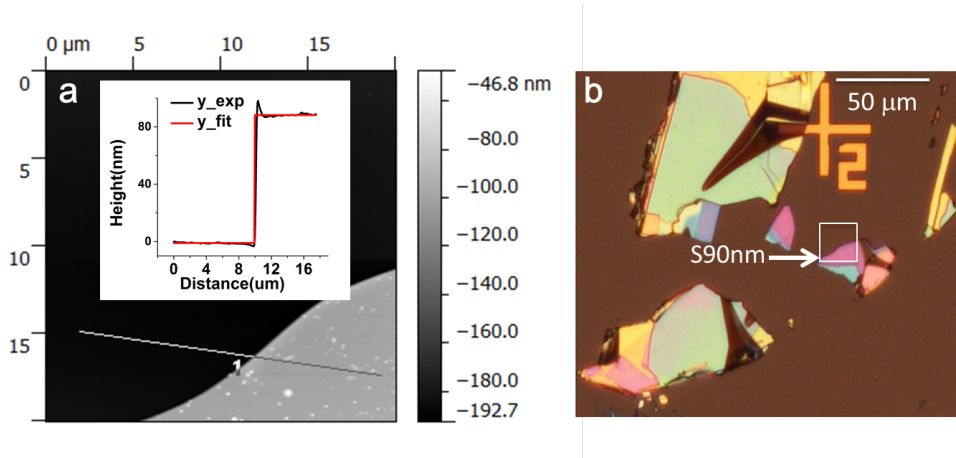


Figure 3.1 **AFM (a) and optical (b) microscope images of a GaSe slab with thickness of 90 nm.** The colors in the optical images are due to thickness-dependent optical interference.

3.2.2 Time- and polarization-resolved photoluminescence

One method of studying spin dynamics is to measure time- and polarization-resolved photoluminescence. The spin-orbit coupling allows the direct coupling of light to the orbital degrees of freedom to produce an initial spin polarization through excitation with circularly polarized light. As the time-reverse process of absorption, the polarization of PL indicates the remaining degree of spin polarization.

3.2.2.1 Setup

A schematic of the setup is shown in Fig. 3.2. GaSe nanoslabs are optically excited by 2-ps laser pulses from a synchronously pumped optical parametric oscillator ($\lambda_p \sim 560\text{--}595\text{ nm}$, $E_p \sim 2.21$

– 2.08 eV, Coherent, Mira-OPO) or by second-harmonic pulses from a Ti:sapphire oscillator ($\lambda_p \sim 410$ nm, $E_p \sim 3.0$ eV, 76 MHz, Coherent, Mira 900-D) powered by a CW pump (Coherent, Verdi V18). The laser output either goes through or bypasses an acousto-optical modulator (Crystal Technology, Model 3000 series), which is used to lower the average excitation intensity without reducing peak intensity. The excitation power is controlled by a liquid-crystal variable retarder (Meadowlark, LRC-200-VIS) between two orthogonally oriented polarizers. The circularly polarized pump is generated by a variable retarder and a Berek polarization compensator (New Focus, Model 5540). The polarization analyzer for the photoluminescence consists of a variable retarder, a polarization rotator, and a wire-grid polarizer (Thorlabs, WP25M-UB). The laser beam is focused through a microscope objective (N.A. = 0.28, Mitutoyo M Plan Apo SL 20x ULWD) to an area of about $80 \mu\text{m}^2$ on the sample. The wave vector of the pump is along the crystal c -axis (the surface normal), i.e., the electric field vector \vec{E} is orthogonal to the c -axis ($\vec{E} \perp c$). The maximum deviation from normal incidence is 8° in air and $\sim 2.5^\circ$ in the crystal for this objective. The photoluminescence is collected by the same objective and focused into a monochromator (f=750 mm, Princeton Instruments, ARC-SP-2758) coupled to a liquid-nitrogen (LN) cooled CCD (Princeton Instruments, Spec-10:400BR/LN) and a streak camera with temporal resolution of 2 ps (Optronis, SC-10) for time-integrated and -resolved studies, respectively. The samples are excited with pump flux P from $0.1 P_0$ to P_0 , where $P_0 = 2.6 \times 10^{14} \text{ cm}^{-2}$ photons per pulse. We estimate the photoexcitation density to be from $\approx 2 \times 10^{16} \text{ cm}^{-3}$ to $3.4 \times 10^{17} \text{ cm}^{-3}$ ($2.7 \times 10^{10} \text{ cm}^{-2}$ per layer) given the absorption coefficient at 2.1 eV ($\approx 10^3 \text{ cm}^{-1}$ for $\vec{E} \perp c$) and loss from reflection. The photoexcited carrier density is below the Mott transition [108] of direct excitons occurring near e-h pair densities of $4 \times 10^{17} \text{ cm}^{-3}$.

3.2.2.2 Pulse train picker based on acousto-optic modulator

To suppress thermal effects without diminishing the peak intensity, a double-pass through an AOM is used to modulate the pulse train [109], as shown in Fig. 3.3. The beam diffraction angle depends on the modulation frequency, which causes problems of alignment and stability of the beam path

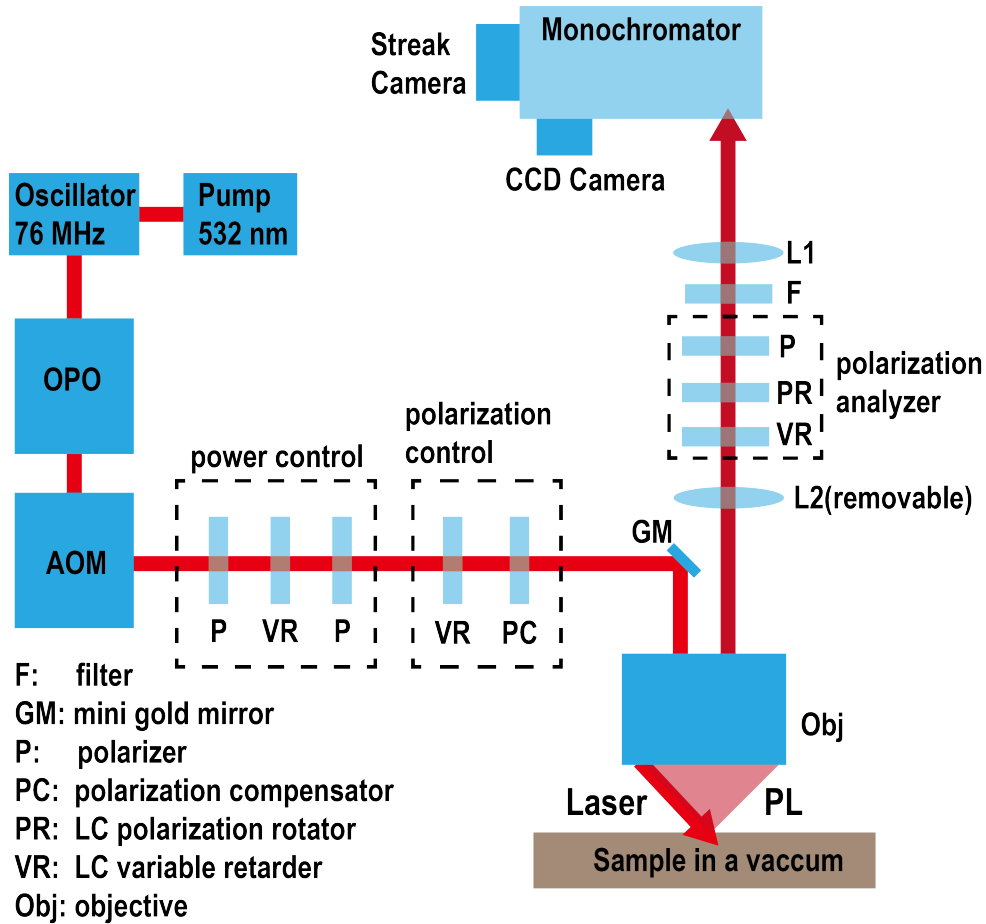


Figure 3.2 **The schematic setup for measurements of time- and polarization-resolved photoluminescence.** The two lenses, L1 and L2, have a focal length $f_1 = f_2 = 100$ mm, and are separated by $f_1 + f_2 = 200$ mm. With L2 out of (in) the optical path, the setup images real (momentum) space.

for a single pass through the AOM. The double-pass configuration makes the angle of the output insensitive to modulation frequency.

3.2.2.3 Power and polarization control based on liquid crystal devices

In the nematic phase, liquid crystal (LC) molecules are oriented in a given direction, creating birefringence, which can be modulated by applying a DC voltage to reorient the molecules (Fig. 3.4). Polarization control based on LC devices allows fast (millisecond switching time) and automatic optical control.

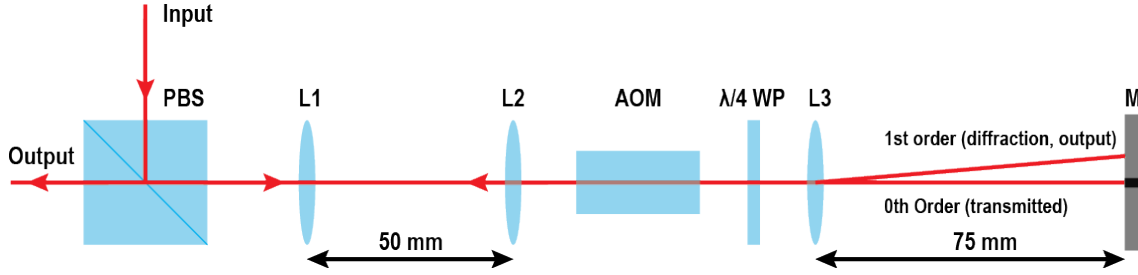


Figure 3.3 **The schematic layout for a pulse-train picker based on an acousto-optic modulator.** PBS represents a polarized beam splitter. $\lambda/4$ WP represents a quarter-wave plate, which rotates the linearly polarized beam by 90° as the beam passes twice. The focal lengths of lenses L1, L2 and L3 are 100, -50, and 75 mm, respectively. L1 and L2 work as a telescope to reduce the beam size to fit the aperture of the AOM. The 0^{th} order beam is blocked, and the 1^{st} order diffracted beam is retroreflected by a silver mirror.

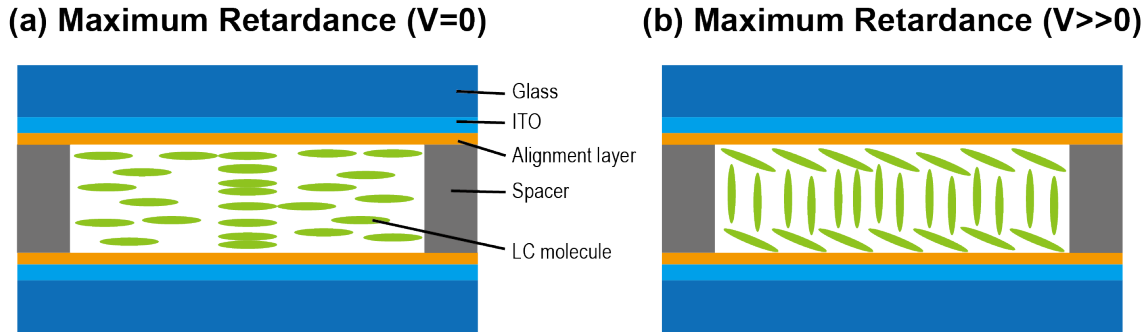


Figure 3.4 **The principle of a liquid-crystal variable retarder, showing molecule orientation with (a) and without (b) an applied DC voltage.**

In Fig. 3.5, we show the orientation of all LC-based modules. For frequencies in visible range, the excitation power can be modulated over three orders of magnitude; the degree of circular polarization of the excitation can be as high as 0.99 and the polarization error can be as small as $\pm 1\%$ in visible region.

3.2.3 Polarization analysis

Linearly polarized light with horizontal (vertical) polarization is labeled as σ^X (σ^Y). Circularly polarized pump or luminescence with angular momentum $+\hbar$ ($-\hbar$) along the pump laser wavevector $\hat{k} \parallel \hat{z}$ is labeled as σ^+ (σ^-). The polarization state is characterized by the Stokes vector $\{S_0, S_1, S_2, S_3\}$. S_0 is the flux and is determined as $S_0 = I^X + I^Y$. The Stokes vector can be

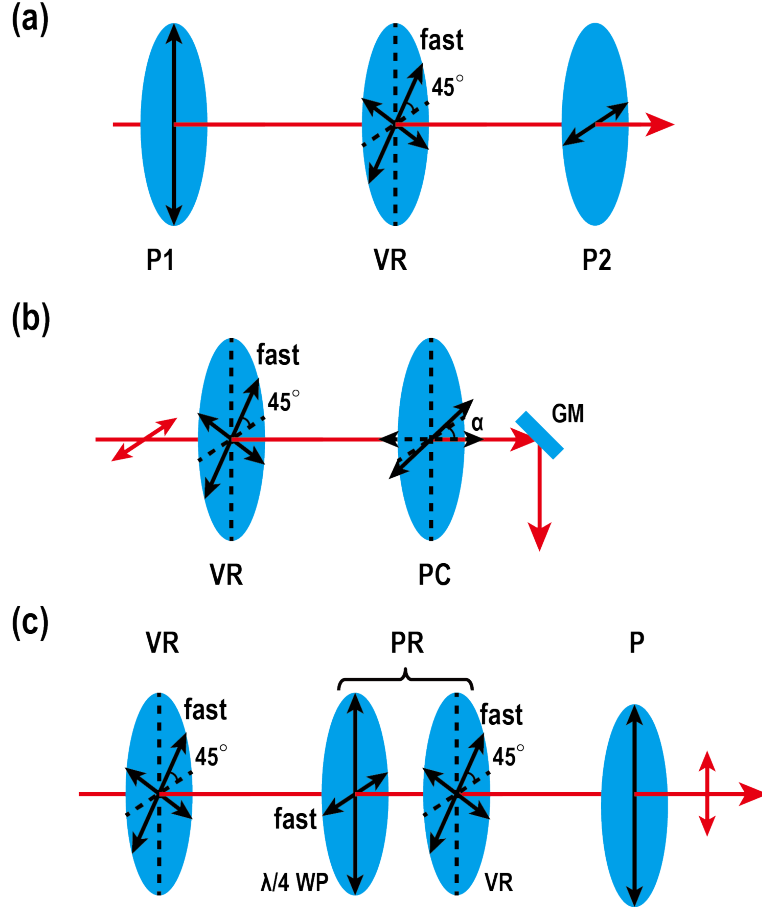


Figure 3.5 The orientation of modules for the power modulation (a), generation of circular polarization (b), and the polarization detection of the full Stokes parameters (c).

normalized by its flux S_0 to yield the Stokes three-vector $s = \{s_1, s_2, s_3\}$, where $s_1 = (I^X - I^Y)/S_0$, $s_2 = (I^{45^\circ} - I^{135^\circ})/S_0$, and $s_3 = (I^+ - I^-)/S_0$. I^+ , I^- , I^X , I^Y , I^{45° , and I^{135° are the measured intensities of circularly or linearly polarized components of the electric field. The degree of circular polarization $DoCP$ is represented by s_3 . The degree of linear polarization is represented by $DoLP \equiv \sqrt{s_1^2 + s_2^2}$, and the polarization orientation angle is determined by $\tan^{-1}(s_2/s_1)$.

3.3 Near-unity generation of optical spin polarization in GaSe

Time- and polarization-resolved PL measurements allow us to separately determine the initial spin orientation, the spin relaxation time, and the recombination time. Due to limited choices of filters,

polarized PL measurements are performed under excitation with energy of about 0.1 to 0.2 eV above the exciton emission peak, instead of resonant excitation. The band-edge exciton emission at room temperature is near 620 nm (2.0 eV), independent of thickness. The exciton peak (not shown) gradually red shifts from 590 nm (2.1 eV) to 620 nm (2.0 eV) in bulk (> 1000 nm) to 90-nm nanoslabs at T = 10 K. This shift is attributed to increasing contribution to PL from localized excitons, like trapped by defects, which is beyond the scope of this thesis. Meanwhile, we observe that the quantum yield of luminescence is greatly suppressed in sub-50-nm thick samples (Fig. 3.6), which makes PL measurements impractical in thin samples. Thus, we will only focus on GaSe nanoslabs ranging from about 90 to 2000 nm thick for spin-dynamics studies.

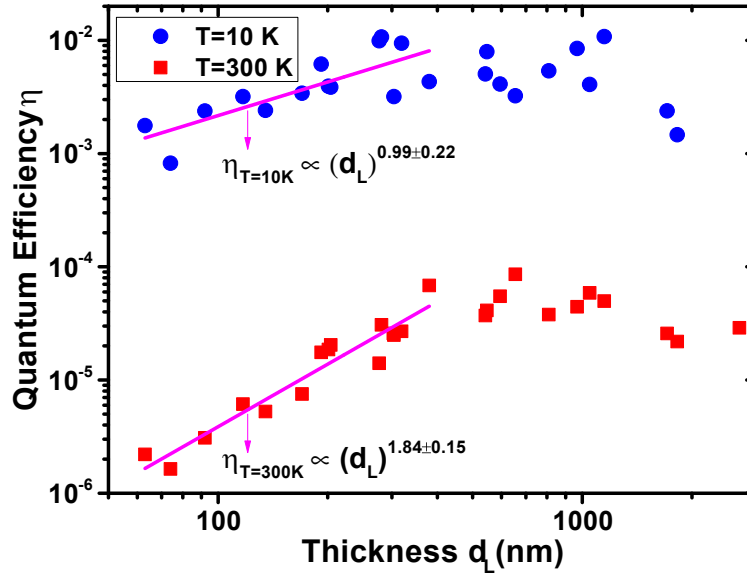


Figure 3.6 **PL quantum efficiency.** Quantum efficiency of luminescence as a function of thickness of GaSe nanoslabs at T = 300 and 10 K. Here, quantum efficiency is defined as the ratio between the luminescence emission flux and optical absorption flux per layer. Optical absorption flux is determined using the experimentally measured reflectance for each sample and reported absorption coefficient $\alpha = 1.1 \times 10^3 \text{ cm}^{-1}$ [110, 111, 112, 113]. Optical collection and detection efficiencies are measured by passing a 633-nm laser beam of known power through the optical setup and spectrometer. The emission flux is then calculated by including the reflection loss at the surface assuming angularly isotropic emission.

3.3.1 Polarization-resolved photoluminescence at room temperature

Upon absorption of circularly polarized light above the band-gap, the stationary (time-averaged) degree of circular polarization ($\bar{\rho}_c$) of luminescence represents photoexcited carrier spin memory. In Fig. 3.7, we show time-integrated PL spectra $[I(E)]$ under co- and cross-circularly polarized excitation and detection for 90 nm- and 650 nm-thick samples at room temperature, respectively labeled as S90nm and S650nm. The PL of S90nm is peaked at about 1.98 eV with $\bar{\rho}_c \approx 0.3$. The PL peak of S650nm is slightly red-shifted to 1.97 eV but with a much smaller $\bar{\rho}_c \approx 0.05$. Across a range of sample thicknesses (d_L), time-integrated PL shows a pronounced increase of $\bar{\rho}_c$ from ~ 0.03 in bulk to 0.3 in sub-100-nm nanoslabs. In the following, I will show that such thickness-dependent $\bar{\rho}_c$ is merely the result of reduced population lifetime in thinner samples.

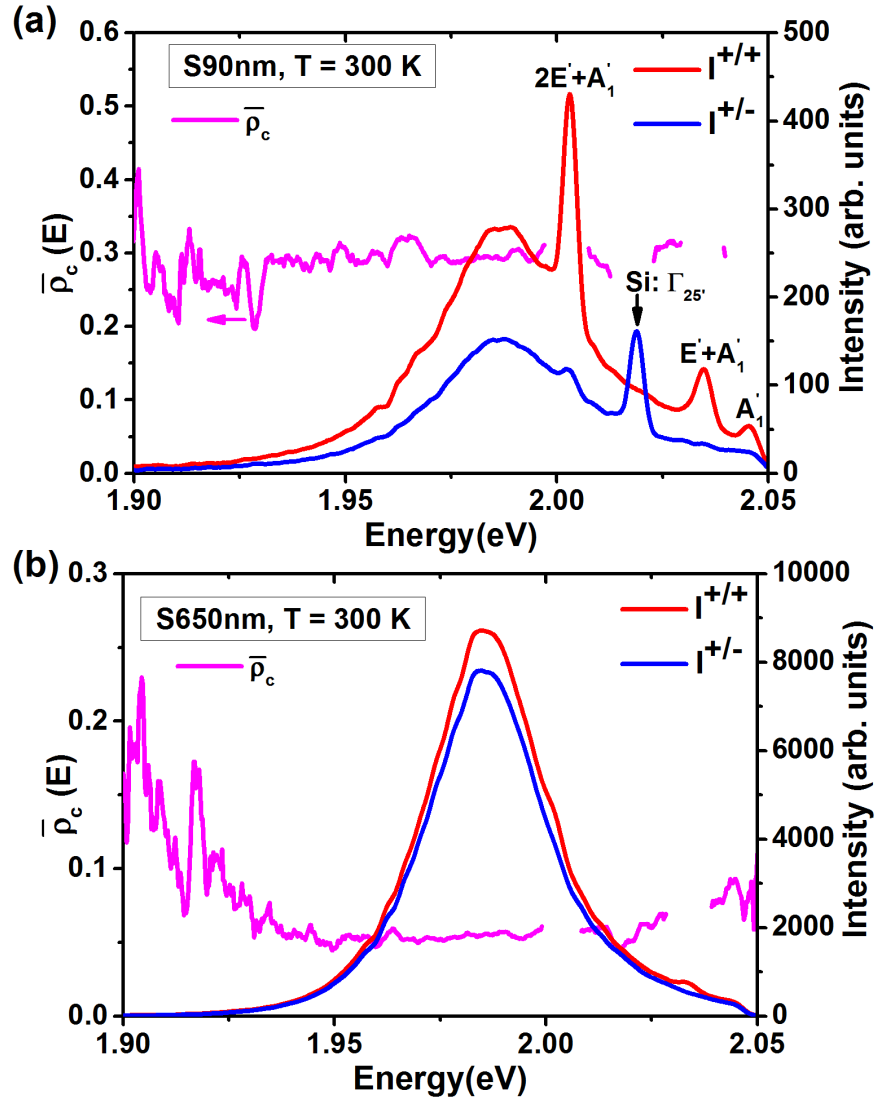


Figure 3.7 **Polarized time-integrated PL spectra at room temperature.** Time-integrated PL spectra [$I^{+/+}(E)$ (co-circular excitation and detection, red) and $I^{+/-}(E)$ (cross-circular excitation and detection, blue)] and degree of circular polarization $\bar{\rho}_c(E) = \frac{I^{+/+}(E) - I^{+/-}(E)}{I^{+/+}(E) + I^{+/-}(E)}$ (magenta) of 90-nm-(S90nm, a) and 650-nm-thick (S650nm, b) samples under σ^+ excitation with 594-nm (2.087 eV) excitation and pump flux $P = 0.5 P_0$ at T = 300 K. Spectra under σ^- excitation have opposite circular polarization with respect to those under σ^+ excitation (not shown). The labeled spectral peaks are assigned to the one-phonon Raman mode A'_1 (310 cm^{-1}) and multi-phonon Raman modes $E'(LO) + A'_1$ [$255 + 136 \text{ cm}^{-1}$] and $2E'(LO) + A'_1$ [$510 + 136 \text{ cm}^{-1}$] in GaSe by energy matching. The multi-phonon Raman modes measured at ~ 394 and 648 cm^{-1} become dominant in sub-100-nm thick GaSe and have not been reported in bulk GaSe. Raman shifts are calibrated against the 520-cm^{-1} Raman line (Γ_{25}' phonon mode) of the silicon substrate.

In Fig. 3.8(a,b), we show time- and polarization-resolved PL measurements with spectral integration for S90nm and S650nm (the Raman signal is only obvious for S90nm at the moment of excitation). Both samples have similar spin relaxation dynamics with a sub-10-ps time constant that is independent of the slab thickness and photoexcited carrier density [106]. That the initial degree of circular polarization ρ_0 of S90nm is smaller than that of S650nm is mostly probably because the Raman signal dominates the initial emission and it exhibits a lower degree of circular polarization (Fig. 3.7). But S90nm experiences much faster population decay than S650nm as revealed by unpolarized PL $I^{X/Y}(t)$. Fig. 3.8(c) shows the time constant τ_0 of single-exponential PL decay as function of thickness. τ_0 increases linearly with thickness from about 20 ps to 250 ps for $90 \text{ nm} \lesssim d_L \lesssim 700 \text{ nm}$ and increases more slowly above 700 nm. Combining the spin and population dynamics, we can understand that the preservation of a high spin polarization during the brief absorption-cooling-emission cycle [114] in sub-100-nm GaSe nanoslabs is because the fast PL rise and decay time constants are comparable to the ~ 10 -ps spin relaxation time. In Fig. 3.8(d), we plot $\bar{\rho}_c$ as a function of PL decay time τ_0 for all samples studied. The stationary $\bar{\rho}_c$ is well described by a simple model: $\bar{\rho}_c = \rho_0 / (1 + \tau_0 / \tau_s)$, where τ_0 is the lifetime of photoexcited carriers, and τ_s is the spin relaxation time. Fitting yields $\rho_0 = 0.73 \pm 0.25$ and $\tau_s = 13 \pm 7$ ps, consistent with the time-resolved measurements. Therefore, the apparent enhancement of “spin memory” revealed in time-integrated PL is largely due to the linear decrease of the PL decay time (τ_0) with thickness, rather than a long spin relaxation time. The decrease of τ_0 is unlikely due to an enhancement of radiative recombination rates with dimensionality and confinement [115] given that the bulk Bohr exciton radius of GaSe is only ~ 5 nm, as also suggested by the reduced quantum yield in thinner samples (Fig. 3.6). The linear dependence of $\tau_0 \propto d_L$ can result from non-radiative surface recombination [116].

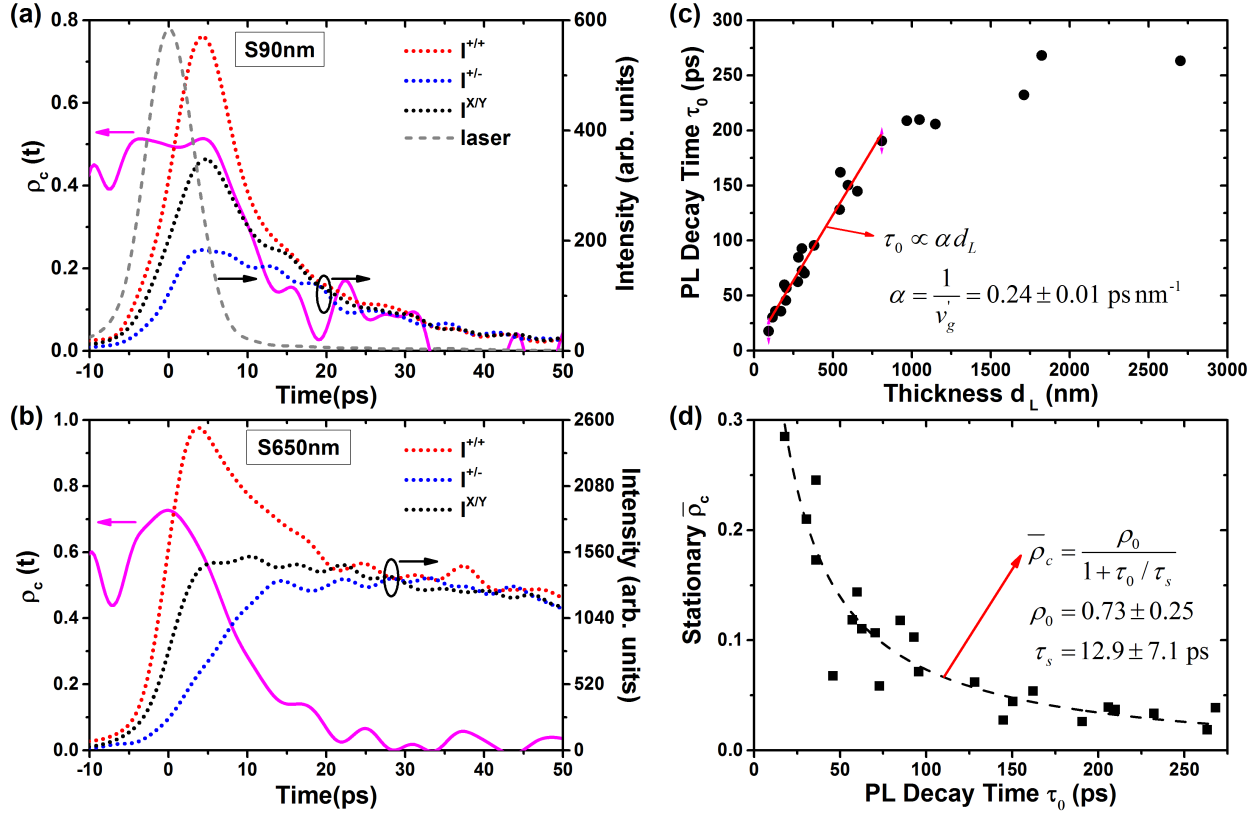


Figure 3.8 **PL dynamics and polarization properties versus sample thickness at room temperature.** Time-resolved PL of S90nm (a) and S650nm (b) with different polarization combinations for excitation and detection: σ^+/σ^+ (red dotted), σ^+/σ^- (blue dotted) and σ^X/σ^Y (black dotted). The laser response (gray dashed curve) represents the instrumental temporal resolution. The solid magenta curves represent the time-resolved degree of circular polarization $\rho_c(t)$. (c) PL decay time constant (τ_0) as a function of thickness (d_L) of the samples (black circles). τ_0 decreases linearly with thickness for $d_L \lesssim 700$ nm yielding a slope or an effective group velocity of 0.24 ps/nm. (d) This results in an increasing stationary circular polarization (black squares) near the exciton PL peak [$\bar{\rho}_c(E \approx 1.98$ eV)] with decreasing τ_0 (thickness), described by the formula inserted in (d), which reveals an initial spin polarization $\rho_0 = 0.73$ and spin lifetime $\tau_s = 12.9$ ps.

3.3.2 Polarization-resolved photoluminescence at cryogenic temperature

At cryogenic temperature ($T = 10$ K), the spin and PL decay dynamics slow markedly for excitation at 560 nm (2.214 eV) to 575 nm (2.156 eV). Similar $\bar{\rho}_c(E)$ and PL dynamics are observed for all studied samples with $d_L > 90$ nm at $T = 10$ K. We thus describe only the results from S90nm. At a pump fluence of $0.1 P_0$, the stationary $\bar{\rho}_c(E)$ reaches 0.8 at the high-energy range of the exciton emission spectrum and decreases gradually to about 0.2 at low emission energies (Fig. 3.9).

Meanwhile, time-dependent PL decay becomes bi-exponential with time constants $\tau'_0 \approx 20\text{-}50$ ps and $\tau''_0 \approx 150\text{-}200$ ps (Fig. 3.10[a]). In contrast, the PL rise time remains about 10 ps (limited by instrument temporal resolution), suggesting sub-10-ps cooling and momentum relaxation of radiative photoexcited carriers independent of temperature. Time-dependent circular polarization $\rho_c(t)$ is also found to be bi-exponential, with decay time constants $\tau'_s \approx 30\text{-}40$ ps and $\tau''_s \gtrsim 500$ ps (Fig. 3.10[b]). As shown below (Fig. 3.15), the shorter time constant τ'_s shows a weak power-law dependence on the photoexcited density (n_X) with $\tau'_s \propto n_X^{(-0.23 \pm 0.06)}$, while there is no identifiable dependence on thickness for either population decay or spin relaxation. That τ'_0 is close to τ'_s is not a coincidence. We will demonstrate in Chap. 4 that both τ'_0 and τ'_s are caused by transitions from triplet to singlet excitons.

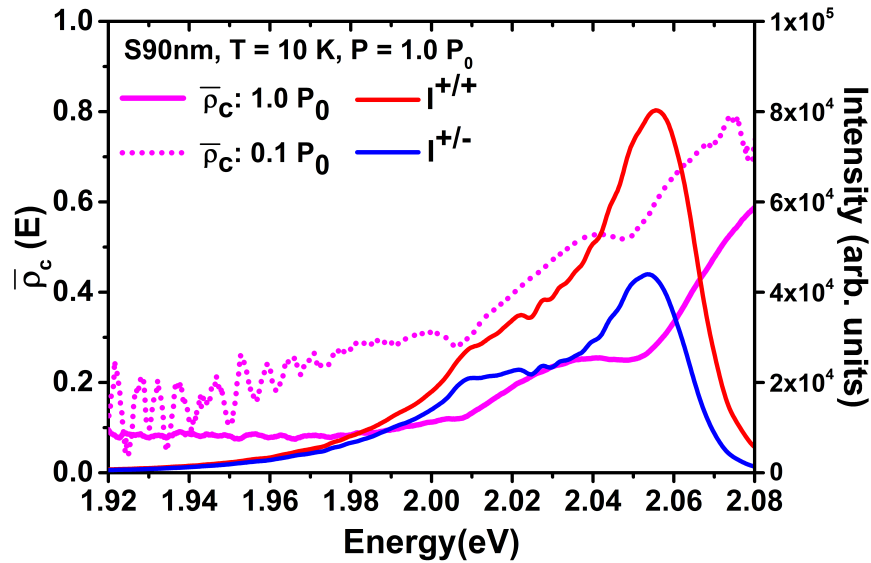


Figure 3.9 **Time-integrated and polarization-resolved PL spectra.** Time-integrated PL spectra [$I^{+/+}(E)$ (co-circular, red) and $I^{+/-}(E)$ (cross-circular, blue)] and degree of circular polarization $\bar{\rho}_c(E)$ of S90nm under σ^+ excitation at pump flux $P = 1.0 P_0$. $\bar{\rho}_c(E)$ at $P = 0.1 P_0$ for S90nm is shown as a magenta dotted curve for comparison.

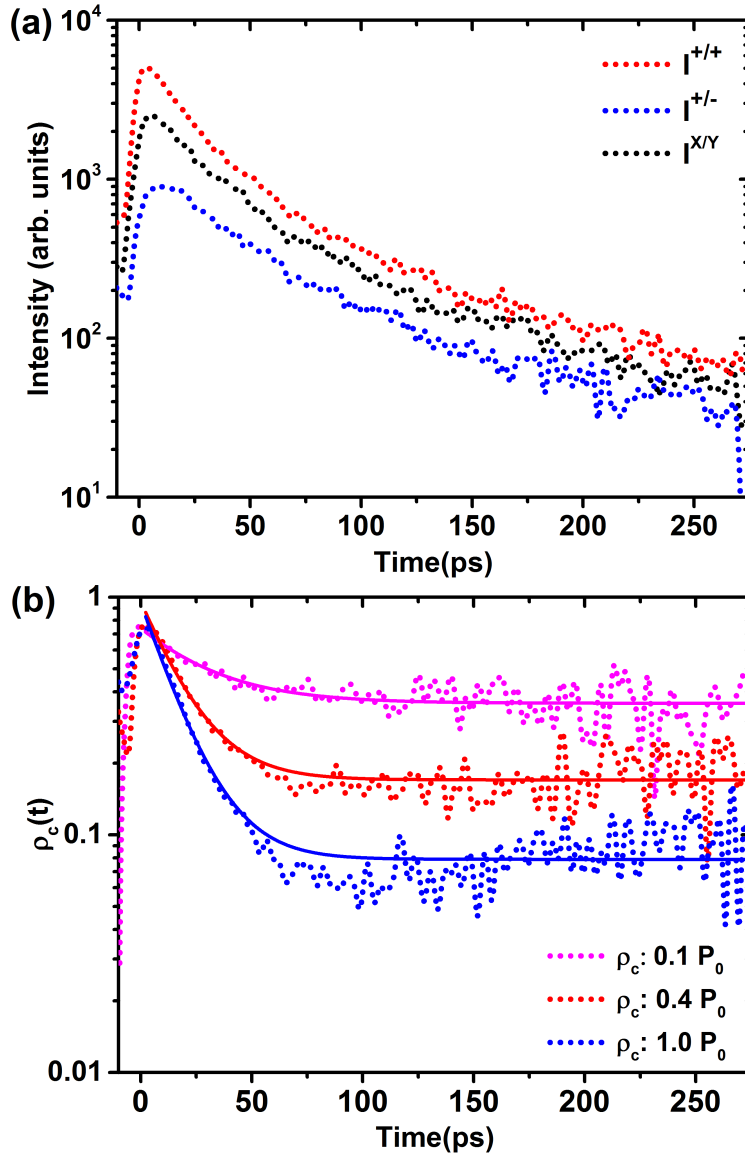


Figure 3.10 **Polarized PL dynamics.** (a) Polarized time-dependent PL of S90nm for $I^{+/+}(t)$, $I^{+/-}(t)$, and $I^{X/Y}(t)$ (dashed red, blue, and black, respectively) at $P = 0.1 P_0$. (b) $\rho_c(t)$ of PL from S90nm under σ^+ excitation at a pump flux of $P = 0.1, 0.4,$ and $1.0 P_0$ (magenta, red, and blue, respectively). Solid lines are bi-exponential fittings.

3.4 Spin dynamics at different excitation energies

To understand the spin dynamics, we consider the model of the exciton spin dynamics in Fig. 3.11. In our measurements, hot carriers with excess energy and a given spin are initially generated and then quickly cool (W_k) to the band edge (see Fig. 1.2 for optical selection rules). There are two possible spin-relaxation channels: Individual spin-flip of electrons or holes (W_s) and exciton spin-flip (W_X), i.e., simultaneous spin flip of electrons and holes. These are accompanied by population decay (for simplicity, we only attribute population decay of the band-edge excitons to radiative recombination from the $|0,0\rangle$ and $|1,\pm 1\rangle$ excitons with rates W_R^0 and W_R , respectively). There are several questions we would like to answer. Which spin-relaxation channel dominates, W_s or W_X ? How much initial spin polarization can be generated with high-energy excitation, and how much remains after hundreds of meV cooling?

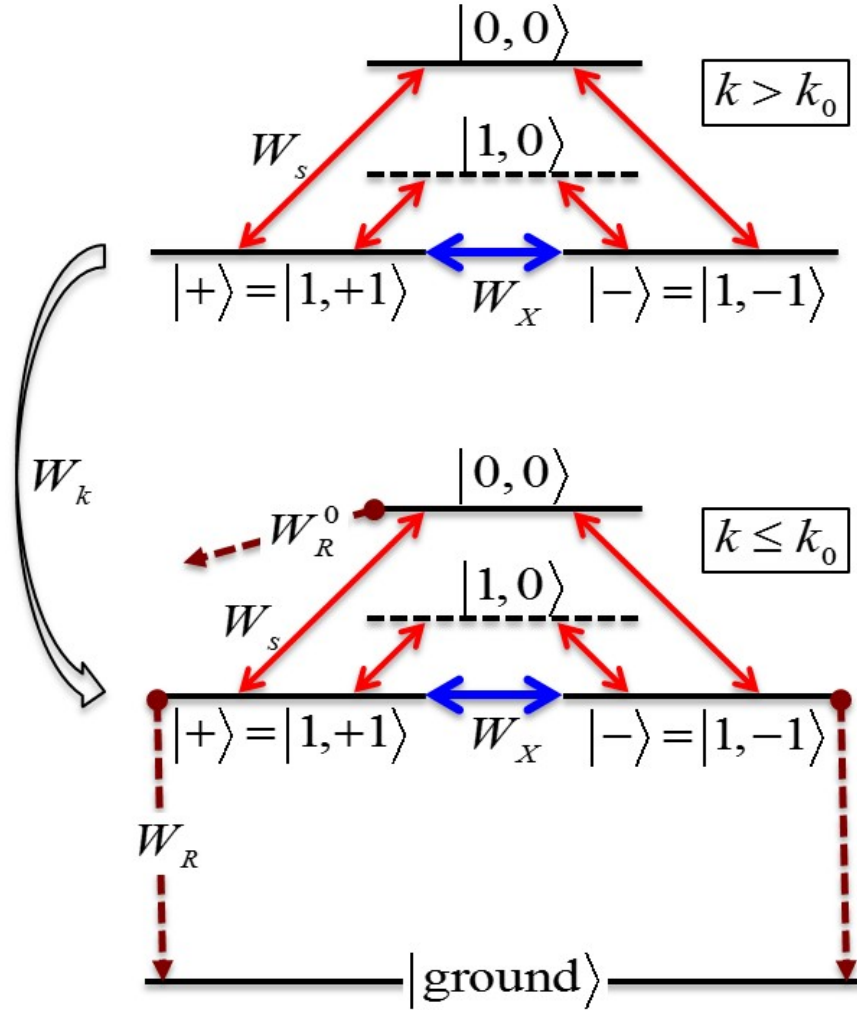


Figure 3.11 **Schematic of the model for exciton spin dynamics.** W_R^0 and W_R represent radiative decay rates of $|0,0\rangle$ and $|1,\pm 1\rangle$ excitons, respectively. W_x and W_s represent the spin-flip rates of excitons and individual electrons/holes, respectively. W_k represents the initial cooling rate.

Fig. 3.12 shows time-integrated PL spectra under co- and cross-circularly polarized excitation and detection at $T = 10$ K with excitation energies of 2.156 eV and 2.214 eV. The PL is peaked at about 2.07 eV with a low-energy tail that is attributed to localized excitons. As in samples described previously, the degree of steady-state spin polarization ($\bar{\rho}_c$) is highest at high energies, as expected given the reduced time spent at such energies and that carriers have undergone less relaxation than fully relaxed band-edge carriers. There is also a pronounced increase in $\bar{\rho}_c$ as the excitation-photon energy decreases towards the band gap. This is as expected from the greater

E (eV)	A_1	τ_s' (ps)	A_2	τ_s'' (ps)
2.156	0.534	36.8	0.356	265
2.214	0.672	31.2	0.199	278

Table 3.1 Fitting parameters of a bi-exponential decay function, $\rho_c(t) = A_1 \exp(-t/\tau_s') + A_2 \exp(-t/\tau_s'')$.

spin-orbit field at larger k in the D'yakonov-Perel' (DP) mechanism of spin relaxation and the increased rate of scattering at larger k in the EY mechanism, which will be discussed more in Sec. 3.5.

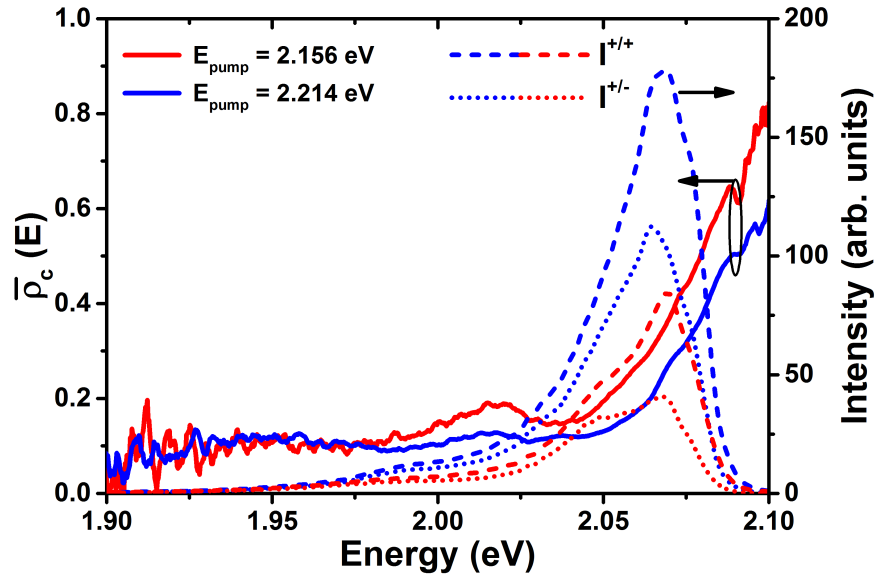


Figure 3.12 **Polarized PL spectra of S540nm under optical excitation at 2.156 eV and 2.214 eV.** Time-integrated PL spectra [$I^{+/+}(E)$ (co-circular, dashed lines) and $I^{+/-}(E)$ (cross-circular, dotted lines)] and degree of circular polarization $\bar{\rho}_c(E)$ (solid lines) of S540nm GaSe samples under σ^+ excitation at pump flux $P = 0.5 P_0$, where $P_0 = 2.6 \times 10^{14} \text{ cm}^{-2}$ per pulse. Blue (red) lines are for $E_{pump} = 2.214 \text{ eV}$ (2.156 eV).

For more direct insights into the nature of the spin relaxation, we performed time-resolved measurements of the spectrally integrated PL at cryogenic temperatures (10 K) in Fig. 3.13. The PL at cryogenic temperatures (10 K) reveals a fast ($< 10 \text{ ps}$) rise time followed by a biexponential decay for spin-relaxation and population dynamics. Bi-exponential fitting parameters at both excitation energies are given in Table 3.1. The fast spin-relaxation component τ_s' decreases from 37 ps to 31 ps, which is consistent with the expectation that greater spin-orbit field and faster momentum scat-

tering at higher energies should result in faster spin relaxation. The ratio of the fast amplitude to the slow amplitude increases from 1.5 to 3.4 as the excitation energy increases from 2.156 eV to 2.214 eV. The initial $\rho_0 \cong 0.9$ is almost unchanged, which suggests the optical selection rules (Fig. 1.2) still hold without involving other transitions at such excitation energies. Next we consider the difference between the time-dependent PL intensity under linearly and circularly polarized excitation conditions, revealed by $R(t) \equiv I^+(t)/I^X(t) = [I^{+/+}(t) + I^{+/-}(t)] / [I^{X/X}(t) + I^{X/Y}(t)]$, where $I^+(t)$ and $I^X(t)$ respectively represent the total photoluminescence intensity created by circularly and linearly polarized light. Under linearly polarized excitation, the photoexcited electrons and holes are assumed to be equally distributed over their respective spin states, i.e. $|\pm 1/2\rangle$, during the initial 2-ps laser excitation. The nongeminate (bimolecular) formation of excitons then produces an initial exciton population distributed equally over the three triplet exciton states $|1, \pm 1\rangle$ and $|1, 0\rangle$. We contrast this to the case of circularly polarized excitation (σ^+), under which only the bright exciton state $|1, +1\rangle$ is initially formed. Under σ^+ excitation, the ratio $R(t)$ will decrease from approximately 1.5 to 1 as the populations in the three triplet states eventually become nearly equal through spin relaxation under σ^+ excitation. The peak magnitude and single-exponential time constant (~ 10 ps) of $R(t)-1$ in Fig. 3.13 are qualitatively consistent with this expectation, which suggests that W_S is the dominant process in spin relaxation, which will be further demonstrated in Chap. 4.

The bi-exponential nature of $\rho_c(t)$ has not been determined, but there are two possible explanations. One is that the bi-exponential decay of $\rho_c(t)$ can be understood as a consequence of fast spin relaxation during thermalization to the band edge followed by slower spin relaxation once the carriers are at the band edge. The other is that the fast component is from free carriers and the slower component is from localized (e.g., trapped) carriers.

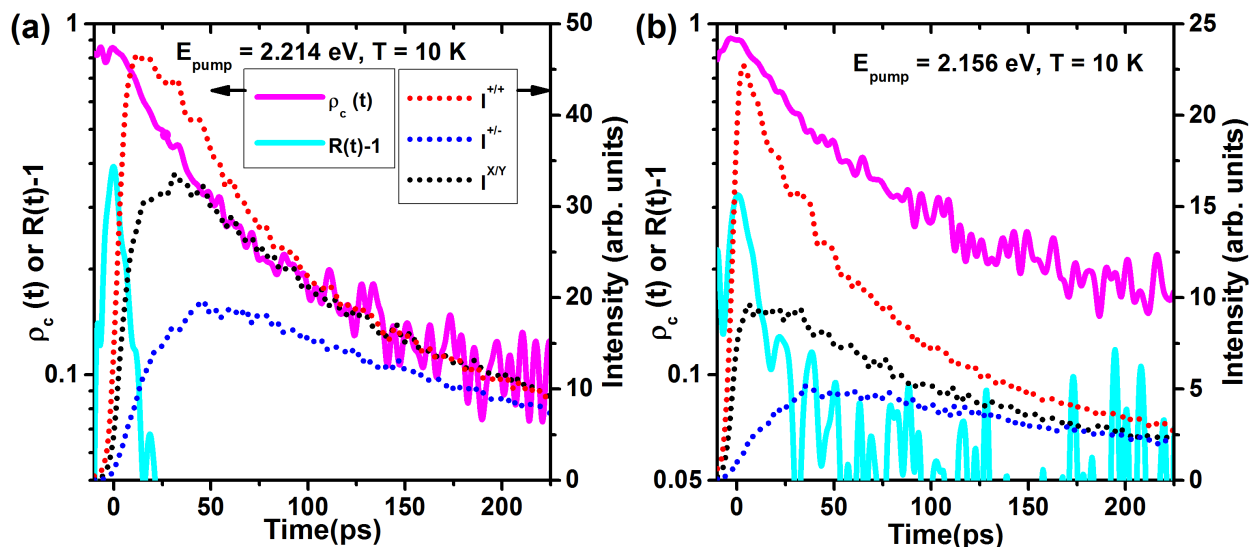


Figure 3.13 **Polarized PL dynamics of S540nm under optical excitation at 2.156 eV and 2.214 eV.** Time-dependent PL intensity [$I^{+/+}(t)$, $I^{+/-}(t)$, and $I^{X/Y}(t)$ (dotted red, blue, and black, respectively)], degree of circular polarization $\rho_c(t) = \frac{I^{+/+}(t) - I^{+/-}(t)}{I^{+/+}(t) + I^{+/-}(t)}$ (solid magenta), and $R(t) - 1 = \frac{I^{+/+}(t) + I^{+/-}(t)}{I^{X/X}(t) + I^{X/Y}(t)} - 1$ (solid cyan) under excitation $E_{pump} = 2.214$ eV (a) and $E_{pump} = 2.156$ eV (b) at $P = 0.5 P_0$. The \pm/\pm (X/Y) labels represent the helicity (polarization) of the pump laser and luminescence, respectively.

To explore the limits of spin memory, we also performed experiments on a 650 nm-thick sample (S650nm) under 3.0 eV excitation (Fig. 3.14). We find that the initial ρ_0 at the band edge is 0.15, irrespective of temperature, followed by a single-exponential decay with a time constant of 10 ps. By contrast, an ultrafast electron spin-relaxation time of 200 fs has been observed in bulk GaAs under a 3.00 ± 0.05 eV excitation (i.e., excess energy ≈ 1.5 eV above the GaAs band gap) when the L -valley transitions are involved [117]. The generation of a substantial degree of spin polarization at the band edge after highly nonresonant excitation and relatively much longer spin-relaxation time compared to the case of bulk GaAs is a consequence of the highly orbitally nondegenerate bands involved in optical excitation and emission in GaSe. The PL measurements presented here only probe excitons and carriers near the band edge (the Γ point). At 3.0 eV excitation, carriers must dissipate 1 eV excess energy. This takes markedly larger than dissipation

0.1-0.2 eV, especially at $T = 10$ K, leading to little remaining spin polarization when most carriers have cooled to the Γ point. Thus the reduced initial degree of spin polarization observed at the band edge might be due to reduced polarization generated by 3.0 eV transitions, which occur at other points of the Brillouin zone and loss of spin memory during momentum scattering back to the Γ point.

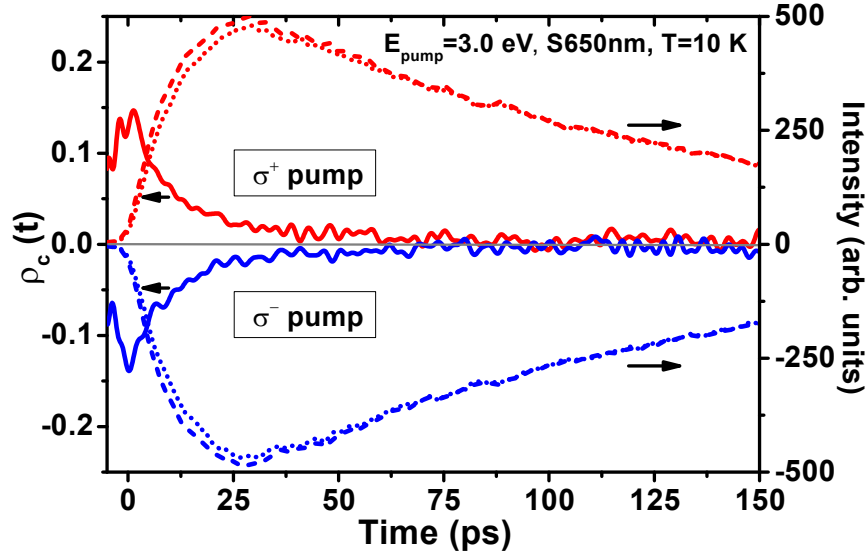


Figure 3.14 **Polarized time-dependent PL under optical excitation at 3 eV.** Time-dependent PL intensities $I^{\pm/\pm}(t)$ (co-circular, dashed curves) and $I^{\pm/\mp}(t)$ (cross-circular, dotted curves), degree of circular polarization $\rho_c(t)$ (solid curves) under excitation at $E_{pump} = 3$ eV and $T = 10$ K. Red and blue curves are for σ^+ and σ^- excitation, respectively. The decay of $\rho_c(t)$ is slower at $T = 10$ K than that at $T = 300$ K (not shown) (≈ 7 ps vs. 3 ps) as is the PL rise time (≈ 18 ps vs. 5 ps).

3.5 Mechanism of spin relaxation in GaSe

Spin-relaxation mechanisms in semiconductors depend on details of the energy-versus-momentum dispersion and spin-splitting because of spin-orbit interaction [118, 119]. In III-V semiconductors such as GaAs, the group-V p_x , p_y , and p_z -derived valence bands are closely spaced because of the small crystal field. Consequently, the angular momentum and quasimomentum of holes are strongly coupled, and the spin orientation of holes is lost in a period comparable to the momentum relaxation time (τ_p) [120, 121, 87, 122, 123, 82, 124, 84]. The slower relaxation of *electron* spin

in such semiconductors is a result of the reduced spin–orbit mixing of the group-III s -orbital-derived conduction band with distant bands. Electron-spin relaxation is usually analyzed in terms of three mechanisms [81, 83, 84, 125]: the D’yakonov–Perel’ (DP) [126, 127, 81], Elliot-Yafet (EY) [128, 129], and Bir-Aronov-Pikus mechanism [130, 131, 132, 133]. The DP mechanism is associated with spin–orbit-induced spin splitting of a band in noncentrosymmetric systems, i.e., the spin splitting works as an effective magnetic field on the spin of carriers, and spin relaxation only occurs between two scattering events; The EY mechanism is associated with the spin–orbit interaction, i.e., an electric field, such as that induced by lattice vibrations or charged impurities, is transformed into an effective magnetic field through spin–orbit interaction, and spin relaxation only occurs during scatterings. The BAP mechanism is associated with electron–hole exchange interactions and may dominate the electron spin relaxation in heavily p -doped semiconductors. For photoexcited carrier densities above 10^{16} cm^{-3} as studied in undoped GaSe here, we neglect spin relaxation due to the BAP mechanism, since only the electron–hole exchange interaction between photoexcited carriers is important, which does not change the total angular momentum.

The EY and DP mechanisms are respectively associated with the spin–orbit interaction (SOI) and the spin–orbit-induced spin splitting, $\Delta_s(\vec{k}) = |E(\vec{k}, \uparrow) - E(\vec{k}, \downarrow)|$ [82, 125]. Using a four-state (two bands with spin) model Hamiltonian in the absence of an external magnetic field, one can express the spin-relaxation rate of electrons (holes) with wave vector \vec{k} away from the conduction (valence) band edge with the following equation [125]:

$$\Gamma_s \sim \frac{|\Delta_s(\vec{k})|^2}{\hbar^2 \Gamma_p} + \frac{\Gamma_p |L(\vec{k})|^2}{\hbar^2 \Gamma_p^2 + \Delta_g^2(\vec{k})}, \quad (3.1)$$

where $\Gamma_p = 1/\tau_p$ is the scattering rate of electron (hole), with τ_p being the corresponding momentum scattering (or correlation) time, $\Delta_s(\vec{k})$ is the spin–orbit-induced spin splitting, and $L(\vec{k})$ is the SOI between adjacent bands with energy separation Δ_g . One or the other of the two terms in Eq. 3.1 can dominate in different regions of momentum space.

In GaSe, the initial carrier cooling to the band edge occurs in the sub-ps to sub-10 ps range (Fig. 3.13) [114]. This fast energy and momentum relaxation ($\tau_p \sim 1 \text{ ps}$) is demonstrated by the sub-10

ps PL rise time that is nearly independent of PL emission energy. During this cooling time, the carrier spin relaxation is dominated by the DP mechanism. This can be seen as follows. Because the p_z -like UVB is well isolated from the LCB and the adjacent $p_{x,y}$ -like valence bands, $\Delta_g \sim 1\text{--}2$ eV, which corresponds to a rate that is much greater than the electron/hole momentum relaxation rate of $\Gamma_p \sim (1\text{ps})^{-1}$. In this case ($\hbar\Gamma_p \ll \Delta_g(\vec{k})$), the hole-spin relaxation caused by the EY mechanism $\Gamma_s^{EY} \approx (\frac{L}{\Delta_g})^2\Gamma_p \ll \Gamma_p$. Meanwhile, in ε -GaSe at large momenta, hole spin splitting $\Delta_s^h(k' = 0.15) \approx 5$ meV [34] and $k' = |\vec{k}|/\overline{\Gamma K}$, where $\overline{\Gamma K}$ is the length from the Γ point to the K point. As a result, for holes with finite momentum k' , $|\Delta_s^h(k')|^2/\hbar\Gamma_p \gg \hbar\Gamma_p|L(k')|^2/\Delta_g^2(k')$, i.e., spin relaxation of *hot* holes in GaSe is dominated by the DP mechanism, in which spin relaxation occurs from the precession of spins in an effective magnetic field associated with $\Delta_s^h(k')$ [81, 82, 125].

After cooling, it is not a priori obvious whether DP or EY should constitute the dominant mechanism for spin relaxation. However, we observe experimentally that the EY mechanism plays a larger role than the DP mechanism in the initial decay of ρ_c after cooling of carriers to the band edge. In general, the momentum scattering time $\tau_p(n)$ is expected to decrease with increasing carrier density n . Therefore, the spin relaxation time, τ_s , should increase with increasing n if spin relaxation is dominated by the DP mechanism and, for $\Delta_g \gg \hbar\Gamma_p$, decrease with increasing n if spin relaxation is dominated by the EY mechanism. As shown in Fig. 3.15, at $T = 10$ K, we found the initial decay of ρ_c is characterized by $\tau_s' \propto n^{-0.23}$. The decreasing spin relaxation time with the increasing density (i.e., decreasing τ_p) suggests that the EY mechanism plays a larger role than the DP mechanism in the spin relaxation of *cold* excitons near the band edge in GaSe at low temperature.

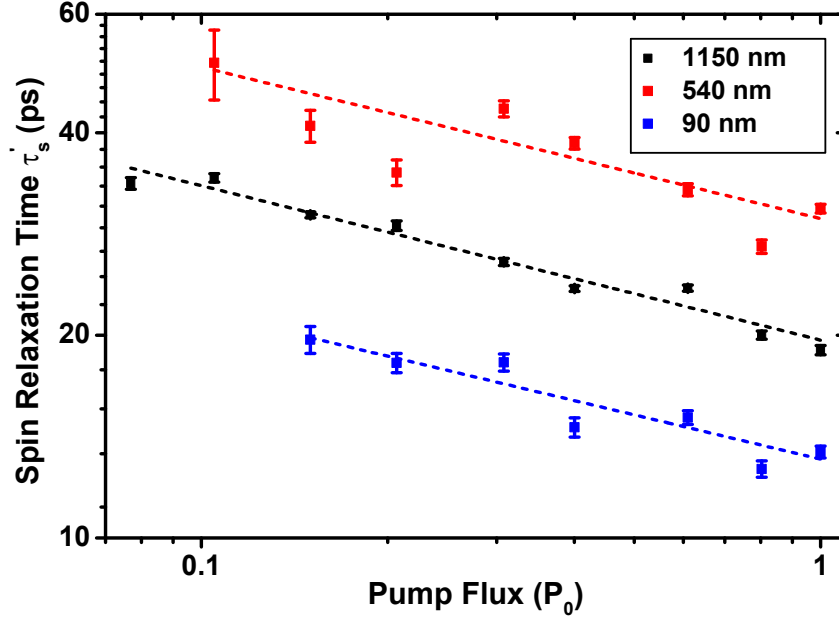


Figure 3.15 The initial spin decay time τ'_s versus the pump flux P (photoexcited density n) for 90 nm, 540 nm, and 1150 nm thick GaSe slabs. The pump flux $P_0 = 2.6 \times 10^{14} \text{ cm}^{-2}$ per pulse. The fitting gives a power law $\tau'_s \propto n^{-0.22 \pm 0.04}$, $n^{-0.23 \pm 0.02}$, and $n^{-0.23 \pm 0.06}$ for 90 nm, 540 nm, and 1150 nm GaSe slabs, respectively.

3.6 Conclusion

We demonstrated generation of a high degree of optical spin polarization ($\rho_0 \approx 0.9$) under non-resonant excitation and a long spin memory ($\tau \geq 500$ ps) in GaSe at cryogenic temperature as revealed by time- and polarization-resolved photoluminescence measurements, which are attributed to orbital non-degeneracy of conduction and valence bands. Even at room temperature, ρ_0 as large as 0.7 is observed and followed by a single-exponential decay with $\tau \leq 10$ ps, while pumping 1 eV above the band edge yields $\rho_0 = 0.15$. For future directions, the mechanism of thickness-dependent population lifetime at room temperature needs to be determined, which should be associated with nonradiative processes. Even though the carrier-density-dependent spin relaxation ($\tau'_s \propto n_X^{-0.23 \pm 0.06}$) at cryogenic temperature suggests the EY mechanism might be dominant, the temperature-dependent spin-relaxation measurements are still needed to clarify the spin mechanism.

CHAPTER 4

DIRECT OBSERVATION OF TRANSITIONS FROM TRIPLET TO SINGLET EXCITONS

4.1 Introduction

In most bulk semiconductors, the optical orientation and alignment of electron-hole ($e-h$) pairs and consequent polarized luminescence are limited [134]. In quasi-2D systems, such as semiconductor quantum wells, whether photoluminescence is typically polarized depends strongly on the photoexcitation energy and polarization as well as the band structure. Highly linearly polarized luminescence or lasing has been observed in quasi-1D colloidal nanowires [135, 136, 137] with strong dielectric confinement, as well as in quasi-0D quantum dots with a sizable anisotropy induced by strain or electron-hole exchange interactions [138, 139, 140, 141]. Recently, in atomically thin transition metal dichalcogenides (TMDs), polarized luminescence has been shown to result from intra- and interlayer excitations [142] or valley coherence [143, 144]. In 2D TMDs, though, the luminescence yield only becomes significant at the monolayer level when a crossover from indirect to direct gap occurs.

In this chapter, we exploit the anisotropic optical properties [145, 146, 147, 110, 112, 111] and unique optical selection rules [29, 30, 105] in layered GaSe. We report highly linearly polarized remote luminescence that emerges at the cleaved edges of sub- μm GaSe slabs tens of micrometers away from the optical excitation spot. The remote-edge luminescence (REL) measured in the reflection geometry has a degree of linear polarization above 0.90, with polarization orientation pointing toward the photoexcitation spot. The REL is dominated by an index-guided optical mode that is linearly polarized along the crystalline c -axis. In Chap. 3, we observed biexponential decays for both spin ($\tau'_s \approx 30\text{--}40$ ps and $\tau''_s \gtrsim 500$ ps) and population ($\tau'_0 \approx 20\text{--}50$ ps and $\tau''_0 \approx 150\text{--}200$ ps). With the linearly polarized REL, we demonstrate that the initial decays of spin and population are due to the same process, one in which out-of-plane dipoles are converted from in-plane dipoles

through a spin-flip process at the excitation spot. The results and discussion can also be found in Ref. [148].

4.2 Luminescence emerging on the edge

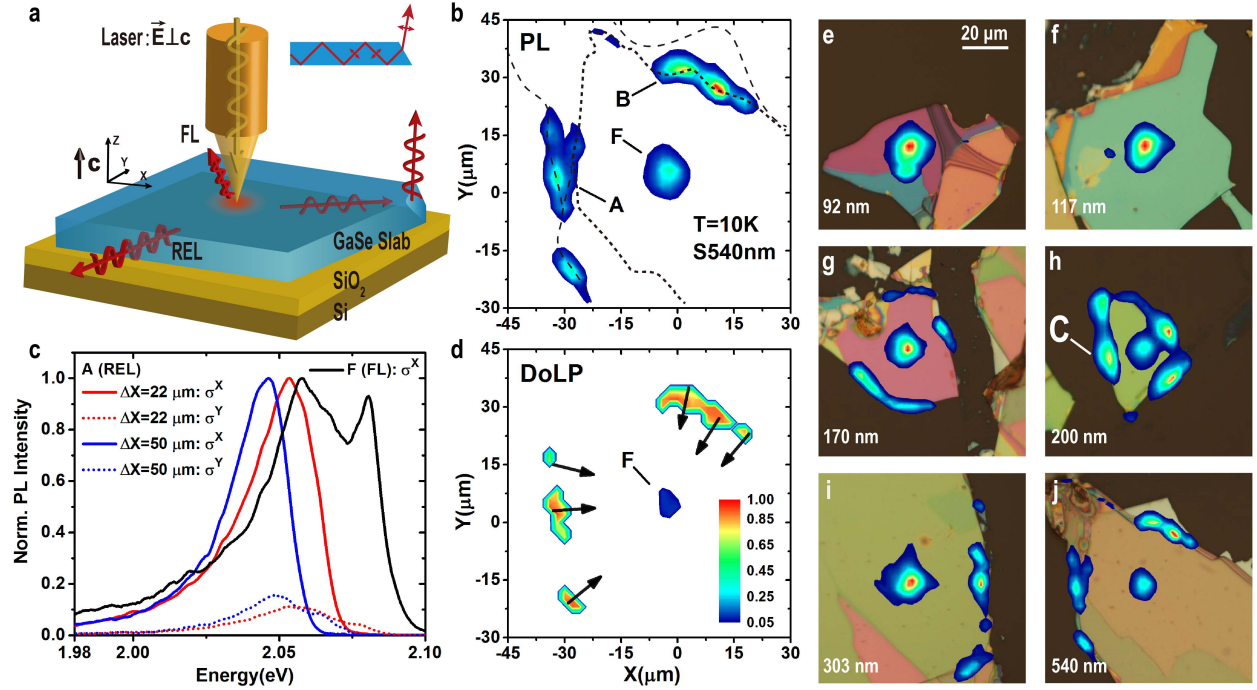


Figure 4.1 **Edge emission.** (a) Schematic of the optical setup. (b) Photoluminescence (PL) image of a 540 nm-thick GaSe slab at $T = 10$ K. The sample is optically pumped at the focal location F under a pump flux $P = 0.1 P_0$, where $P_0 = 2.6 \times 10^{14} \text{ cm}^{-2}$ per pulse. At P_0 , the photoexcited carrier density is about $3.4 \times 10^{17} \text{ cm}^{-3}$ ($2.7 \times 10^{10} \text{ cm}^{-2}$ per layer). The dashed lines represent the cleaved edges of the sample. Remote-edge luminescence (REL) emerges at cleaved edges tens of micrometers away from the photoexcited spot. (c) Polarized spectra of the focal luminescence (FL, black curve) and the REL (red and blue curves) from location A at distances (ΔX) from the photoexcited spot for $P = 0.15 P_0$. The spectra are normalized with respect to the X-polarized (σ^X) component. Both σ^X (TM mode, solid lines) and σ^Y (TE mode, dashed lines) spectral components red-shift with respect to the FL with increasing ΔX as a result of reabsorption. The two peaks in the FL spectrum are attributed to emission via exciton-exciton scattering (~ 2.08 eV) and localized excitons (~ 2.06 eV), respectively (see details in Appendix C). The FL is dominated by free excitons for $P \gtrsim 0.6 P_0$ (not shown). (d) Spatially resolved *DoLP* for $P = 0.1 P_0$. The false color and arrows represent the *DoLP* and polarization orientation, respectively. The measured maximal *DoLP* is about 0.93. The REL has a polarization oriented toward the photoexcited spot. (e–j) Overlay of optical and luminescence images of samples with thickness $d_L = 92, 117, 170, 200$ (S200nm), 303, and 540 (S540nm). The false colors in the luminescence images represent the relative intensities with the same scale used in (d). The remote-edge luminescence (REL) is visible only for $d_L \gtrsim 160$ nm. The central elliptical luminescence spot is the photoexcitation focal region.

The sample preparation and experimental setup have been discussed in Chap. 3. These GaSe dielectric slabs on SiO₂/Si form the simplest optical waveguides [149]. The thinnest GaSe that can sustain one guided transverse electric (TE) mode ($\vec{E} \perp c$) and transverse magnetic (TM) mode ($\vec{E} \parallel c$) for luminescence near the band edge (wavelength $\lambda \approx 600$ nm) is about 160 nm thick (see calculation in Appendix B). For a 540 nm-thick GaSe dielectric slab on SiO₂, about four guided TE modes and TM modes are allowed. In our experiment, the normally incident 2 ps optical excitation pulses create in-plane dipoles (d_{\perp}). The index-guided radiation propagates away from the photoexcited spot, and gets refracted out of the slab by irregular cleaved edges and collected by the objective. There are several scenarios one could expect for the REL's polarization. If the orientation of in-plane dipoles only randomize within the plane, i.e., there are no out-of-plane dipoles and TM radiation, the REL is expected to be linearly polarized with polarization orientation perpendicular to its propagation direction in the slab. In the presence of both TE and TM modes, the REL is expected to be unpolarized if the orientations of the photoexcited dipoles are totally random and isotropic. However, in Fig. 4.1a, we observed highly linearly polarized REL with orientation pointing to the excited spot, which must be from the guided TM mode of out-of-plane dipoles (d_{\parallel}). In the following, I will show that photoexcited d_{\perp} excitons are rapidly converted to d_{\parallel} dipoles through spin-flip of electrons or holes (Fig. 3.11 and 4.2). The guided TM mode of d_{\parallel} luminescence dominates over the TE mode of d_{\perp} luminescence because the radiative recombination rate of d_{\parallel} is about 30 times higher than that of d_{\perp} . As a result, highly linearly polarized TM mode luminescence emerges in the reflection geometry at cleaved edges when backscattering is allowed in the presence of irregularities.

In Fig. 4.1, we study the spectral and polarization characteristics of the REL from a 540 nm-thick (S540nm) GaSe slab under excitation energy $E_p = 2.138$ eV at $T = 10$ K. Spectrally, the REL shows an apparent red shift compared to the luminescence at the focal (photoexcited) spot (FL). Considering the REL as an index-guided mode of luminescence originating from the photoexcited spot, one can attribute the spectral redshift to anisotropic reabsorption [150] when luminescence propagates in-plane for a distance of tens of micrometers (Fig. 1c). Additionally, the REL is highly

linearly polarized ($DoCP \rightarrow 0.93$), whereas the FL is unpolarized under linearly polarized photoexcitation (Fig. 4.1d). The measured luminescence polarization image (Fig. 4.1d) indicates that the polarization orientations of the REL point toward the photoexcited spot. Moreover, depending on the location and sample thickness, the intensity (emission flux) of the REL can exceed that of the FL (Fig. 4.1f–j). Such a polarization orientation pattern and intensity distribution suggest that the REL originates from out-of-plane dipoles (d_{\parallel}), with the electric field vector parallel to the crystalline c -axis ($\vec{E} \parallel c$).

4.3 Time-resolved edge photoluminescence

To understand the unique polarization of the REL, we need to consider the selection rules and anisotropic optical constants in GaSe. We first examine the optical selection rules in GaSe and illustrate the spin-flip-induced conversion between the in-plane and out-of-plane dipoles (Fig. 4.2). The Se $4p_z$ -derived valence band maximum lies 1.2 and 1.6 eV above the Se $4p_{x,y}$ -derived valence band maxima as a result of the crystal field and spin-orbit interaction. Near the Γ point, direct optical transitions between the p_z -like uppermost valence band and s -like lowermost conduction band are dipole-allowed for light with electric field parallel to the c -axis ($\vec{E} \parallel c$). For light with $\vec{E} \perp c$, the otherwise dipole-forbidden transitions become weakly allowed due to spin-orbit interaction [147]. The spin-dependent optical selection rules can be best understood in the two-particle (exciton) representation (Fig. 4.2a) [29, 30]. Optical excitation with $\vec{E} \perp c$ creates excitons with Γ_6 symmetry (d_{\perp} dipoles), which is analogous to a triplet state ($\uparrow\uparrow$ and $\downarrow\downarrow$), where $\uparrow(\downarrow)$ and $\uparrow(\downarrow)$ represent the electron and hole with spin up(down), respectively. On the other hand, optical excitation with $\vec{E} \parallel c$ results in excitons with Γ_4 symmetry (d_{\parallel} dipoles), which is analogous to a singlet state ($\uparrow\downarrow - \downarrow\uparrow$). Therefore, a spin flip of either electron or hole of the exciton (e - h pair) results in the conversion between d_{\perp} and d_{\parallel} (Fig. 4.2b).

Experimentally, the absorption coefficient near the band edge for $\vec{E} \perp c$ is about $3 \times 10^{-3} \text{ cm}^{-1}$, which is a factor of 1/30 of that for light with $\vec{E} \parallel c$ [110]. Assuming that the spontaneous

radiative recombination rate is proportional to the absorption coefficient, we approximate the relative radiative recombination rates of the in-plane and out-plane dipoles to be $W_{\parallel}^r/W_{\perp}^r \approx 30$. As a result, under picosecond excitation, luminescence is dominated by the radiative recombination of d_{\parallel} when the conversion between d_{\perp} and d_{\parallel} is fast compared with the recombination rates. The linear polarization of the REL is expected to be approximately $(W_{\parallel}^r - W_{\perp}^r)/(W_{\parallel}^r + W_{\perp}^r) \approx 0.94$, which is consistent with the measured *DoLP*.

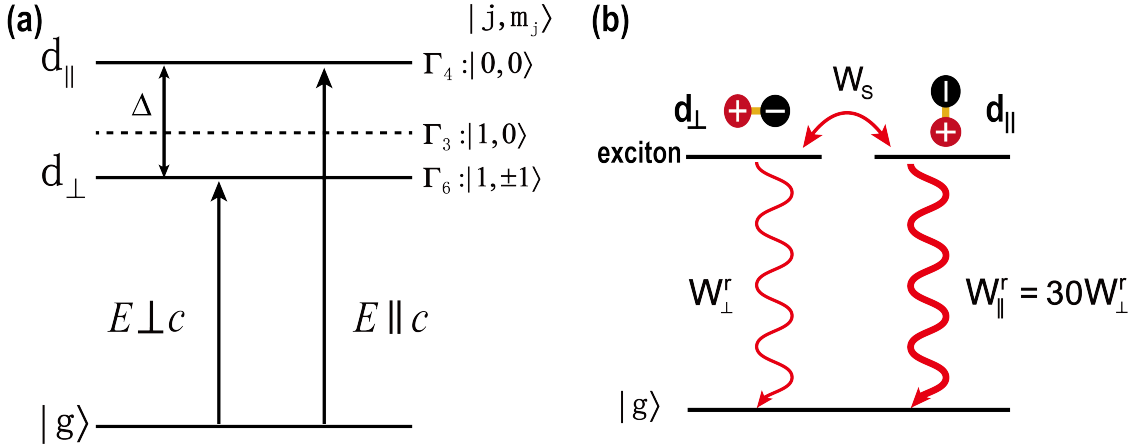


Figure 4.2 **The schematic model of transitions between triplet (d_{\perp}) and singlet (d_{\parallel}) excitons.** (a) Schematic of the exciton levels in ε -GaSe at the Γ point and the representations to which the states at the Γ -point belong when including spin-orbit interaction (see Fig. 1.1). The energy splitting Δ between the Γ_4 (d_{\parallel}) and Γ_6 (d_{\perp}) exciton states is approximately 2 meV [29, 30]. (b) Schematic of the rate equation model. W_s represents the transition rate between d_{\perp} and d_{\parallel} excitons. W_{\perp}^r and W_{\parallel}^r represent the radiative recombination of d_{\perp} and d_{\parallel} excitons, respectively.

In Fig. 4.3, we illustrate the spectral and dynamic characteristics of the REL at room temperature. The REL remains highly linearly polarized, with a polarization orientation pointing to the photoexcited spot. The FL and REL show no identifiable relative time delay. Therefore, the REL cannot originate from carriers that are photoexcited at the focal spot and transported to the cleaved edges. We attribute the REL to the back scattered light from an index-guided optical TM mode with $\vec{E} \parallel c$. The radiation from d_{\parallel} excitons converted from the photoexcited d_{\perp} excitons radiates into this TM mode and propagates in-plane from the photoexcited spot to the cleaved edges at the speed of light in the GaSe slab. The sub-10-ps rise time of the REL in Fig. 4.3 indicates that energy relaxation and conversion of photoexcited d_{\perp} and d_{\parallel} are faster than 10 ps at room temperature

[29, 30, 105].

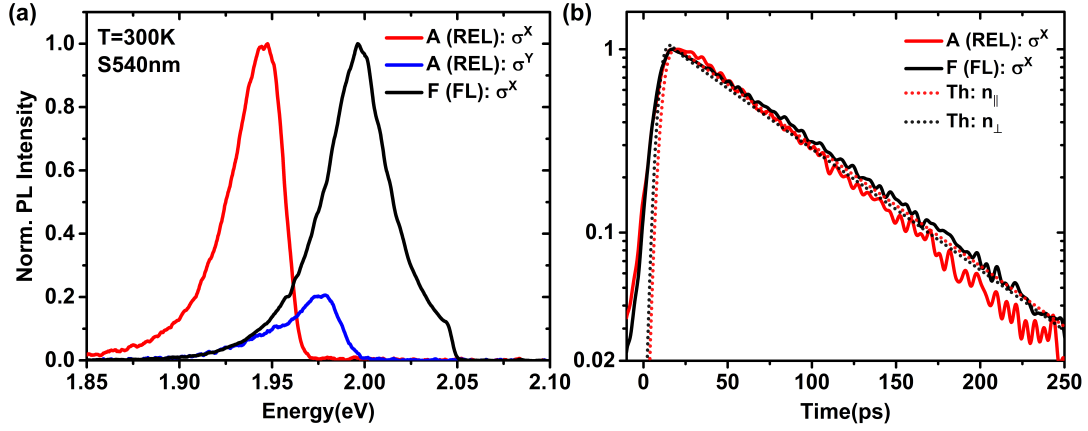


Figure 4.3 **PL dynamics of focal and edge emission.** (a) Polarized spectra of the FL (black curve) and the REL from location A (red and blue curves) in a 540 nm-thick GaSe slab at room temperature. The pump energy is $E_p = 2.087$ eV, and the pump flux is $P = 1.0 P_0$. At room temperature, the FL is largely due to free excitons, and the backscattered REL intensity is considerably weaker than the FL (about a factor of four here). The $DoLP$ is above 0.93 for $E < 1.95$ eV, where the anisotropic reabsorption for σ^X (TM mode) and σ^Y (TE mode) is negligible. (b) Time-dependent FL and REL. The FL (solid black curve) and the REL (solid red curve) show similar rise and decay times. The dotted black (red) curve is the calculated n_{\perp} (n_{\parallel}), which corresponds to the time-dependent luminescence from d_{\perp} (d_{\parallel}) dipoles. The theoretical curves are calculated with a rate equation model and convolved with an 8 ps (FWHM) instrument response. The fitting parameters are as follows: $W_{\perp}^r = 1/1000$, $W_{\parallel}^r = 30 W_{\perp}^r$, $W_S = 1/3$ [ps^{-1}].

The spin-flip-induced conversion between the in-plane and out-of-plane dipoles is evident in the time-dependent PL measurements at cryogenic temperature ($T = 10$ K), where the spin-flip rate is significantly reduced (Fig. 4.4). The FL arises within 10 ps of the pulsed excitation, whereas the REL reaches its maximum about 50 ps afterward. The nearly instantaneous rise of the FL is the result of a sub-5-ps energy/momentum relaxation of photoexcited carriers, whereas the considerable delay of ~ 30 –50 ps in the rise time of the REL is due to the ~ 30 ps spin-flip time constant at $T = 10$ K.

Our model for the time- and spin-dependent dynamics of the lowest-energy excitons has been described elsewhere [106]. In the case that either $k_B T$ or the inhomogeneous linewidth (Γ_h) of the exciton transitions is much larger than Δ , the polarized time-dependent luminescence is reproduced

by a simplified model in which the spin-flip rates $W_{\parallel,\perp}$, describing scattering from d_{\perp} to d_{\parallel} , and $W_{\perp,\parallel}$ are set equal to one another. Considering a spin-flip process and anisotropic radiative recombination rates for the in-plane and out-of-plane dipoles, we describe the time-dependent FL and REL with the following set of coupled differential equations:

$$\begin{aligned}\dot{n}_{\perp}(t) &= -W_{\perp}^r n_{\perp}(t) - W_S [n_{\perp}(t) - n_{\parallel}(t)] + G(t)P, \\ \dot{n}_{\parallel}(t) &= -W_{\parallel}^r n_{\parallel}(t) + W_S [n_{\perp}(t) - n_{\parallel}(t)].\end{aligned}$$

The optical generation rate $G(t)P$ is approximated by a 2 ps Gaussian pulse $G(t)$, with pump flux P . n_{\perp} and n_{\parallel} are the populations of the in-plane (d_{\perp}) and out-of-plane (d_{\parallel}) dipoles, and W_{\perp}^r and W_{\parallel}^r are the corresponding radiative recombination rates. W_S is the spin-flip rate that leads to the conversion between d_{\perp} and d_{\parallel} . In this simple model, we neglect the energy relaxation of nonresonantly excited carriers and non-radiative recombination loss. The time-dependent REL agrees with the calculated temporal evolution of n_{\parallel} , and indicates a rise time of ~ 30 ps that is consistent with the previously measured spin-flip time constant $\tau_s \approx 1/W_S$ (Ref. [105] and Chap. 3). Similarly, the time-dependent FL is associated with the temporal evolution of n_{\perp} . When $\Gamma_h, k_B T \lesssim \Delta$, one must account for the differences in spin-flip rates $W_{\parallel,\perp}$ and $W_{\perp,\parallel}$. For the experimental conditions considered here, though, $\Gamma_h \approx \Delta$ [151] yielding results similar to those obtained from the simplified equations above.

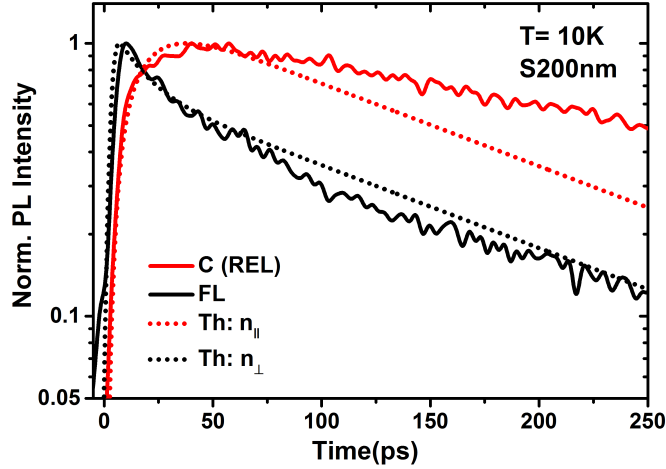


Figure 4.4 **Time-dependent FL (solid black line) and REL (solid red line) in a 200 nm-thick sample (S200nm).** The REL is measured at location C, as indicated in Fig. 1h. The dotted black (red) line is the calculated time-dependent n_{\perp} (n_{\parallel}) convolved with a 4 ps (FWHM) instrument response function. The fitting parameters are as follows: $W_{\perp}^r = 1/2000$, $W_{\parallel}^r = 30 W_{\perp}^r$, $W_S = 1/30$ [ps^{-1}]. The slower decay of the REL relative to the FL is likely due to reabsorption, which results in the dominance of the REL by the low energy portion of the exciton luminescence.

4.4 Discussion

Anisotropic absorption and TE polarized emission of excitons have also been observed for light propagating in the quantum-well plane in GaAs-based structures. In the absence of mixing of the heavy-hole and light-hole bands, the emission from heavy-hole excitons propagating in the quantum-well plane (in-plane) is expected to be transverse-electric (TE) polarized [152]. In practice, a sample with quantum wells imbedded in a proper waveguide structure is required for the observation of remote polarized edge emission [153, 154, 155, 156]. For example, the edge emission from GaAs-AlGaAs multiple quantum wells in a waveguide structure was measured to be TE polarized with a degree of linear polarization about 0.8 under excitation near or in resonance with heavy-hole excitons [153, 154]. The reduced linear polarization as compared to the ideal unity linear polarization [152, 157] was attributed to the presence of valence sub-bands with mixed $M_j = \pm 3/2$ (heavy-hole) and $M_j = \pm 1/2$ (light-hole) characters [153].

Lasing [158, 159] or an enhanced spontaneous emission rate [160, 161, 162, 163] has been observed for atomically thin TMDs integrated with a microcavity (Fabry-Pérot [160, 161], photonic crystals [162, 163, 158], or microdisk [159]). One can anticipate linearly polarized stimulated emission or lasing in microdisks with a thickness of $\sim 200\text{-}300$ nm and a lateral size of several micrometers when optical cavity effects are enhanced and non-radiative annihilation processes are suppressed [164]. Here, the GaSe layers can provide both gain and optical confinement and in principle should allow for in-plane integration with other photonic components [165, 166, 167].

4.5 Conclusion

In summary, we have observed highly linearly polarized remote-edge luminescence (REL) in GaSe platelets with a thickness of 160 nm or more. The REL measured in the reflection geometry has a degree of linear polarization above 0.90, with polarization orientation pointing toward the photoexcitation spot. The REL is dominated by an index-guided optical mode that is linearly polarized along the crystalline *c*-axis. We reveal this luminescence as transitions from in-plane dipoles to out-of-plane dipoles through a spin-flip process with a time constant of 30 ps at the excitation spot.

CHAPTER 5

SECOND-ORDER OPTICAL NONLINEARITY IN ATOMICALLY THIN GaSe CRYSTALS

5.1 Introduction

Two-dimensional semiconductors such as graphene and transition metal dichalcogenides (TMDs), e.g., MoS₂, WS₂, and WSe₂, have been studied intensively as potential materials to complement silicon electronics and gallium arsenide optoelectronics. A recent trend in the search for new two-dimensional systems is the isolation and study of atomically thin sheets of layered materials. Similar to graphene and TMDs, gallium monochalcogenide nanoslabs from atomic thickness to hundreds of layers can be prepared by mechanical exfoliation. Gallium monochalcogenides have a quasi-direct band gap in bulk with the valence band maximum at the Γ point and the conduction band minimum near the M point but only about 10 meV below the local minimum at the Γ point [40, 38, 46, 47, 43]. This quasi-direct band gap makes them versatile materials in which strong emission occurs and spin polarization can potentially be controlled from bulk to atomically thin crystals [105, 148, 106]. For example, as shown in Chap. 3, the unique band structure of GaSe allows generation and preservation of a high degree of spin polarization for both electrons and holes [29, 30, 105, 148, 106, 34, 35].

In contrast to TMDs, atomically thin GaSe crystals are expected to undergo a direct-to-indirect-band-gap transition, where the quasi-bottom of the conduction band remains at the Γ point, but the maximum of the uppermost valence band (UVB) moves away from the Γ point and forms a Mexican-hat-like structure in mono- and few-layer GaSe [33, 34, 35]. As spin degeneracy can be lifted at the maximum of the UVB of mono- and few-layer GaSe due to broken inversion symmetry, spin can be locked to the valley, and atomically thin GaSe slabs become an interesting platform to explore valley physics, as in the case of monolayer TMDs [11, 12, 13]. Associated with such unique valence structure, theorists [36] recently predicted that the spin degeneracy can be totally

cancelled over the whole Brillouin zone by hole doping, and consequently a ferromagnetic phase forms in monolayer GaSe, which can be tuned by the hole-doping level.

In this chapter, we explore the thickness-evolution of the electronic structure by measuring the second-harmonic response of exfoliated GaSe using a large range of sub-band-gap fundamental photon energies with corresponding second-harmonic photon energies spanning from 0.3 eV below to 1.0 eV above the bulk band gap. By accounting for wavelength-dependent interference, we are able to reproduce the frequency- and thickness-dependence of the SHG signal from samples of ~ 7 to ~ 100 L with a susceptibility $|\chi^{(2)}| = 80 \pm 18$ pm/V, similar to the reported bulk value of $|\chi^{(2)}| = 2|d_{22}| = 108 \pm 21.6$ pm/V [25]. However, for crystals $\lesssim 7$ L, we observe a suppression of the nonlinear susceptibility by as much as a factor of ~ 5 at 3 L. The latter observation is qualitatively consistent with a report on SHG from mechanically exfoliated GaSe crystals from 2 to 10 layers thick excited with a fundamental photon energy of 1.55 eV [168]. Contrary to a recent report of an enhanced $\chi^{(2)}$ in monolayer CVD-grown GaSe [169], we do not observe an increase in the efficiency of SHG or $\chi^{(2)}$ for monolayer GaSe. The results and discussion can be also found in Ref. [170].

5.2 Experimental method

5.2.1 Sample exfoliation and characterization

ϵ -GaSe is grown with the Bridgman method by Krishna C. Mandal [107]. The Scotch-tape method is used to exfoliate thin slabs of GaSe. Among all Scotch tapes, we found that the Magic brand of tape is the best one for high yield of thin and large slabs. The exfoliated slabs are transferred to a Si wafer with 90 nm SiO₂ and position markers. The detailed procedure for sample exfoliation is presented in Appendix A. The key thing to keep in mind during the exfoliation of GaSe is that GaSe is so fragile that strain on the samples will easily break samples into small thick pieces (Fig. 5.1a). This is in contrast to the case of graphene exfoliation where people use their fingers to press the tape with graphene onto the substrate. The process of unfolding the tape and peeling the tape

off the substrate must be smooth, slow, and gentle. I use a z-axis translation stage to control the speed of unfolding and peeling. When placing the tape onto the substrate, no force should be applied to the area with samples. Generally, I just use the tip of a tweezer to press the sample-free area to increase the contact between the nearby samples and substrate. With all these tricks, I can easily get few-layer samples with size $\geq 10 \mu\text{m}$ (Fig. 5.1b). However, the exfoliation yield of monolayer GaSe is still low (about one out of 50 substrates). Further possible tricks for exfoliation of layered materials can be found in the study by Huang et al. [171]. We identify single- and few-layer GaSe crystals using an optical microscope. Their thickness are determined by using an atomic force microscope (AFM) operated in the contact mode rather than tapping mode, as the thickness determined by tapping mode is sensitive to setting parameters [172, 173], especially free amplitude. We use AFM tips with a frequency of 13 KHz and stiffness of 0.2 N/m due to the high measurement reproducibility.

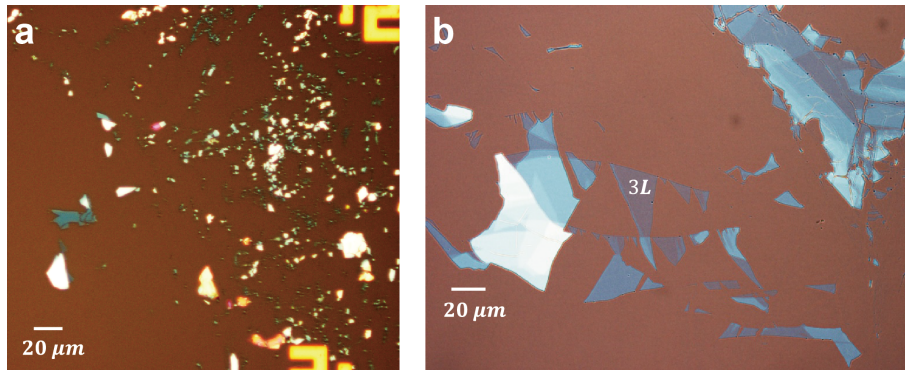


Figure 5.1 **Optical microscopic images showing results of exfoliation by different approaches.** (a) Samples are exfoliated by rapid unfolding and peeling. (b) Samples are exfoliated by the procedure in the main text.

In Fig. 5.2a-f, we show optical and AFM images of mono-, bi-, and tri-layer nanoslabs. The AFM measurement (Fig. 5.2g) gives a thickness of $0.85 \pm 0.1 \text{ nm}$ for monolayer GaSe, which is consistent with previous studies [169] of CVD-grown monolayer GaSe. The thicknesses of 2 L and 3 L nanoslabs (Fig. 5.2h,i) are about an integer multiple of that of 1 L, $1.5 \pm 0.1 \text{ nm}$ and $2.4 \pm 0.1 \text{ nm}$, respectively.

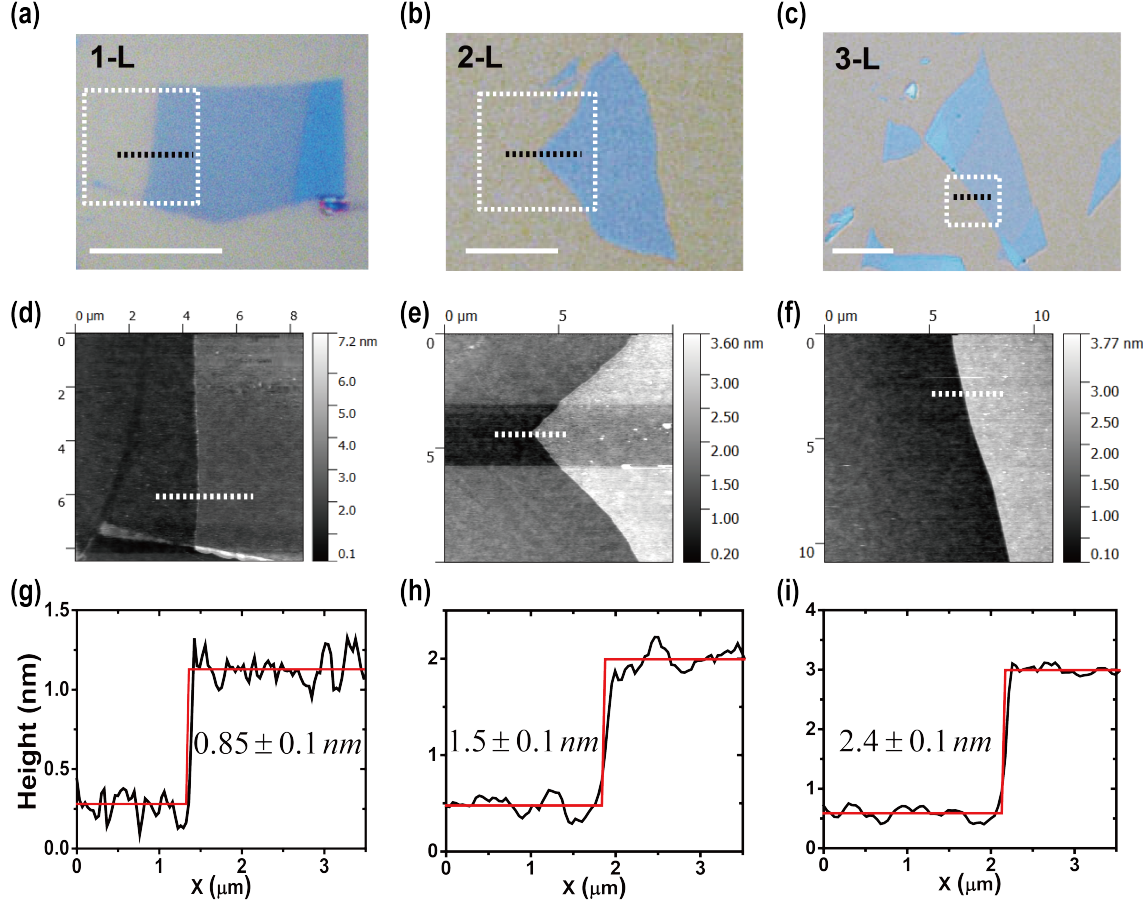


Figure 5.2 **AFM measurements of mono- and few-layer GaSe crystals.** Optical (a-c) and atomic force microscopic (d-f) images of mono-, bi-, and tri-layer GaSe deposited onto a Si substrate with a 90 nm SiO_2 layer. The white dashed squares in (a-c) represent the AFM region, shown in (d-f). The AFM traces (g-i) corresponding to the white dashed lines (d-f) reveal thicknesses of 0.85 ± 0.1 , 1.5 ± 0.1 , and 2.4 ± 0.1 nm.

5.2.2 SHG setup

In this study, we applied second-harmonic generation (SHG) to explore the evolution of the electronic structure in single- and few-layer GaSe. SHG is a nonlinear optical process, in which photons with twice the frequency of the fundamental field are generated in a nonlinear material. SHG by dipolar transitions only occurs in noncentrosymmetric systems, such as surfaces and non-centrosymmetric crystals. SHG is a powerful tool for probing crystal structures [174] and resolving the electronic structures [175, 176, 177]. For example, the efficiency of SHG in WSe_2 at low temperature was shown to be enhanced by about three orders of magnitude when the SHG

photon energy is in resonance with the 1s exciton peak [175]. ϵ -GaSe crystals belong to the non-centrosymmetric D_{3h} point group and so can allow nonvanishing SHG in an arbitrary number of layers. This is in contrast to TMDs, in which SHG is only efficient for crystals with an odd number of layers [178, 179, 180] and does not increase with layer thickness for odd numbers of layers. The suppressed photoluminescence in thin GaSe (Fig. 3.6) and small absorption coefficient for normally incident light [26] makes it difficult to use other techniques, like photoluminescence, absorption, and reflection spectra, to explore the electronic structure in mono- and few-layer GaSe.

In Fig. 5.3, we show a schematic layout of the SHG setup. SHG in reflection is generated with a fundamental pump wavelength of $\lambda = 785$ nm (1.58 eV) from a 2-ps pulsed Ti:sapphire oscillator (Coherent Mira 900D) or $\lambda > 800$ nm (< 1.55 eV) from a supercontinuum white-light laser (NKT Photonics SuperK EXTREME EXB-6). A reflective microscope objective with numerical aperture NA = 0.5 is used to focus the fundamental pump laser beam and to collect the SHG signal in the reflection geometry. The polarization of the pump is defined by a wire-grid polarizer (Thorlabs, WP25M-UB) that is devoid of beam walk-off during its rotation, which is important because a small mirror (~ 2 mm) is used to reflect the pump through the objective. The orientation of the polarizers is kept orthogonal or parallel during the measurements (see details in Sec. 5.4). The samples are maintained in vacuum (10^{-5} Torr) to minimize degradation from oxidation or water contamination.

To confirm the quadratic power-dependence of SHG, we measure the power-dependent SHG by a fundamental with $\lambda = 785$ nm (Fig. 5.5a). The power of the fundamental is controlled by liquid-crystal-based devices (Sec. 3.2.2). To confirm the crystalline symmetry, we measure the polarized SHG by rotating the polarization of the fundamental in the x - y plane and collecting the orthogonally polarized SHG signal (Fig. 5.5b). To maintain a constant pump power, the fundamental polarization is changed by a polarization compensator from linear to circular before the wire-grid polarizer (Sec. 3.2.2). The polarization-dependent detection efficiency of the spectroscopic and optical collection system is calibrated with a 400 nm laser. In this set of polarized SHG measurements, the fundamental pump laser beam with an incident angle of less than 8° and

a flux of 7.5×10^{-2} nJ per pulse is focused to a spot of $2.6 \mu\text{m}$ radius. For layer-dependent SHG measurements, the SHG signals are averaged over four polarizations of the fundamental pump to avoid any potential anisotropic issues, namely $\psi = 0^\circ, 45^\circ, 90^\circ$ and 135° , where ψ is the polarization angle of the fundamental with respect to the x -axis (horizontal axis in the laboratory frame). We further determine the frequency-dependent SHG using the supercontinuum laser as the fundamental pump. The value of the nonlinear susceptibility of each GaSe sample is determined by comparing to the reflected SHG signal from the upper surface of a thick (>4 mm) BBO crystal, for which reflections from the other surface are unimportant, under identical pump flux and spot size.

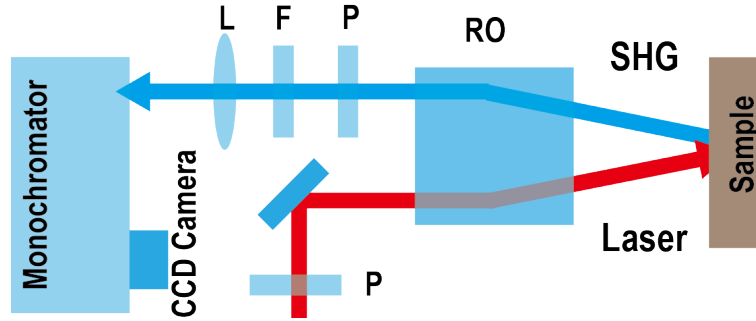


Figure 5.3 **The schematic layout of the SHG setup.** P, F, L and RO respectively represent polarizer, short-pass filter, lens ($f=100$ mm) and UV-enhanced reflective objective ($f=4$ mm, LMM-40X-UVV-160).

5.3 Calculation of reflected SHG in a multilayer system

The most usual procedure for describing nonlinear optical phenomena is based on expressing the polarization $\vec{P}(n\omega)$ (n is integer and equals 2 in this case) in terms of the fundamental field $\vec{E}(\omega)$. $\vec{P}(n\omega)$ acts as the source of n^{th} harmonic waves. In eq. 5.1, we write the second-order nonlinear

polarization as a general function of the fundamental field:

$$\begin{bmatrix} P_x(2\omega) \\ P_y(2\omega) \\ P_z(2\omega) \end{bmatrix} = 2\epsilon_0 \begin{bmatrix} d_{11} & d_{12} & d_{13} & d_{14} & d_{15} & d_{16} \\ d_{21} & d_{22} & d_{23} & d_{24} & d_{25} & d_{26} \\ d_{31} & d_{32} & d_{33} & d_{34} & d_{35} & d_{36} \end{bmatrix} \begin{bmatrix} E_x(\omega)^2 \\ E_y(\omega)^2 \\ E_z(\omega)^2 \\ 2E_y(\omega)E_z(\omega) \\ 2E_x(\omega)E_z(\omega) \\ 2E_x(\omega)E_y(\omega) \end{bmatrix} \quad (5.1)$$

where d_{ij} is the second-order nonlinear optical coefficient, which is conventionally related to the second-order nonlinear susceptibility $\chi^{(2)}$ by $d = \frac{1}{2}\chi^{(2)}$ [181]. In the case of the D_{3h} point group,

$$\overset{\leftrightarrow}{d} = \begin{bmatrix} 0 & 0 & 0 & 0 & 0 & -d_{22} \\ -d_{22} & d_{22} & 0 & 0 & 0 & 0 \\ 0 & 0 & 0 & 0 & 0 & 0 \end{bmatrix}$$

The multilayer system in this study consists of vacuum(V), GaSe(G), SiO₂(O), and Si(S), as shown in Fig. 5.4. The second-order polarization $\vec{P}^{(2)}$ is given as

$$\vec{P}^{(2)} = \vec{P}_{ff} + \vec{P}_{bb} + 2\vec{P}_{fb} \quad (5.2)$$

where, for example, $\vec{P}_{fb} \equiv \overset{\leftrightarrow}{\chi}^{(2)} : \vec{E}_{G,f}^\omega \vec{E}_{G,b}^\omega$, and $\vec{E}_{G,f}^\omega$ and $\vec{E}_{G,b}^\omega$ are the homogeneous waves at frequency ω propagating in GaSe in the $+z$ (forward) and $-z$ (backward) directions respectively. Since the depth of field (about 10 μm) is much larger than the coherence length of the SHG radiation (about 0.1 μm), we use the plane-wave approximation. We label quantities associated with the fundamental fields with a superscript ω ; otherwise, the quantities are taken to be associated with the SH fields. For symmetry class $D_{3h}^1 - \bar{6}m2$ and fundamental light propagating along the crystalline c -axis, the sum of the SHG power measured with SH polarization alternately parallel and perpendicular to the fundamental is independent of sample orientation. Since the angle of incidence in vacuum is small ($\theta_V^\omega \equiv \theta_V \approx 8^\circ$), it is sufficient to calculate $\vec{P}^{(2)}$ for fundamental electric field polarization along the GaSe x -axis (a -axis), for which $\vec{P}^{(2)} = P^{(2)}\hat{y}$.

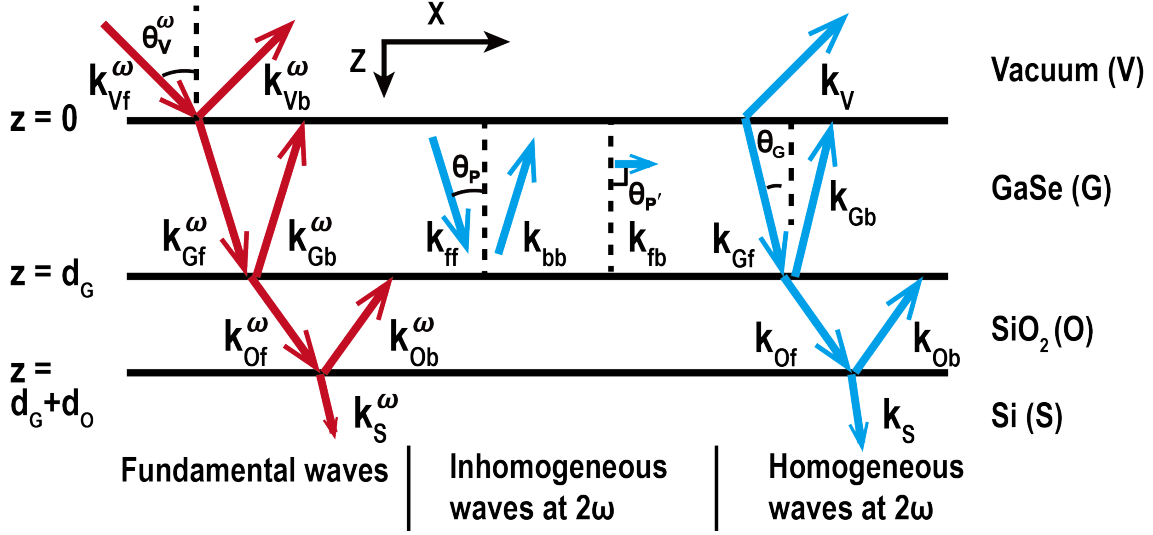


Figure 5.4 **Nonlinear waves in the multilayer structure.** See main text for labelling conventions

Calculation of the reflected SHG power as a function of sample thickness and wavelength amounts to solving a pair of boundary value problems: One for the fundamental field and one for the SHG field. In particular, since the generation of the second-harmonic waves negligibly depletes the fundamental field, the determination of the fundamental electric field in the GaSe layer is just a standard boundary value problem for the homogeneous wave equation. For a given value of $\chi^{(2)}$, the fundamental field in the GaSe layer then directly yields the second-order polarization $P^{(2)}$ (i.e., the inhomogeneous waves in Fig. 5.4) via Eq. 5.2. The electromagnetic field at 2ω in each medium (i.e., the homogeneous SH waves in Fig. 5.4) is then determined by solving the boundary value problem for the inhomogeneous wave equation for the electromagnetic field at 2ω . The SH electric and magnetic fields E_y and H_x (we hereafter drop the directional subscripts) at the upper and lower boundaries of medium $n = V, G, O, S$ are given by identical equations as for the fundamental fields, except for the addition of the inhomogeneous terms in GaSe:

$$E_n = E_{n,f} \exp(i\phi_n) + E_{n,b} \exp(-i\phi_n) + 4\pi \left[\frac{P_{ff} \exp(i\phi_P) + P_{bb} \exp(-i\phi_P)}{\epsilon_P - \epsilon_G} + \frac{2P_{fb}}{\epsilon_{P'} - \epsilon_G} \right] \delta_{n,G}$$

$$H_n = \epsilon_n^{1/2} \cos \theta_n [E_{n,f} \exp(i\phi_n) - E_{n,b} \exp(-i\phi_n)] + 4\pi \epsilon_P^{1/2} \cos \theta_P \frac{P_{ff} \exp(i\phi_P) - P_{bb} \exp(-i\phi_P)}{\epsilon_P - \epsilon_G} \delta_{n,G},$$

where $\delta_{n,G}$ is the Kronecker delta. We define $\phi_n = \phi_{n,ff} = \phi_{n,bb} \equiv 0$ at the upper surface of

each medium $n = G, O, S$ as well as the lower surface of the vacuum. At the lower surface of each medium, $\phi_n = |k_{n,z}| d_n = 2\varepsilon_n^{1/2} d_n \omega c^{-1} \cos \theta_n$ ($n = P, G, O$), where d_n is the thickness of the corresponding medium ($d_P = d_G$), θ_n is the angle of \vec{k}_n with respect to the surface normal, and c is the speed of light. In particular, the variation of ϕ_G with the number of GaSe layers will result in pronounced interference patterns. For the SH field, we also have $E_{V,f} = E_{S,b} = 0$, i.e., there is no incident SH field in vacuum or reflected SH field from the far side of the thick substrate.

The propagation directions of the homogeneous waves are determined by Snell's law or conservation of momentum parallel to the surface, given as

$$\sin \theta_V = \varepsilon_n^{1/2} \sin \theta_n \quad (n = V, G, O, S), \quad (5.3)$$

where θ_n and ε_n are respectively the refracted or reflected angles and the dielectric constant of the waves at ω or 2ω in medium n . For the inhomogeneous waves at 2ω , the angle θ_P of $\vec{P}_{ff(bb)}$ is the same as the refracted angle of the fundamental field at ω in the GaSe slab, while the refracted angle $\theta_{P'}$ of $\vec{P}_{fb} = \vec{P}_{bf}$ is 90° , as required by momentum conservation. The effective dielectric constants ε_P and $\varepsilon_{P'}$ of $\vec{P}_{ff(bb)}$ and \vec{P}_{fb} , respectively, are given by $\varepsilon_{P(P')}^{1/2} = \sin \theta_V / \sin \theta_{P(P')}$.

The measured SH signal is given by the intensity: $I_V = \frac{1}{2} \varepsilon_0 c |E_V|^2$, where $E_V = E_{V,b}$. Matching E_n and H_n across each of the three interfaces yields six equations from which we can determine the six unknown fields $E_{n,f}$ and $E_{n,b}$. The explicit form for E_V is

$$E_V = \left\{ \begin{aligned} & \left[2\varepsilon_G^{1/2} \cos \theta_G M_{ff} + \frac{4\pi\varepsilon_G^{1/2} \cos \theta_G (M_{mb} - 1)}{\varepsilon_P - \varepsilon_G} - \frac{4\pi\varepsilon_P^{1/2} \cos \theta_P (M_{mb} + 1)}{\varepsilon_P - \varepsilon_G} \right] \cdot P_{ff} + \\ & \left[-2\varepsilon_G^{1/2} \cos \theta_G M_{bb} + \frac{4\pi\varepsilon_G^{1/2} \cos \theta_G (M_{mb} - 1)}{\varepsilon_P - \varepsilon_G} + \frac{4\pi\varepsilon_P^{1/2} \cos \theta_P (M_{mb} + 1)}{\varepsilon_P - \varepsilon_G} \right] \cdot P_{bb} + \\ & \left[-2\varepsilon_G^{1/2} \cos \theta_G M_{fb} + \frac{8\pi\varepsilon_G \cos \theta_G (M_{mb} - 1)}{\varepsilon_{P'} - \varepsilon_G} \right] \cdot P_{fb} \left. \right\} \times \\ & \left[\varepsilon_G^{1/2} \cos \theta_G (M_{mb} - 1) + \varepsilon_V^{1/2} \cos \theta_V (M_{mb} + 1) \right]^{-1} \end{aligned} \right. \quad (5.4)$$

where

$$\begin{aligned}
M_{ff} &= \frac{(1+T)\varepsilon_P^{1/2} \cos \theta_P - (1-T)\varepsilon_O^{1/2} \cos \theta_O}{(1+T)\varepsilon_G^{1/2} \cos \theta_G - (1-T)\varepsilon_O^{1/2} \cos \theta_O} \times \frac{4\pi}{\varepsilon_P - \varepsilon_G} \exp[-i(\phi_G - \phi_P)] \\
M_{bb} &= \frac{(1+T)\varepsilon_P^{1/2} \cos \theta_P + (1-T)\varepsilon_O^{1/2} \cos \theta_O}{(1+T)\varepsilon_G^{1/2} \cos \theta_G - (1-T)\varepsilon_O^{1/2} \cos \theta_O} \times \frac{4\pi}{\varepsilon_P - \varepsilon_G} \exp[-i(\phi_G + \phi_P)], \\
M_{mb} &= \frac{(1+T)\varepsilon_G^{1/2} \cos \theta_G + (1-T)\varepsilon_O^{1/2} \cos \theta_O}{(1+T)\varepsilon_G^{1/2} \cos \theta_G - (1-T)\varepsilon_O^{1/2} \cos \theta_O} \times \exp(-2i\phi_G), \\
M_{fb} &= \frac{(1-T)\varepsilon_O^{1/2} \cos \theta_O}{(1+T)\varepsilon_G^{1/2} \cos \theta_G - (1-T)\varepsilon_O^{1/2} \cos \theta_O} \times \frac{8\pi}{\varepsilon_{P'} - \varepsilon_G} \exp(-i\phi_G), \\
T &= \frac{\varepsilon_O^{1/2} \cos \theta_O - \varepsilon_S^{1/2} \cos \theta_S}{\varepsilon_O^{1/2} \cos \theta_O + \varepsilon_S^{1/2} \cos \theta_S} \times \exp(2i\phi_O),
\end{aligned}$$

and the nonlinear polarization terms P_{ff} , P_{bb} , and P_{fb} are given by Eq. 5.2. For a given $\chi^{(2)}$, these can be calculated easily by solving the corresponding interference problem for the fundamental fields in the multilayer system.

Given a constant incident fluence and known refractive index[110], we can determine the value of $|\chi^{(2)}|$ by fitting the measured layer-dependent SHG power with the above model.

5.4 Power- and polarization-dependent SHG

The quadratic power-dependent nature of SHG is confirmed in Fig. 5.5a, where the power-law fitting reveals a power-dependence (not shown) of $\mathcal{P}^{SH} \propto (\mathcal{P}^\omega)^{1.96 \pm 0.01}$ (the error is just from fitting), where \mathcal{P}^{SH} and \mathcal{P}^ω are the power of the SHG radiation and the fundamental field, respectively. In Fig. 5.5b, we show the experimental polarization-dependence of the SHG for 1 L, where the SHG power is plotted as a function of ψ . The SHG response from the GaSe nanoslabs exhibits the six-fold angular-dependence expected for the D_{3h} symmetry of ε -GaSe. The data are fitted with the function $I_{SH} = (I^\omega)^2 \sin^2(3\psi + \psi_0)$, which follows from Eq. 5.1, where I_{SH} is the reflected SHG power.

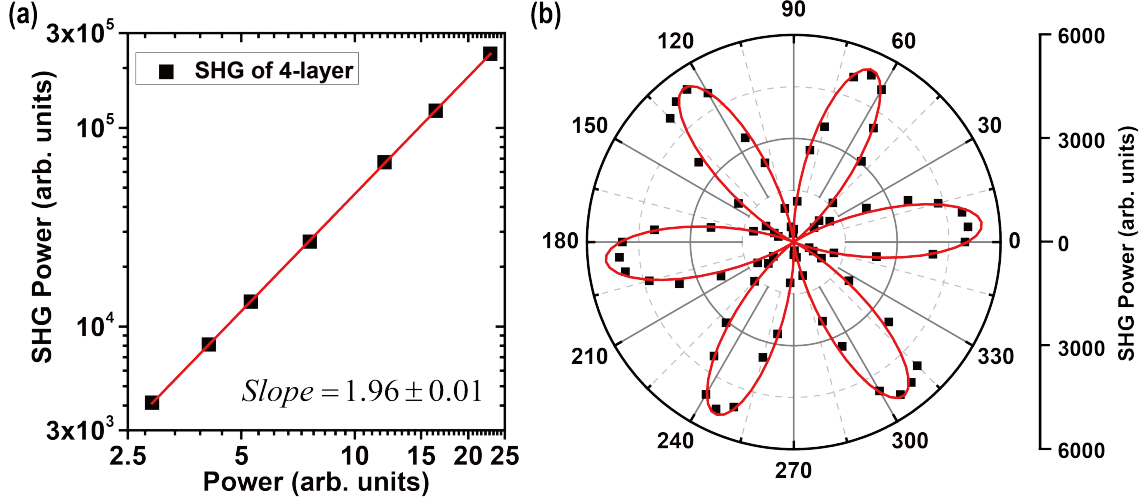


Figure 5.5 **Power- and polarization-orientation-dependent SHG.** (a) The typical quadratic power-dependence of the SHG intensity from a thin GaSe slab (here 4 layers), revealing a quadratic power dependence. (b) The SHG polarization pattern for orthogonally polarized fundamental and second harmonic.

5.5 Layer-dependent SHG with 785 nm excitation

In Fig. 5.6, we show the layer-dependent SHG for a fundamental input with $\lambda = 785$ nm from GaSe nanoslabs ranging from 1 L to > 100 L excited by a fundamental field at 785 nm. For thickness ≤ 10 L, the error bars represent the sample-to-sample variance, about $\pm 50\%$, of the average SHG power. The large variance might be related to photon-induced damage to samples. For samples of thickness > 10 L, which generally have a lateral size $> 20 \mu\text{m}$, the error bars represent the typical position-to-position variance, about $\pm 30\%$, of the SHG power from the same nanoslab. The dashed curve is a least-squares fit to the data for thickness ≥ 10 L according to the model described in Sec. 5.3, which yields $|\chi^{(2)}| = 78 \pm 17$ pm/V. In samples with thickness $d_G \geq 7$ L, the SHG power reaches a maximum near 20 L and decreases rapidly for $d_G \geq 25$ L. The SHG power decreases by a factor of 42 from 6 L to 3 L, faster than the quadratic layer-dependence expected for a layer-independent value of $\chi^{(2)}$, and increases from 3 L to 2 L by a factor of 2.0 ± 1.4 . For 2 L and 1 L, the values of $|\chi^{(2)}|$ are similar within the sample-to-sample variance. We would discuss the reduction of $|\chi^{(2)}|$ for thickness ≤ 6 L in Sec. 5.6.

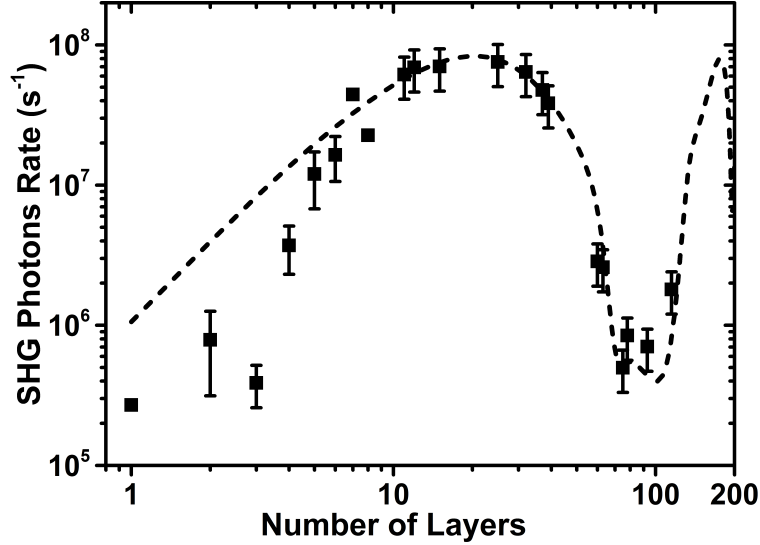


Figure 5.6 **The thickness-dependent SHG for a fundamental wavelength of 785 nm.** The square black symbols and dashed curve respectively are experimental data and fitting based on the model in Fig. 5.4.

5.6 Frequency-dependent SHG

To explore possible changes in the electronic structure of few-layer GaSe and the anomalous thickness dependence of $\chi^{(2)}$ in few-layer samples, we carried out frequency-dependent SHG measurements with SH energies from 1.7 to 2.8 eV for nanoslabs from 2 L to > 100 L. To reduce experimental uncertainties in the absolute determination of the nonlinear susceptibility, we determined the ratio of the SHG power from GaSe to that from a BBO crystal (thickness > 4 mm), since BBO has a flat response over the spectral region in our study. The samples are excited with vertically polarized fundamental field, and the SH radiation is collected with the polarizer before the spectrometer orientated at 45° and 135° to the x axis, at which angles the spectrometer ideally has identical collection efficiency. We first measured the spectrum of SH radiation from the samples and then the BBO crystal, as the supercontinuum light source was stable for several hours. The samples and the BBO crystal are measured under the same experimental conditions, such as the fundamental power, except that there is a sapphire window between the GaSe samples and the objective during measurements but nothing between the BBO crystal and the objective. The sapphire window will cause additional spherical aberration that leads to a larger focal spot on the surface of

the samples and smaller SH power for the same fundamental power than in the case of the BBO crystal. The final SH power ratio between GaSe samples and the BBO crystal is scaled to the same spot size, i.e., the SH power of the samples is scaled by a factor of $f^{0.5}$, where f is the ratio of the area of the focal spot on the GaSe samples to that on the BBO crystal ($f \approx 4.4$ in our case).

The SH fields from the BBO crystal are determined similarly to the case of GaSe, except that the presence of only a single interface greatly simplifies the model, as shown in the inset of Fig. 5.7b. (In fact, there is a dielectric coating on the BBO crystal, the correction of which increases $|\chi^{(2)}|$ by a factor of 3%.) The reflected SHG field from the BBO crystal, E_V is given by

$$E_V = \frac{-4\pi P_B^{(2)}}{(\epsilon_B^{1/2} \cos \theta_B + \cos \theta_V)(\epsilon_B^{1/2} \cos \theta_B + \epsilon_P^{1/2} \cos \theta_P)} \quad (5.5)$$

where $\vec{P}_B = \vec{P}_{B,ff} = \overset{\leftrightarrow}{\chi}^{(2)} : \vec{E}_{B,f}^\omega \vec{E}_{B,f}^\omega$, θ_V is the incident angle of the fundamental field, θ_B and ϵ_B are respectively the refracted angle and dielectric constant of the SH field in the BBO crystal and are related to θ_V by $\sin \theta_V = \epsilon_B^{1/2} \sin \theta_B$, and θ_P is the refracted angle of the inhomogeneous field and is the same as the angle of the fundamental field in the BBO crystal. We show four representative spectra of the frequency-dependent ratio of the SHG power in Fig. 5.7a. We fit the spectra of the SHG power from 1.7 to 2.4 eV with a spectrally constant value of $\chi^{(2)}$ according to the model described in Sec. 5.3. The fittings yield $|\chi^{(2)}| = 102 \pm 17, 66 \pm 11, 7.2 \pm 1.8,$ and 28 ± 6.4 pm/V for samples of 78, 8, 3, and 2 layers, respectively. The mismatch of 78- and 8-L samples at high SH energy might be due to enhancement of $\chi^{(2)}$ by high-energy resonances.

We do not observe any features indicative of excitonic resonances at the band gap in the SHG spectra of Fig. 5.7a. This is in contrast to the case of WSe₂ monolayers, in which SHG has been observed to increase by three orders of magnitude near the two-photon excitonic resonance [175]. The absence of excitonic enhancement in GaSe may be attributed to the weak absorption for light with electric field \vec{E} perpendicular to the crystalline c -axis [182, 110]. We note that previous studies of bulk GaSe revealed only a weak two-photon excitonic resonance in the SHG power after accounting for the frequency-dependent optical absorption [183]. Even a low-temperature study [184] only showed an increase of the SHG power by a factor of 2 at the one-photon excitonic

resonance. This suggests that for wave propagation along the c axis, the SHG response in GaSe is dominated by transitions other than those giving rise to band-edge absorption. This does not rule out the possibility that the reduction in SHG from few-layer GaSe is associated with predicted changes in the highest valence band and lowest conduction band [33, 34, 35]. For example, the primary contributions to the SHG response could come from transitions between one of these bands and higher conduction or lower valence bands. However, further calculations would be needed to understand the origin of the SHG response.

In Fig. 5.7b, we show experimental data and fitting of the layer-dependent ratio of the SHG power from GaSe to the SHG power from BBO at the SHG energies $\hbar\omega_{\text{SHG}} = 2.0$ eV and 2.6 eV. Our model reveals that for both $\hbar\omega_{\text{SHG}} = 2.0$ eV and 2.6 eV, $|\chi^{(2)}| = 80 \pm 18$ pm/V, consistent with the result determined by the absolute measurement at $\hbar\omega_{\text{SHG}} = 3.16$ eV. The similar value of $|\chi^{(2)}|$ at $\hbar\omega_{\text{SHG}}$ from 2.0 eV to 3.16 eV again indicates that any excitonic contribution to the nonlinear optical susceptibility at room temperature is weak.

5.7 Conclusion

We have measured the room-temperature second-harmonic response of GaSe from monolayer to >100 layers for sub-band-gap fundamental photon energies but second-harmonic photon energies from 1.7 to 3.1 eV, i.e., tuning the second-harmonic across the band gap. For crystals of thickness >10 layers, we obtain a value of the second-order susceptibility of $|\chi^{(2)}| = 80 \pm 18$ pm/V for a fundamental photon energy below 1.3 eV, which is close to that reported for the bulk. Deviations from the bulk second-order susceptibility $\chi^{(2)}$ are observed only for thicknesses $\lesssim 7$ layers, at which thicknesses $\chi^{(2)}$ is suppressed. No signatures of two-photon excitonic resonances are observed, which is consistent with the weak excitonic absorption for electric fields polarized perpendicular to the c axis.

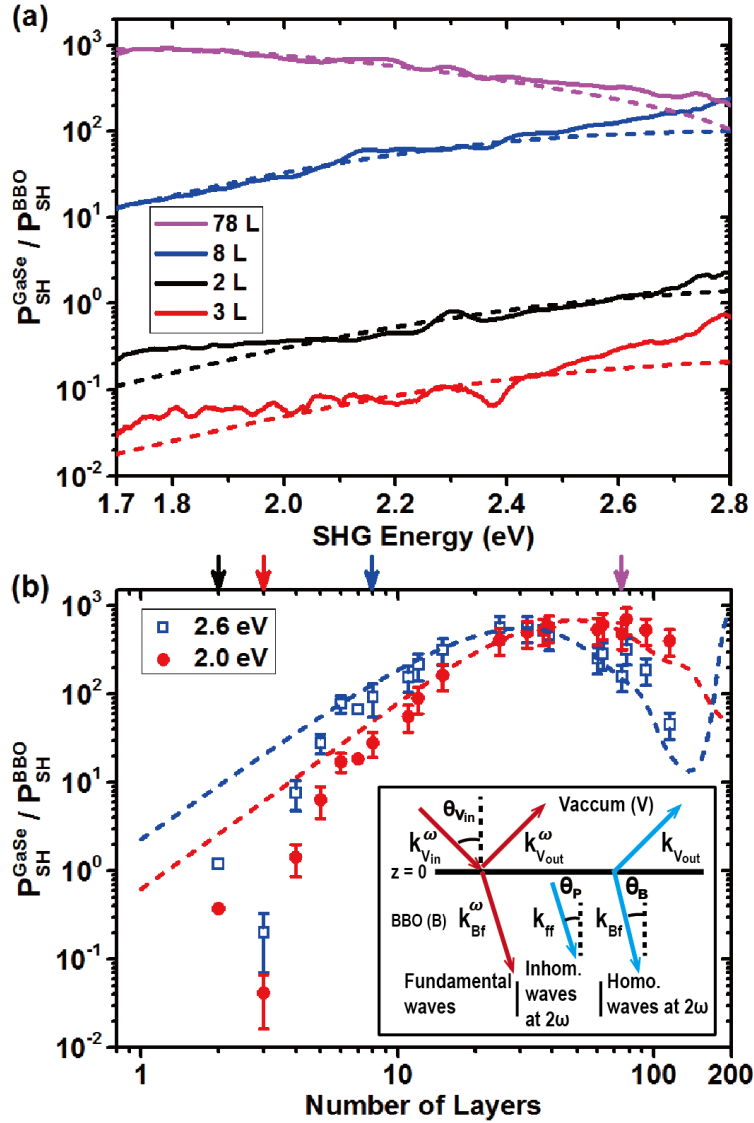


Figure 5.7 **Ratio between the reflected SHG power from GaSe nanoslabs and a thick BBO crystal.** (a) Representative curves of the frequency-dependent ratio of the SHG power from 2 L, 3 L, 8 L, and 78 L GaSe nanoslabs. The dashed curves are fits to the SHG spectrum from 1.7 eV to 2.4 eV according to the model in the text. (b) Layer-dependent ratio of the SHG power at the SHG energies $\hbar\omega_{SHG} = 2.0$ eV (red dots) and 2.6 eV (open blue squares), with uncertainties determined as in Fig. 5.6. The arrows indicate the thickness of samples whose frequency-dependent SHG power are shown in (a). The dashed red and blue curves are fits to the data for thickness ≥ 10 L. By comparing to the well known nonlinear optical coefficient of BBO ($d_{22} = 2.2$ pm/V), the fit reveals $|\chi^{(2)}| = 80 \pm 18$ pm/V for $\hbar\omega_{SHG} = 2.0$ eV and 2.6 eV. The inset in (b) illustrates the fields involved in calculating the reflected SHG from the BBO crystal.

CHAPTER 6

THE OPTICAL STARK EFFECT IN COLLOIDAL CdSe NQDS

6.1 Introduction

Strong confinement in nanocrystal quantum dots (NQDs) has dramatic implications for fundamental physical processes, e.g., spin-carrier interactions [185], and applications. The most invoked and widely analyzed consequence of confinement is the size-dependence of optical transition energies. Equally important is the size-dependent oscillator strength, i.e., the light-matter interaction, of the lowest-energy transitions. Large oscillator strengths imply strong absorption and emission and so determine the performance of NQD-based photovoltaics [186], light-emitting diodes [187], and bio-labels[188]. Despite debates over the appropriateness of the $k \cdot p$ effective-mass approximation (EMA) for calculations of the electronic structure of small NQDs [189, 190, 191, 192], optical transition energies have been well reproduced by the EMA [67, 68, 69, 70, 66, 71, 72]. Meanwhile, one of the landmark achievements of EMA-based calculations of NQD electronic structure was the calculation of the exciton fine structure of CdSe NQDs, the most widely studied NQD system, and identification of the lowest-energy dark states[193, 69]. The EMA also predicts large, nearly size-independent values of the integrated oscillator strength of the lowest-energy excitons[54, 75, 194, 69].

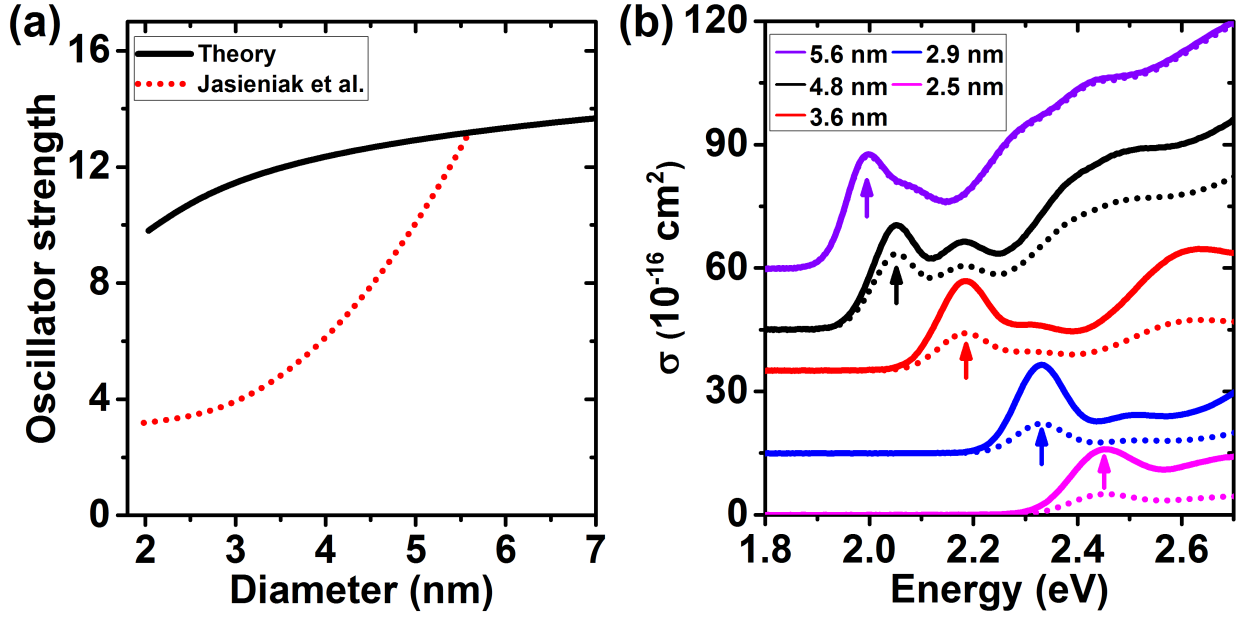


Figure 6.1 **Comparisons between the effective-mass approximation and previously reported results.** (a) Integrated, orientationally averaged oscillator strength of the $1S_{3/2}1S_e$ peak in CdSe NQDs based on the effective-mass approximation (EMA, black curve) and as experimentally measured in Ref. [71] (dotted red curve). The EMA curve is based on a constant value of $(\hbar\omega f)_{1S_{3/2}1S_e}$, which is taken equal to the sum of the orientationally averaged A and B excitons in the bulk ($f = 14.3$, $\hbar\omega = 1.84$ eV) [195]. (b) Ground-state absorption cross section for NQDs of different sizes: Solid curves refer to the EMA, and dashed curves refer to the results of Ref. [71]. The arrows indicate the $1S_{3/2}1S_e$ peak.

As NQD radius decreases below the bulk exciton Bohr radius, a_B^* , the reduced number of unit cells comprising a NQD, and so contributing to the oscillator strength, is compensated by the increased volume of reciprocal-space contributing to the lowest-energy confined excitons (the $1S_{3/2}1S_e$ excitons in CdSe [67]). As a result, and as shown above, the EMA predicts the product of the energy ($\hbar\omega$) and the oscillator strength (f) to be size-independent for the $1S_{3/2}1S_e$ exciton manifold [54, 75, 194, 69]. Despite the aforementioned successes of the EMA, numerous measurements of CdSe NQDs based on challenging analytic estimates [196] of NQD concentrations in solution suggest a strongly size-dependent value of $f_{1S_{3/2}1S_e}$ falling in small NQDs to $\lesssim 1/3$ the bulk exciton value [76, 197, 70, 66, 198, 71, 72]. The divergent values of $f_{1S_{3/2}1S_e}$ determined by experiment and EMA calculations and the corresponding implications for the spectra of the

ground-state absorption cross section are highlighted in Fig. 6.1. Notably, the experimental results have gone unexplained. If valid, these results imply a basic misunderstanding of the electronic structure of strongly confined NQDs and a failure of the EMA, while suggesting that single excitons in small NQDs are much less easily optically generated and manipulated than in larger NQDs or bulk [199].

Here, we use optical Stark metrology to obtain a measure of $f_{1S_{3/2}1S_e}$ that is free of estimates of NQD concentration and only weakly sensitive to the accuracy with which NQD size is known. We show the total oscillator strength of the $1S_{3/2} \rightarrow 1S_e$ transition in CdSe NQDs to be consistent with predictions of the EMA. These large oscillator strengths enable helicity-selective, unsaturated Stark shifts of 17 meV corresponding to pseudo-magnetic fields exceeding 100 T and suggesting new possibilities for coherent optical spin manipulation in NQDs. The results and discussion can also be found in [200].

6.2 Background

6.2.1 A brief discussion of experimental size-dependence studies of $f_{1S_{3/2}1S_e}$

Colloidal NQDs provide a platform to test quantum theory in the strong-quantum-confinement regime. The question of how the oscillator strength evolves as a function of NQD size has been theoretically and experimentally explored since decades ago. Both theories based on EMA with the $k \cdot p$ method [54, 194, 69] and an atomistic direct diagonalization pseudopotential approach [201, 202] have been successful in describing spectral features due to quantized states and calculation of exciton fine structure, and they all have predicted almost size-independent $f_{1S_{3/2}1S_e}$ in the strong confinement regime. Experimental studies of CdS [203] and CdTe [204, 205] NQDs have shown nearly size-independent $f_{1S_{3/2}1S_e}$, consistent with theories. However, despite quantitative discrepancies, $f_{1S_{3/2}1S_e}$ of CdSe NQDs [70, 71, 72, 198, 76], the most studied NQD system, generally shows a linear size-dependence across reports, although there have been other size dependences reported [197, 66].

To understand the inconsistencies with theories, consider how $f_{1S_{3/2}1S_e}$ per NQD is experimentally determined. The typical experimental method is to measure the absorbance spectrum $A(\omega)$ of colloidal NQDs in solution and then measure the concentration of NQDs, C , in the solution. The extinction coefficient per NQD, $\epsilon(\omega)$, can be expressed as $\epsilon(\omega) = A(\omega)/(C \cdot l)$, where l is the optical path length. $f_{1S_{3/2}1S_e}$ can be derived by integrating $\epsilon(\omega)$ over the $1S_{3/2}1S_e$ peak. In this process, determination of C is difficult, which is probably the reason for the discrepancies among different experimental studies and may explain the disagreement with theoretical predictions. One of the methods of measuring the concentration of NQDs is to measure the concentration of Cd^{2+} ions by an atomic absorption spectrum after chemical digestion of NQDs [197, 71]. If the number of Cd^{2+} ions per NQD is known, one then knows the concentration of NQDs. Another method is to measure the total weight of dried NQDs [70, 206]. If the weight per NQD is known, one can determine the concentration of NQDs. However, the determination of the number of Cd^{2+} ions and weight per NQD can be affected by many factors such as the assumption of a given shape and stoichiometry of NQDs and size measurements based on transmission electron microscopy (TEM). For the TEM measurements, people usually take a snapshot of hundreds of NQDs at one time and then do a size analysis, but the boundaries of the NQDs might not be precisely determined.

There are also other methods that do not require measurements of the concentration of NQDs. For example, people have assumed bulk-like absorption at high energy (3.1 to 3.5 eV) [76, 198], i.e., at energies sufficiently high that the absorption coefficient of NQDs at such energies does not depend on the size and is the same as the bulk value. This assumption leads to a linear size-dependence for $f_{1S_{3/2}1S_e}$. It is true that quantum confinement will eventually have no effect on transitions when the transition energy becomes high enough, because then the transitions mainly involve well-localized states. However, whether the energies from 3.1 to 3.5 eV are high enough is questionable, as spectral features due to quantized states still can be observed at such energies [72, 205]. People have also tried to measure the size dependence of the PL radiative lifetime [207, 198], which indicates a size-independent $f_{1S_{3/2}1S_e}$ in CdSe NQDs. However, the PL lifetime also depends on other factors besides radiative recombination, such as the size-dependent fine

structure (see Fig. 1.4 in Sec. 1.4), of which the lowest-lying state is dark, and nonradiative processes like trapping.

6.2.2 Why the optical Stark effect?

Here, I will show that the optical Stark effect (OSE) can be a direct method of determining $f_{1S_{3/2}1S_e}$ with few assumptions and without requiring measurement of the concentration of NQDs. The OSE, illustrated in Fig. 6.2, is a shift of an optical transition due to interaction with a non-resonant optical field that transiently mixes the two states of the transition. The optical Stark shift (OSS) of states i and j , of energies E_i and $E_j > E_i$, connected by a dipole-allowed transition is given by second-order perturbation theory [208] as

$$\delta E_j = -\delta E_i = \frac{1}{4} |\mathcal{E}_{\text{in}}|^2 |\mathbf{e} \cdot \vec{\mu}_{ji}|^2 \left(\frac{1}{\Delta_{ji}^-} + \frac{1}{\Delta_{ji}^+} \right), \quad (6.1)$$

where \mathbf{e} is the unit polarization vector of the electric field, $\vec{\mu}_{ji} \equiv -e\vec{r}_{ji}$ is the electric dipole transition matrix element, e is the magnitude of the electron charge, $\Delta_{ji}^\pm = E_j - E_i \pm E_p$, and $E_p = \hbar\omega_p$ is the energy of the Stark pump. \mathcal{E}_{in} is related to the pump intensity, I_0 , by $|\mathcal{E}_{\text{in}}|^2 = 2|F|^2 I_0 / (\epsilon_0 n_s c)$, where $F = \mathcal{E}_{\text{in}} / \mathcal{E}_{\text{out}}$ is the local field correction factor relating the electric field inside (\mathcal{E}_{in}) and outside (\mathcal{E}_{out}) the NQD, ϵ_0 is the permittivity of free space, n_s is the solvent refractive and c is the vacuum speed of light.

The key difference between the OSS measurements and the absorption-spectra measurements is that the absorbance is an extensive quantity but the OSS is an intensive quantity. Because the OSS is an intrinsically single-exciton process, the concentration does not appear in Eq. 6.1. Since I_0 and Δ_{ji}^\pm are easily measured, the OSS reports directly on $|\mathbf{e} \cdot \vec{\mu}_{ji}|^2$ and consequently on the oscillator strength of the $i \rightarrow j$ transition:

$$f_{ji} = \frac{2m_0\omega_{ji}}{\hbar e^2} \langle |\mathbf{e} \cdot \vec{\mu}_{ji}|^2 \rangle_\Omega = \frac{2}{m_0\hbar\omega_{ji}} \langle |\mathbf{e} \cdot \vec{p}_{ji}|^2 \rangle_\Omega, \quad (6.2)$$

where \vec{p} is the momentum operator and the angled brackets indicate an average over all orientations of the system (hereafter we drop the subscript Ω). Since in the EMA \vec{p}_{ji} is energy-independent for

interband transitions, $(\hbar\omega f)_{1S_{3/2}1S_e}$ is predicted to be constant [54, 69].

In practice, the light-matter interaction in NQDs is often described in terms of the absorption cross section. $f_{1S_{3/2}1S_e}$ is directly related to the energy-integrated absorption cross section of the $1S_{3/2}1S_e$ peak [209]:

$$\bar{\sigma}_{1S_{3/2}1S_e} = \frac{\pi e^2 \hbar}{2 \epsilon_0 n_s m_0 c} \left| F \left(\hbar\omega_{1S_e, 1S_{3/2}} \right) \right|^2 f_{1S_{3/2}1S_e}, \quad (6.3)$$

where m_0 is the electron mass in vacuum.

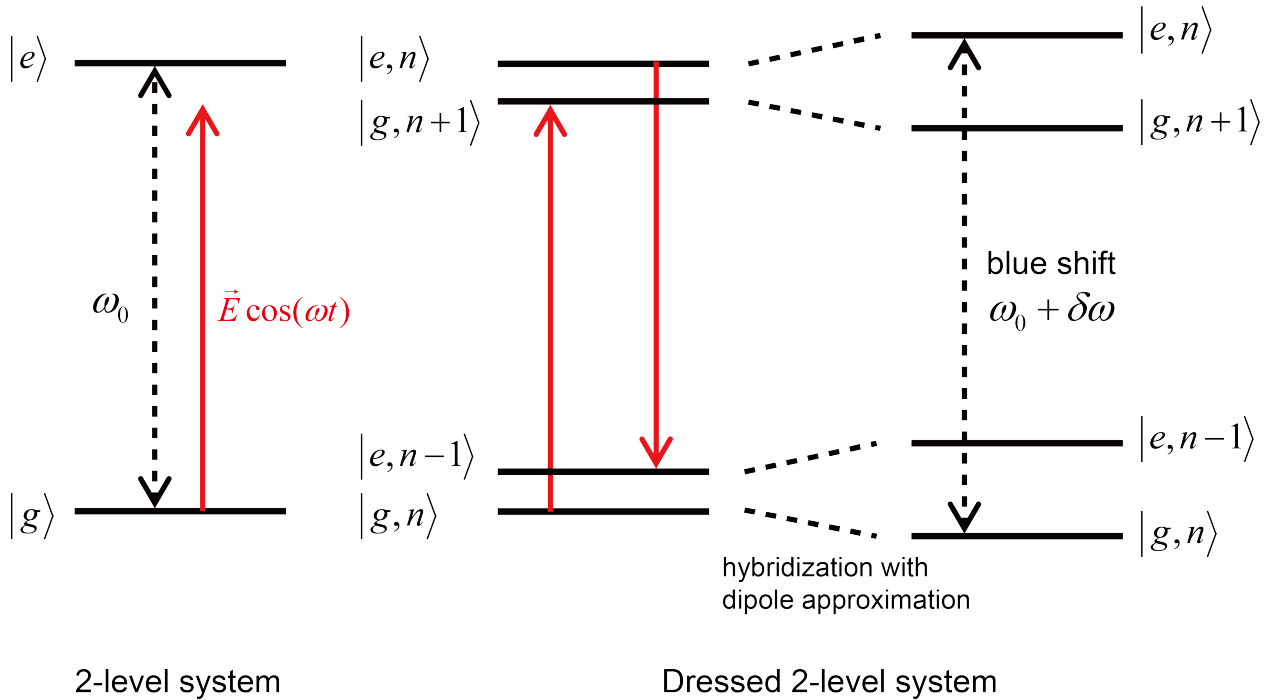


Figure 6.2 **Illustration of the optical Stark effect of a two-level system.** The two-level system consists of $|g\rangle$ and $|e\rangle$ with angular frequency difference of ω_0 due to a red-detuned Stark pump with angular frequency of ω . The left panel describe only the two-level system, a material state. The right two panels describe a photon-dressed two-level system, where the material state is coupled to the electric field. n indicates the number of photons dressed by the two-level system. In the dressed picture, hybridization with electric-dipole interaction leads to an anti-crossing, which results in a blue shift $\delta\omega$ of the transition from $|g, n\rangle$ to $|e, n\rangle$.

6.3 Experimental methods

Sample Preparation: Optical experiments were performed on CdSe NQDs with the wurtzite crystal structure and diameters $d = 2.5\text{--}6.7$ nm (cf. $2a_{\text{B}}^* = 11.2$ nm), which were synthesized by Rémi's group with heating-up method by Prof. Beaulac's group [210] or hot-injection method from NN-Labs [211]. NQD diameters were determined from the energy of the $1S_{3/2}1S_e$ absorption peak using the empirical sizing curve of Ref. [71]. NQDs were dissolved in toluene or, in the case of 6.7 nm dots, in CCl_4 and loaded into fused silica cuvettes with 1-mm solution path length. The reason for using CCl_4 is that the stimulated Raman signal (0.379 eV) of toluene spectrally overlaps the OSE response of 6.7 nm dots.

Optical measurements: The OSE and carrier dynamics were measured by the differential absorption (DA) setup described in Sec. 2.1. For the OSE, we pumped samples with the ~ 100 -fs, 1.55-eV output of a 1-kHz Ti:sapphire laser or the doubled output of a home-made optical parametric amplifier pumped by the laser. We generated real excited populations with the second harmonic of the laser fundamental. The probe was a supercontinuum produced by focusing ~ 1 μJ of the laser output onto a c -cut sapphire crystal and compressed for minimum dispersion around 2.2 eV with a pair of fused-silica prisms. Pump and probe beam diameters at the sample were respectively ~ 1 mm and ~ 0.1 mm. The angle between the pump and probe was 7.5° . We measured the transmitted probe with 5 meV resolution using a CCD spectrometer synchronized to a mechanical chopper in the pump path. The pump fluence was determined by measurement of the pump power transmitted by a pinhole assuming a spatially uniform intensity over the pinhole. The peak intensity (I_0) was determined by a temporal Gaussian fit of $-\Delta\alpha(t)L$ at the lowest-energy DA peak (see Fig. 6.3). The linear (circular) polarization of pump and probe were controlled by half-wave (quarter-wave) plates. The pump power was modulated by a set of neutral density filters. The solvent response was accounted for by subtracting the DA signal from the neat solvent under the same conditions as the NQDs.

Characterization of pulse temporal duration: For determining the oscillator strength via the OSE method, it is important to determine the pulse temporal duration to get a precise peak intensity. As the OSE is a transient phenomenon which only exists in the presence of the pump field, we can use the OSE itself to measure the temporal convolution of the pump and probe, as shown in Fig. 6.3. The peak intensity is given by $I_{peak} = \frac{2\sqrt{\ln(2)}J}{\sqrt{\pi}FWHM}$ ($GW \cdot cm^{-2} \cdot eV^{-1}$), where J and FWHM respectively are the energy fluence per pulse and the full-width-half-maximum by a Gaussian fitting. I choose the maximum experimental $|\Delta\alpha L|$ as the OSE response at the peak intensity. To avoid missing the real peak intensity, there are at least four data points within the FWHM, the highest of which is $\sim 6\%$ lower than the maximum of the fitting. Without fitting, there will generally be a systematic underestimate. The reason that I didn't use maximum of the fitting is that the fitting does not necessarily reveal the real peak of the OSE response, i.e., the temporal convoluted profile of pump and probe might not be exact Gaussian-like. (I used the maximum experimental OSS as the peak value.)

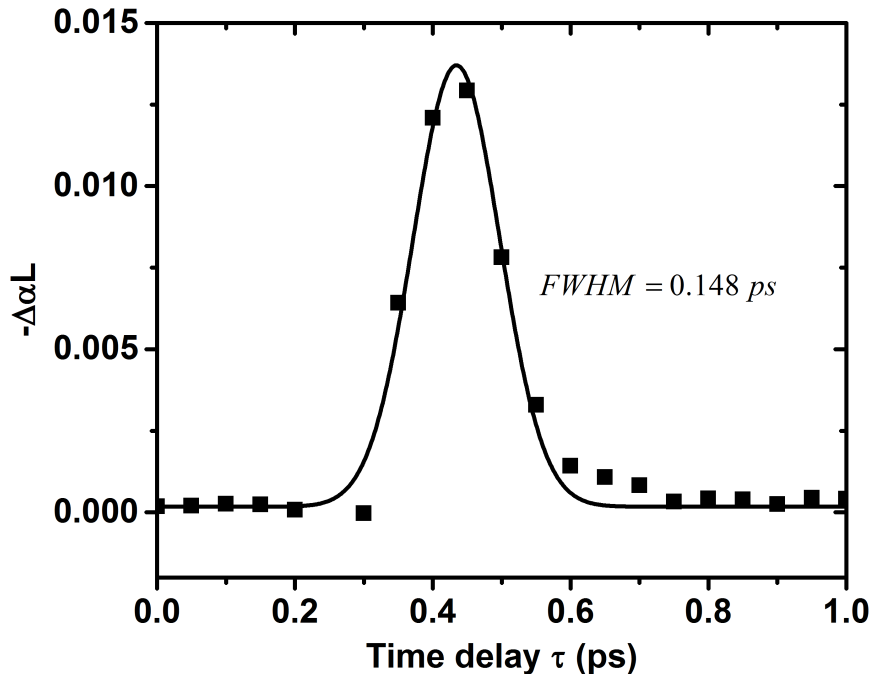


Figure 6.3 **Differential absorption dynamics of the OSE of 3.6 nm CdSe NQDs with 800 nm excitation.** The symbols are experimental data with temporal step size of 50 fs. The solid curve is a Gaussian fit, revealing a temporal full-width-half-maximum (FWHM) of 0.148 ps.

6.4 The evidence of the optical Stark effect

Fig. 6.4a shows a typical CdSe-NQD differential absorption (DA) spectrum, $-\Delta\alpha(\hbar\omega, t)L$, where α and L are respectively the absorption coefficient and length of the NQD solution. In Fig. 6.4b, we compare the DA spectrum at the time delay when the DA has the maximum response (around $t = 0$ ps) to the difference $-\Delta\alpha_{\text{fit}}L \equiv \left[\alpha_0(E) - \alpha_0(E + \delta E_{1\text{Se}, 1\text{S}_{3/2}}^{\text{obs}}) \right] L$, where the observed OSS, $\delta E_{1\text{Se}, 1\text{S}_{3/2}}^{\text{obs}}$, is a fitting parameter used to match $\Delta\alpha_{\text{fit}}L$ to the amplitude of the measured $\Delta\alpha(E, t = 0)L$ at the lowest-energy DA peak (see App. D.1 for discussion of the relationship between the observed OSS of the $1\text{S}_{3/2}1\text{S}_e$ peak and the actual OSS of the individual transitions within the spectral peak). The local extrema of $\Delta\alpha(E, t = 0)L$ and $\Delta\alpha_{\text{fit}}L$ occur at the same frequencies, which indicates that the nonlinear features are due to the OSE. The magnitudes are different at higher energy as a consequence of different oscillator strengths and detuning factors at higher energy. However, we are only interested in the lowest-energy exciton.

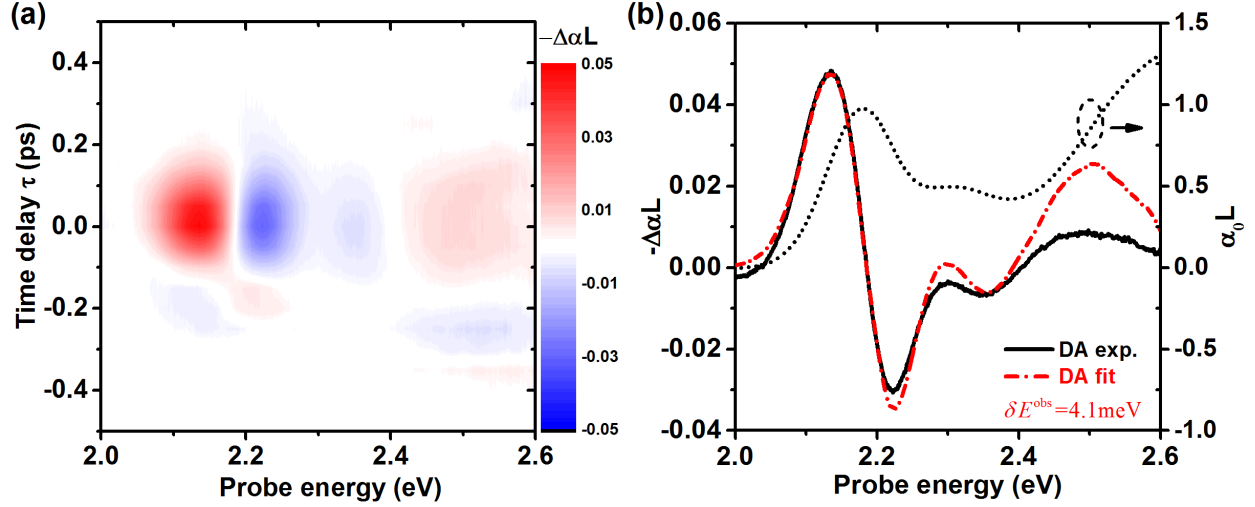


Figure 6.4 **Optical Stark effect for CdSe NQDs and co-linearly polarized Stark and probe fields.** (a) Experimental differential absorption (DA) spectrum, $-\Delta\alpha(\hbar\omega, t)L = -[\alpha_{\text{pump}}(\hbar\omega, t) - \alpha_0(\hbar\omega)]L$, for 3.6 nm NQDs, where $\alpha_{\text{pump}}(\hbar\omega, t)$ and $\alpha_0(\hbar\omega)$ are the absorption coefficients of the NQD solution in the presence and absence, respectively, of the Stark pump and L is the sample length. The Stark pump is at $E_p = 1.55$ eV, corresponding to a -0.63 eV detuning from the $1S_{3/2}1S_e$ absorption peak, with intensity $I_0 = 10.7 \pm 1.1 \text{ GW cm}^{-2}$. (b) $-\Delta\alpha(E, t = 0)L$ (solid curve), $\alpha_0 L$ (dotted curve), and $-\Delta\alpha_{\text{fit}}(E, 0)L \equiv \left[\alpha_0(E) - \alpha_0\left(E + \delta E_{1S_{3/2}1S_e}^{\text{obs}}\right) \right] L$ (dashed-dotted curve) with $\delta E_{1S_e, 1S_{3/2}}^{\text{obs}} = 4.1 \text{ meV}$.

6.5 Excitation-energy- and size-dependence of the optical Stark effect

The excitation- and size-dependence of the OSS for CdSe NQDs are shown in Fig. 6.5a for detuning $-\Delta^- \equiv -\Delta_{1S_{3/2}1S_e}^- = -0.20$ to -0.29 eV. The observed linear dependence of $\delta E_{1S_{3/2}1S_e}^{\text{obs}}$ on $I_0(1/\Delta^- + 1/\Delta^+)$ (the slope of the OSS data) varies with size by only about $\pm 20\%$, immediately suggesting a similarly limited size-dependence of $f_{1S_{3/2}1S_e}$ in contrast to earlier results shown in Fig. 6.1. Importantly, at equal values of $I_0(1/\Delta^+ + 1/\Delta^-)$ the OSS shown for 3.6 nm CdSe NQDs with a -0.63 eV (large) detuning yields a significantly different slope than at -0.28 eV (small) detuning, which is at odds with Eq. 6.1. This is evidence that the OSS of the $1S_{3/2}1S_e$ peak is not determined solely by the interaction of light with the $1S_{3/2} \rightarrow 1S_e$ transition. To correctly determine $f_{1S_{3/2}1S_e}$, we must account for the contributions of other transitions to the OSS of the

$1S_{3/2}1S_e$ peak.

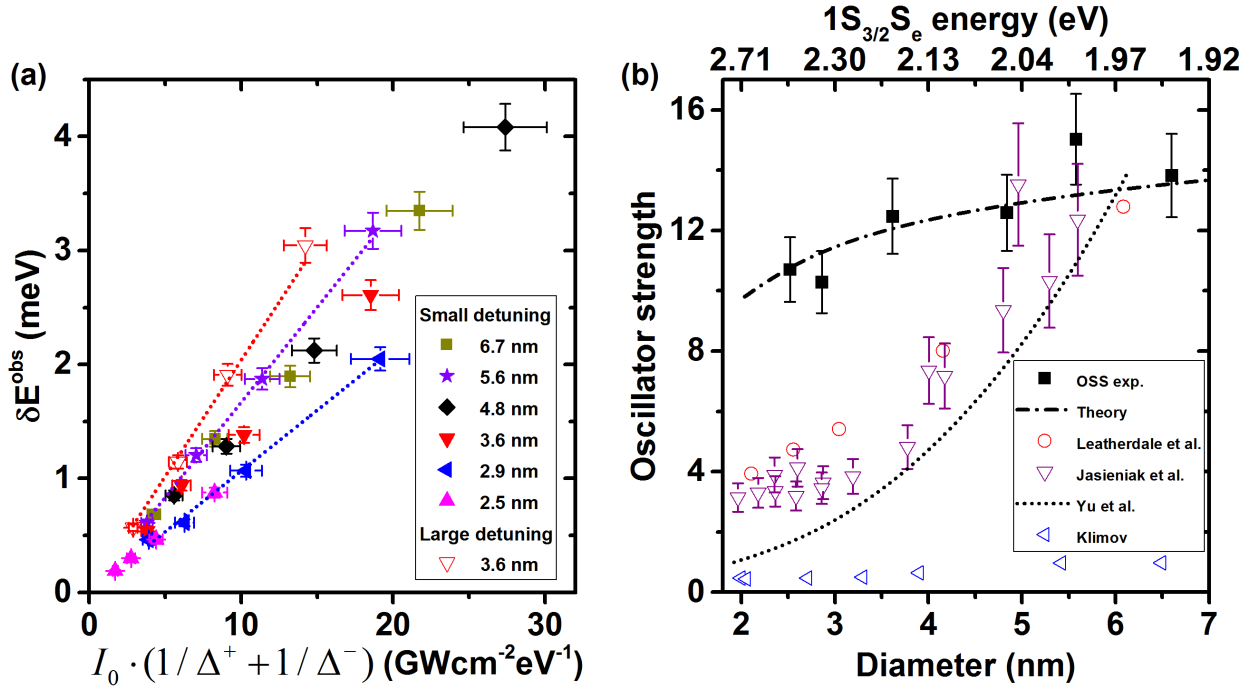


Figure 6.5 **Size-dependent optical Stark shift and oscillator strengths.** (a) OSS for NQDs excited at 0.20–0.29 eV (filled symbols, see Table D.1 in App. D.2 for detunings) or 0.63 eV (open triangles) below the $1S_{3/2}1S_e$ peak. The OSS shows a linear dependence on $I_0 \cdot (1/\Delta^+ + 1/\Delta^-)$, where I_0 is the pump intensity, $\Delta^\pm = E_{1S} \pm E_p$, and E_{1S} and E_p are respectively the energy of the $1S_{3/2}1S_e$ peak and the Stark pump field. (b) Energy-integrated oscillator strength per NQD of the $1S_{3/2}1S_e$ peak as determined here (filled squares) and previous approaches (open symbols and dotted line), which could be found in the Ref. [70, 71, 66, 76]. The dash-dotted curve is the prediction of the effective-mass approximation for $(\hbar\omega f)_{\text{bulk}} = 26.3$ eV, as shown in Fig. 6.1a.

While an exact accounting of the OSS must address the excitonic (and biexcitonic) origins of the OSS[212], for Stark-pump detunings large compared to the fine structure splittings and biexciton binding, the OSS is accurately calculated in a single-particle picture[213]. For the $1S_{3/2}1S_e$ peak, this can be shown explicitly using detailed theories of single- and biexciton-fine-structure states [69, 214] (see App. D.4). Nonetheless, we must still account for the OSS associated with all transitions involving the $1S_{3/2}$ or $1S_e$ states and for the orientational distribution of NQDs (see App. D.2). For example, the oscillator strength of the $1S_e \rightarrow 1P_e$ transition is expected to be of the same order of magnitude as the $1S_{3/2} \rightarrow 1S_e$ transition[215] and so will contribute to the shift of

the $1S_e$ state and, hence, to the observed OSS of the $1S_{3/2}1S_e$ peak to the extent that the detuning from the $1S_e \rightarrow 1P_e$ is not too large. The observed OSS is then determined by a weighted (with respect to the matrix element squared) average of the shift of each of the transitions constituting the $1S_{3/2}1S_e$ peak:

$$\delta E_{1S_e, 1S_{3/2}}^{\text{obs}} = \frac{\left\langle \sum_{i, \beta, M} \left(\delta E_{1S_e \beta}^i - \delta E_{1S_{3/2} M}^i \right) \left| \langle 1S_e \beta | \mathbf{e} \cdot \hat{\mathbf{r}} | 1S_{3/2} M \rangle_v \right|^2 \right\rangle}{\left\langle \sum_{\beta, M} \left| \langle 1S_e \beta | \mathbf{e} \cdot \hat{\mathbf{r}} | 1S_{3/2} M \rangle_v \right|^2 \right\rangle}, \quad (6.4)$$

where δE_j^i indicates the OSS of level j due to the $i \rightarrow j$ transition. To highlight the degree to which the OSS of the $1S_{3/2}1S_e$ peak is due to the transitions $1S_{3/2} \rightarrow 1S_e$ or other transitions involving the $1S_{3/2}$ or $1S_e$ states, we can formally write Eq. 6.4 as in Eq. 6.1 via a NQD-diameter- and pump-energy-dependent factor $\gamma = \gamma(d, E_p)$:

$$\delta E_{1S_e, 1S_{3/2}}^{\text{obs}} = \gamma(d, E_p) \frac{|F|^2}{\epsilon_0 n_{sc}} I_0 \left(\frac{1}{\Delta^+} + \frac{1}{\Delta^-} \right) \sum_{\beta, M} \left\langle \left| \mathbf{e} \cdot \vec{\mu}_{1S_e \beta, 1S_{3/2} M} \right|^2 \right\rangle, \quad (6.5)$$

where β (M) is the projection of the electron (hole) angular momentum along the NQD c axis. $f_{1S_{3/2}1S_e}$ can then be related to the observed OSS by

$$\begin{aligned} f_{1S_{3/2}1S_e} &= \frac{2m_0 \omega_{1S_e, 1S_{3/2}}}{\hbar e^2} \sum_{\beta, M} \left\langle \left| \mathbf{e} \cdot \vec{\mu}_{1S_e \beta, 1S_{3/2} M} \right|^2 \right\rangle \\ &= \frac{2\epsilon_0 n_s c m_0 \omega_{1S_e, 1S_{3/2}}}{\gamma(d, E_p) \hbar e^2 |F|^2} \frac{\delta E_{1S_e, 1S_{3/2}}^{\text{obs}}}{I_0 \left(\frac{1}{\Delta^-} + \frac{1}{\Delta^+} \right)}. \end{aligned} \quad (6.6)$$

The key computational parameter in Eqs. 6.5 and 6.6 is $\gamma(d, E_p)$. As shown in Eq. D.7 of App. D.2, accounting solely for interactions between the pump and the $1S_e \rightarrow 1S_{3/2}$ transitions, $\gamma(d, E_p)$ is exactly $2/5$ in a single-particle picture, while variations due to excitonic effects are $\lesssim 3\%$ (see Fig. D.3 in App. D.4) when pump detunings are large compared to the exciton fine-structure splittings and biexciton binding. When including other transitions to or from the $1S_e$ or $1S_{3/2}$ states, for detunings of -0.20 to -0.29 eV and $d = 2.5$ to 6.7 nm, the EMA yields $\gamma(d, E_p) = 0.60$ – 0.66 (details in Table D.1 in App. D.2).

The calculated $\gamma(d, E_p)$ and measured $\delta E_{1S_e, 1S_{3/2}}^{\text{obs}}$ yield the $1S_{3/2}1S_e$ oscillator strengths shown in Fig. 6.5b, where we also show previous estimates of $f_{1S_{3/2}1S_e}$. Most importantly, the values of $f_{1S_{3/2}1S_e}$ measured here closely match theory: the energy-integrated oscillator strength of the $1S_{3/2}1S_e$ peak in CdSe depends only weakly on size. Although $\gamma(d, E_p)$ is markedly different at $E_p = 1.55$ eV (detunings of -0.4 to -0.9 eV) than at smaller detunings, the resulting $f_{1S_{3/2}1S_e}$ are the same as in Fig. 6.5b (see Fig. D.1 in App. D.2); this consistency confirms the validity of the approach. $f_{1S_{3/2}1S_e}$ drops from ~ 14 in the largest dots to ~ 10 in the smallest, while $(\hbar\omega f)_{1S_{3/2}1S_e} = 27 \pm 2$ eV, at least three times larger than previous estimates for the smallest NQDs [76, 197, 70, 66, 198, 71, 72]. For comparison, the orientationally averaged sum of A and B exciton oscillator strengths per CdSe unit cell in the bulk is $f_{\text{unit}} \sim 2.2 \times 10^{-3}$ [195], which yields a combined oscillator strength of $f_X = f_{\text{unit}} V_X / V_{\text{unit}} \sim 14$. The measured OSS for CdTe NQDs (see Fig. D.1 in App. D.2) is the same as for CdSe NQDs of similar size and detuning, as expected given the similar electronic structure of both systems [216]. Notably, the values of $f_{1S_{3/2}1S_e}$ found here for CdSe NQDs are also similar to those reported for CdTe NQDs [205] as expected given the similar electronic parameters (gap and effective masses) of bulk CdSe and CdTe.

6.6 Saturated differential absorption measurements

As a further consistency check on $f_{1S_{3/2}1S_e}$, we measure $\sigma(3.1 \text{ eV})$, the absorption cross section per dot at 3.1 eV, by DA saturation of the $1S_{3/2}1S_e$ transition under 3.1 eV excitation [76].

In Fig. 6.6, we show a pair of representative DA dynamics traces for 3.6 nm CdSe NQDs pumped at 3.1 eV (i.e., > 0.6 eV above the $1S_{3/2}1S_e$ absorption peak) and probed at the $1S_{3/2}1S_e$ transition. At low intensity, the samples are in the single-exciton regime for the entire delay range. At high intensity, the samples experience Auger recombination of multi-exciton states before relaxing into the single-exciton regime at $t > 200$ ps. When normalized at long delays to account for the different signal levels, we see that the dynamics of strongly excited samples after Auger recombination are the same as the dynamics of single-excitons as reflected under low-fluence excitation.

In particular, the amplitude of the signal at long delays should depend only on the probability that at least one pump photon was absorbed and the bleach induced by the single electron or exciton that remains after Auger recombination.

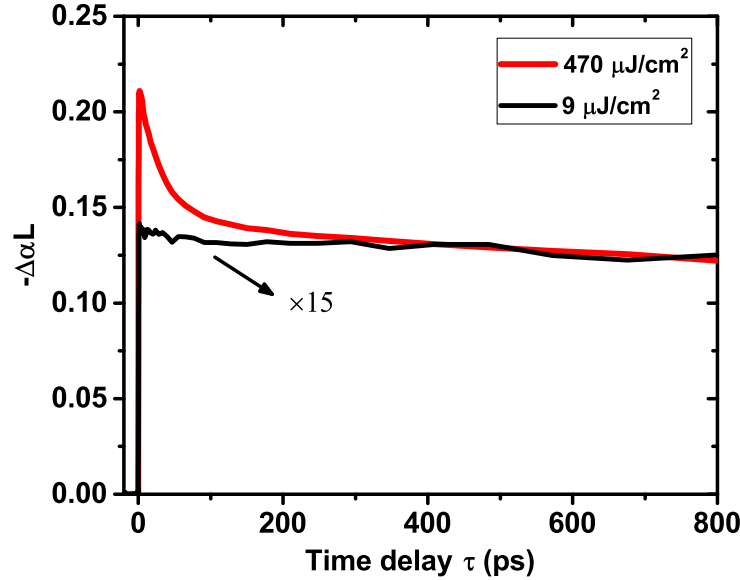


Figure 6.6 **DA dynamics of the $1S_{3/2}1S_e$ peak of 3.6 nm CdSe NQDs.** The samples are pumped at 3.1 eV. The red and black solid curves are the DA dynamics under fluences of 470 and 9 $\mu\text{J}/\text{cm}^2$ per pulse, respectively. The low-fluence data are scaled to highlight the absence of multi-exciton Auger recombination and to show the common dynamics at long delays for both low- and high-fluence excitation.

DA saturation curves of the CdSe $1S_{3/2}1S_e$ peak at $t = 0.8$ ns are shown in Fig. 6.7. No matter how many excitons are initially excited, no more than one exciton remains in each NQD by $\tau = 800$ ps. Therefore, $\sigma(3.1 \text{ eV})$ can be determined by fitting to the Poisson probability of absorption of at least one pump photon per dot: $\frac{-\Delta\alpha}{\alpha_0} = A[1 - P_0(\sigma\Phi)] = A[1 - \exp(-\sigma\Phi)]$, where $P_0(\sigma\Phi)$ is the probability of an NQD absorbing zero photons, Φ is the pump fluence, and the fitting parameters σ and A are the absorption cross section per dot at 3.1 eV and the saturated DA signal, respectively. Ideally, if we neglect the DA response of holes and there is only radiative recombination, we should expect a saturation value of around 0.5, as the radiative recombination usually takes about ~ 20 ns, much longer than the time delay we chose. However, we can see that samples are saturated at different values (A) below 0.5. This might be due to nonradiative

processes, such as trapping, which is different by samples and usually has a time constant shorter than 1 ns.

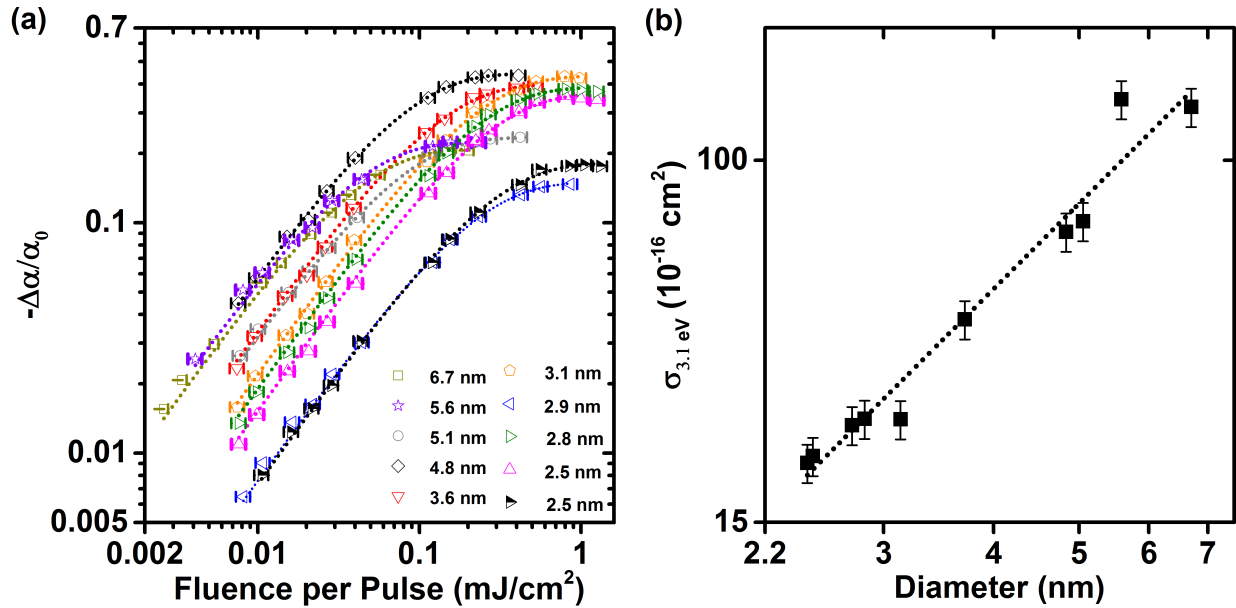


Figure 6.7 **Saturation measurements of the absorption cross section at 3.1 eV.** (a) The fluence-dependence of $-\Delta\alpha/\alpha_0$ at the $1S_{3/2}1S_e$ peak measured at $\tau = 800$ ps for samples with diameter from 2.5 nm to 6.7 nm pumped at 3.1 eV. The dotted curves are fits with the function $-\Delta\alpha/\alpha_0 = A \{1 - \exp[-\sigma(3.1 \text{ eV}) \Phi]\}$ of the absorption cross section per NQD at 3.1 eV, $\sigma(3.1 \text{ eV})$, as a function of the fluence, Φ , at 3.1 eV. (b) The size-dependence of the fitted absorption cross section (solid black squares) at 3.1 eV. The dotted curve is a power-law fit ($\sigma(3.1 \text{ eV}) \propto d^n$) with $n = 2.0 \pm 0.2$.

As shown in Fig. 6.8, the absorption cross section at the peak of the $1S_{3/2}1S_e$ absorption feature determined from the OSS is in close agreement with the absorption cross section determined by DA saturation, again supporting the accuracy of our approach. A power-law fit of the diameter-dependence of $\sigma(3.1 \text{ eV})$ in the inset of Fig. 6.7(b) reveals a $d^{2.0 \pm 0.2}$ dependence. By comparing UV/vis spectra at 3.1 and 3.5 eV, we find that the same quadratic dependence holds at 3.5 eV. This observation is in contrast to earlier assumptions[76, 198] and reports[70, 71] of a d^3 size-dependence, as would be expected when confinement is irrelevant. However, Hens and collaborators have shown that for CdSe and CdTe the absorption spectra are influenced by confinement even at 3.5 eV[72, 205], as well as other studies [70, 68], which makes assumptions of a d^3 dependence

of σ (3.5 eV) questionable. Our observation can be qualitatively understood as a result of quantum confinement: as the NQD diameter decreases, the energy spacing between different transitions increases, leading to a d^{-2} -dependent density of transitions in the high-energy regime. Notably, the ratio of σ (3.1 eV) to $f_{1S_{3/2}1S_e}$ measured here shows a quadratic size-dependence, consistent with previous studies showing a d^2 dependence of the ratio of the high-energy absorption cross section to $f_{1S_{3/2}1S_e}$ [71, 76, 198, 70].

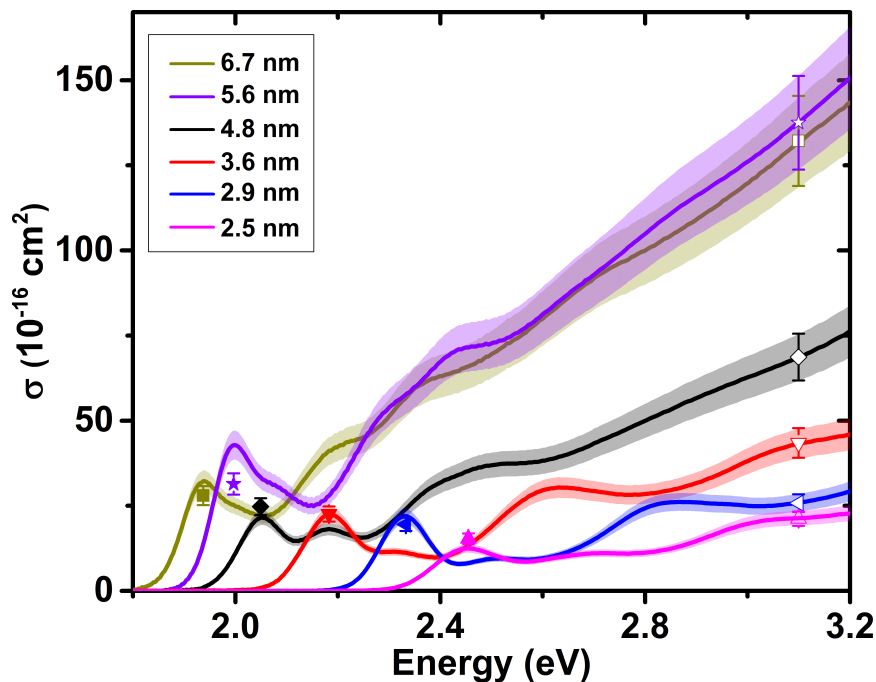


Figure 6.8 **Ground-state absorption cross section (solid curves) for NQDs of different diameter.** The spectra are measured by UV/vis absorption and scaled to the absorption cross section at 3.1 eV as determined by DA saturation measurements (open symbols). The broad bands represent the uncertainty in the overall magnitude of the absorption cross section based on the uncertainty in the DA saturation measurement. Solid points are the expected magnitude of the $1S_{3/2}1S_e$ peak based on the oscillator strengths measured by the OSE.

The discrepancies, reflected in Fig. 6.5b, with earlier experimental reports of $\sigma_{1S_{3/2}1S_e}$ and $f_{1S_{3/2}1S_e}$ for CdSe NQDs may be partly explained by the sensitive dependence of prior analytic approaches on accurate determination of NQD concentrations, which typically rely on assumptions about, e.g., shape, stoichiometry, distribution of stoichiometric excess, and reaction yield and are extremely sensitive to the accuracy of measurements of NQD diameter [196]. For example, if

the radii of small NQDs were underestimated by one unit cell, correction would shift the results of Refs. [70] and [71] (shown in Fig. 6.5b) into agreement with the present results. Although such a large measurement error seems unlikely, this example highlights how sensitive the analytic approach is to the underlying measurements and assumptions. The light-matter interaction has also been addressed by PL lifetime measurements in CdTe and CdSe [207, 198, 196], but nonradiative decay processes and size-dependent fine structure make it difficult to extract the intrinsic $f_{1S_{3/2}1S_e}$ from CdSe by PL lifetime measurements. In contrast to traditional analytic approaches, the oscillator strength determined by the OSS at small detunings does not require knowledge of the NQD concentration and, according to the EMA, is relatively insensitive to experimental estimates of NQD size: the OSS of the $1S_{3/2}1S_e$ peak is dominated by the $1S_{3/2} \rightarrow 1S_e$ transition, so that $\gamma(d, E_p)$ in Eq. 6.5 is calculated to vary across the entire size range studied here by only about 10% for the small-detuning data of Fig. 6.5. Likewise, for Stark pump detunings that are large compared to the unresolved features of the exciton fine structure, the observed OSS is only weakly sensitive to the size-dependent exciton fine structure.

6.7 Helicity-selective optical Stark effect in colloidal CdSe NQDs

The oscillator strength determines the ease of coherent optical manipulation of carriers and spins. Hence, large oscillator strengths underpin proposals for quantum information processing in self-assembled quantum dots[217, 218, 219]. Our measured oscillator strengths suggest the potential for a large helicity-selective OSS. Fig. 6.9a shows the OSS of 3.6 nm NQDs for a 1.904 eV Stark field (-0.28 eV detuning) and co- and counter-circular polarization. As shown in Fig. 6.9b, the difference in the OSS for opposite helicities increases linearly with pump fluence and reaches 9 meV. This corresponds to a pseudo-magnetic field $B_{\text{eff}} = (\delta E^+ - \delta E^-) / (\mu_B g_{\text{eff}}) = 110$ T, where $\delta E^{+(-)}$ is the OSS under co(counter)-circularly polarized Stark and probe fields, μ_B is the Bohr magneton, and $g_{\text{eff}} = 1.4$ [220]. For a pump pulse of length $\tau = 100$ fs, this corresponds to a tipping angle $\theta \approx (\delta E^+ - \delta E^-) \tau / \hbar = 1.4$, or nearly $\pi/2$, similar to that observed in metal-

semiconductor colloidal hetero-nanostructures[199]. Notably, at the highest fluences in Fig. 6.9b the OSS reaches 17 meV while still in the linear regime; no saturation is observed. Measurement of larger shifts was limited by contributions to the DA signal from carriers generated by two-photon absorption. Previous measurements of the OSE in NQDs grown in glass matrices[221, 222] or as hybrid metal-semiconductor heterostructures[199] saw saturation of the OSS at shifts of 1 – 15 meV. The larger unsaturated OSS observed here may be a consequence of larger detunings and correspondingly reduced generation of real populations of screening carriers than in earlier studies or of reduced two-photon absorption in the substantially smaller NQDs studied here than in Refs. [221] and [199]. Larger tipping angles may be attainable by tuning the pump to minimize the ratio of two-photon absorption to the OSS and allow greater Stark pump intensities.

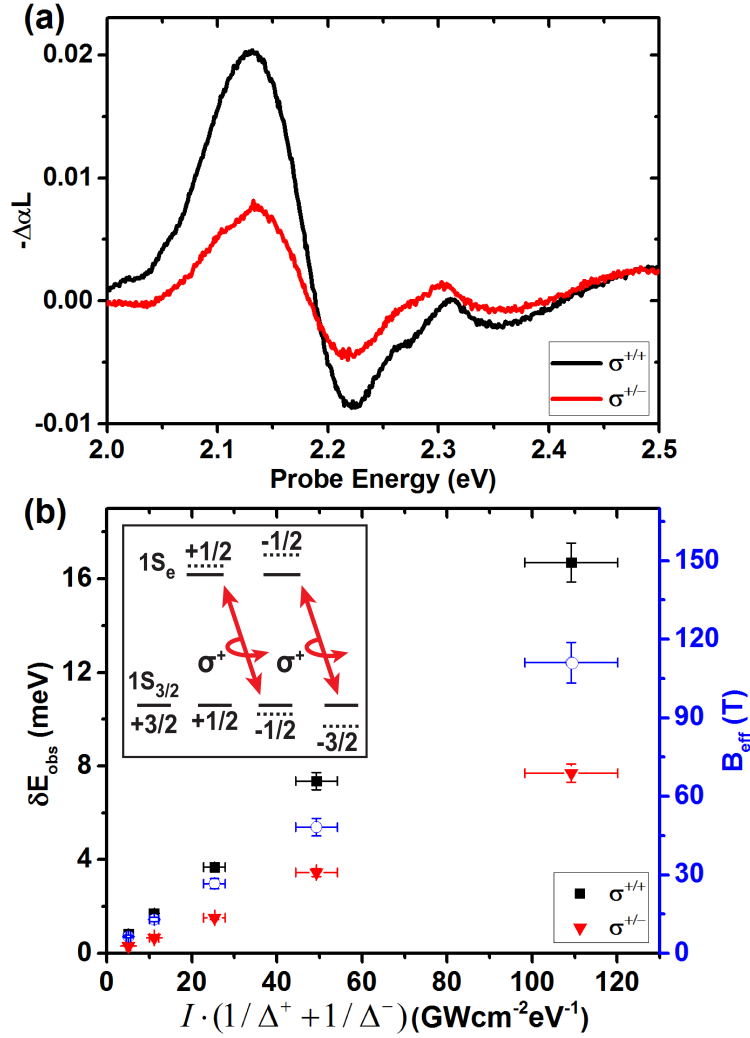


Figure 6.9 **The OSE for circularly polarized excitation.** (a) $-\Delta\alpha L$ spectra for 3.6 nm CdSe NQDs at $\tau = 0$ ps for co- ($\sigma^{+/+}$) and counter-circularly ($\sigma^{+/-}$) polarized Stark field and probe with $E_p = 1.904$ eV and $I_0 = 2.8 \pm 0.3$ GW/cm^2 . (b) The OSS at $\tau = 0$ ps for co- (black squares) and counter-circularly (red triangles) polarized pump and probe are shown as a function of $I_0(1/\Delta^- + 1/\Delta^+)$. The corresponding pseudo-magnetic field, B_{eff} is shown by empty blue circles. The inset is a schematic diagram of the OSS of the $1S_{3/2}$ and $1S_e$ states for right circularly polarized pump.

6.8 Conclusion

The long-standing puzzle over the size-dependence of the $1S_{3/2}1S_e$ oscillator strength in CdSe NQDs highlights the challenges of determining fundamental electronic properties of even the nominally best understood NQD materials. The optical Stark effect offers a general approach for mea-

suring the oscillator strengths in a wider variety of strongly confined systems, such as heterostructured and wide-band-gap NQDs, than is readily achieved by traditional analytical approaches. In CdSe NQDs, the optical Stark effect reveals that, despite long-standing experimental reports to the contrary, the EMA correctly accounts for the oscillator strength of the lowest-energy exciton. At the same time, the demonstrated generation of large optical Stark shifts in the absence of coupling to plasmonic resonances[199] allows for expanded possibilities for coherent manipulation of excitons in NQDs.

CHAPTER 7

SUMMARY

For the spin studies in bulk GaSe (Chap. 3,4), we have demonstrated generation of a high degree (~ 0.9) of optical spin polarization under non-resonant excitation and a long spin memory ($\tau \geq 500$ ps) as revealed by time- and polarization-resolved photoluminescence, which are attributed to the orbital non-degeneracy of conduction and valence bands. We have also observed highly linearly polarized luminescence from edges tens of micrometers away from the optically excited spot with polarization orientation pointing to the spot, which is attributed to emission from singlet excitons. By studying the dynamics of edge and focal emission, we directly reveal the spin-flip-assisted transition from triplet to singlet excitons. The spin-relaxation mechanism is still unknown, which might require temperature-dependent studies of spin dynamics. Our study demonstrates the importance of orbital non-degeneracy in optically generating high spin polarization and maintaining a long spin-polarization time and suggests a possible way of revealing transitions between states with anisotropic optical properties by studying angle-dependent emission.

For the studies of optical nonlinearities in mono- and few-layer GaSe (Chap. 5), we used second-harmonic generation to probe the evolution of the electronic structure in atomically thin GaSe crystals. We observe a reduction of the second-order optical nonlinearity ($\chi^{(2)}$) in few-layer GaSe slabs, which is attributed to an increase of the band gap in few-layer GaSe. Our measurements are just the first step in resolving the electronic structure. There are lots of questions to be addressed, such as what are the energies of the lowest-energy direct and indirect transitions in monolayer GaSe.

For the studies of the optical Stark effect (OSE) in colloidal CdSe NQDs (Chap. 6), we developed an ultrafast method based on the OSE to directly determine the orientationally averaged oscillator strength of the lowest-energy single excitons in CdSe NQDs. By demonstrating an almost size-independent oscillator strength, we resolved a 20-year puzzle of the size-dependence of the oscillator strength in colloidal CdSe NQDs. Our results suggest that the effective mass theory

with the $k \cdot p$ method can still catch most of the features of the electronic structures in the strong confinement regime. Meanwhile, we are able to optically generate a giant pseudo-magnetic field (~ 110 T), which is due to highly reduced two-photon absorption in small NQDs that permits high pump intensity without real excitations. Such high pseudo-magnetic fields might be useful for manipulating the spin of carriers in NQDs.

APPENDICES

APPENDIX A

EXFOLIATION OF GaSe

1. Chemicals needed: acetone, isopropyl alcohol (IPA), ammonium hydroxide (28%), hydrogen peroxide (30%).
2. Solvent cleaning
 - 2.1. Soak the silicon wafer in the warm acetone bath for 5 minutes.
 - 2.2. Rinse in IPA.
 - 2.3. Rinse in DI water.
 - 2.4. Repeat 2.1 to 2.3 another two times.
 - 2.5. Blow-dry the wafer with a nitrogen gun.
3. RCA-SC1 cleaning
 - 3.1. Prepare 100 ml DI water in a Pyrex beaker, add 20 ml NH_4OH (27%), and heat up to 55 ± 5 °C on a hot plate.
 - 3.2. Add 20 ml H_2O_2 (30%). Solution will bubble vigorously after 1–2 minutes, indicating that it is ready for use.
 - 3.3. Soak the substrates in the solution for 15 minutes.
 - 3.4. Rinse in DI water.
 - 3.5. Store the substrates in clean DI water.
4. Oxygen plasma cleaning
 - 4.1. Put substrates in the plasma etcher (oxygen plasma cleaning), and pump down until the pressure is below 60 mTorr.
 - 4.2. Turn O_2 gas on, keep pressure at 500 mTorr.

- 4.3. Turn on RF, set power=100 W for 60 to 120 sec.
 - 4.4. Turn off RF and take out the substrates.
 - 4.5. Exfoliation and deposition of few-layer samples should be performed on fresh clean substrates within a few minutes.
5. Mechanical exfoliation
- 5.1. Place GaSe bulk crystal on the sticky side of the scotch tape. Peel off the sample.
 - 5.2. Fold and unfold the tape to peel off the sample smoothly and slowly. Repeat the process two or three times.
 - 5.3. Now we have 4 or 8 pieces samples (depending on the fold-unfold times). Place each sample onto a fresh substrate surface very gently.
 - 5.4. Remove the tape from the substrate.
 - 5.5. Identify few-layer samples using an optical microscope.

APPENDIX B

CALCULATION OF NUMBER OF TE AND TM MODES IN GaSe SLABS

We define a parameter $V = (n_1^2 - n_2^2)^{1/2} k d_L$, which includes the difference in the squares of the refractive indices of the core (i.e., n_1 of the GaSe slab) and the substrate (i.e., n_2 of the SiO₂ layer), the vacuum wavelength (λ_0) and wavenumber ($2\pi/\lambda_0$), and the thickness of the core slab (d_L). The total number of TE or TM modes is then determined by the following equation:

$$N = \frac{1}{\pi} \left[V - \arctan \left(\eta \sqrt{\frac{n_2^2 - n_3^2}{n_1^2 - n_2^2}} \right) \right]_{int} .$$

where n_3 is the refractive index of the capping layer (here vacuum), and the symbol $[\]_{int}$ indicates that N is the integer part of the number in brackets. The parameter η is defined as

$$\eta = \begin{cases} 1, & \text{for TE modes.} \\ n_1^2/n_3^2, & \text{for TM modes.} \end{cases}$$

The number of TE and TM modes is usually the same for most d_L . However, the number of TE modes can exceed that of the number of TM modes by one for specific ranges of d_L because $n_1/n_3 > 1$. For example, two TE modes and one TM modes exist for $243 \text{ nm} \lesssim d_L \lesssim 276 \text{ nm}$. Using $n_1 = 3.00$ (GaSe), $n_2 = 1.46$ (SiO₂), $n_3 = 1.00$ (vacuum), and $\lambda_0 = 600 \text{ nm}$ (band-edge exciton luminescence at $T \sim 10 \text{ K}$), we determine the thickness required to sustain only one guided TM mode and one TE mode to be about 162 to 242 nm.

APPENDIX C

EXCITATION-POWER-DEPENDENT EDGE AND FOCAL EMISSION

Previous studies have widely reported that the PL from GaSe generally exhibits nonlinear excitation-power responses [223, 224, 225, 43]. According to the power-law behavior in the PL spectrum, PL can be attributed to different recombination processes [225, 43] (e.g., Power law of 2, 1.5, and 1 correspond to recombinations through exciton-exciton scattering, exciton-carrier scattering, and free exciton, respectively), albeit no exact mechanisms have been determined. Fig. C.1 show a power law transition from 2 at high energy to 1 at low energy, which indicates that the PL above and below 2.07 eV is due to exciton-exciton scattering and localized excitons of unknown origin, maybe trapped by defects. We can also see that the power-law spectra of the focal and edge emission are very similar, which again evidences that both emissions are from the same source.

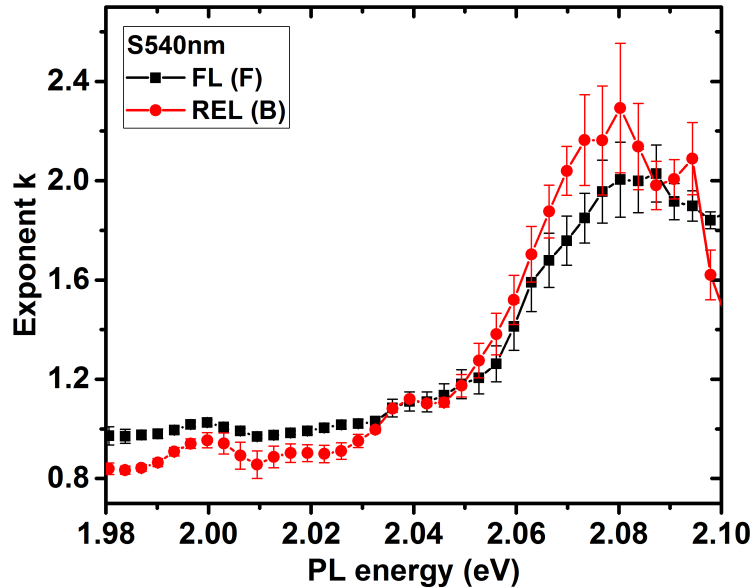


Figure C.1 **The frequency-dependent power-law fitting parameter of the REL and focal emission from S540nm at 10 K.** The PL spectra are binned with unit size of 1 nm, and are analyzed with the power-law fitting $I \propto P^k$, where I , P , and k respectively are the PL intensity, the excitation power, and the fitting parameter. Error bars only represent the error from fitting. The exponent gradually changes from 2 to 1 for PL energy from 2.1 eV to 1.98 eV (the PL spectra of S540nm can be found in Fig. 4.1).

APPENDIX D

CALCULATION OF THE OPTICAL STARK EFFECT IN CDSE NQDS

D.1 The observed optical Stark shift

The OSS of the $1S_{3/2}1S_e$ peak is due to the collective shift of individual fine-structure transitions under the peak. To determine the oscillator strength, $f_{1S_{3/2}1S_e}$, from the observed OSS, we first note that, using single-particle notation, the absorption coefficient of the Stark shifted $1S_{3/2}1S_e$ peak ($\alpha'_{1S_{3/2}1S_e}$) is given by

$$\alpha'_{1S_{3/2}1S_e}(\hbar\omega) \propto \left\langle \sum_{\substack{\beta=\uparrow,\downarrow \\ M=\pm 3/2, \pm 1/2}} g\left(\hbar\omega - [E_{\beta,M} - \delta E_{\beta,M}]\right) \left| \langle 1S_e\beta | \mathbf{e} \cdot \hat{\mathbf{r}} | 1S_{3/2}M \rangle_v \right|^2 \right\rangle,$$

where $E_{\beta,M} \equiv E_{1S_e\beta} - E_{1S_{3/2}M}$, $\delta E_{\beta,M} \equiv \sum_i \left(\delta E_{1S_e\beta}^i - \delta E_{1S_{3/2}M}^i \right)$, δE_j^i is the orientation-dependent OSS of state j due to the $i \rightarrow j$ transition, $g(\hbar\omega - E_{j,i})$ is the absorption line shape of the $i \rightarrow j$ transition, β and M are respectively the projections of the electron spin and hole angular momentum onto the NQD c axis, and the outer, angled brackets indicate an angular average over the NQD orientational distribution. The subscript v indicates the state of valence-band electrons ($M_v = -M_{\text{hole}}$). (Note that besides the use just described in δE_j^i , superscripts are used in two other ways in this manuscript. Superscripts c and v in $\delta E_j^{c(v)}$ indicate that state j is a state of the conduction or valence band, respectively, while δE_j^{obs} always refers to an observed change in transition j .) Taking each transition in the $1S_{3/2}1S_e$ manifold as characterized by the same line shape and the OSS for the transitions as small compared to the linewidth, Taylor expansion yields

$$\begin{aligned} \Delta\alpha_{1S_{3/2}1S_e}(\hbar\omega) &\equiv \left[\alpha'_{1S_{3/2}1S_e}(\hbar\omega) - \alpha_{1S_{3/2}1S_e}(\hbar\omega) \right] \\ &\propto \sum_{\beta,M} \left[\frac{dg}{d(\delta E_{\beta,M})} \Big|_{\delta E_{\beta,M}=0} \right] \left\langle \delta E_{\beta,M} \left| \langle 1S_e\beta | \mathbf{e} \cdot \hat{\mathbf{r}} | 1S_{3/2}M \rangle_v \right|^2 \right\rangle. \end{aligned}$$

The term in square brackets accounts for the dispersive shape of the DA spectrum. For linewidths much larger than the fine structure splittings, the quantity in square brackets can be taken as independent of the particular fine-structure transition, and the differential absorption coefficient becomes

$$\Delta\alpha_{1S_{3/2}1S_e}(\hbar\omega) \propto \sum_{\beta,M} \left\langle \delta E_{\beta,M} \left| \langle 1S_e\beta | \mathbf{e} \cdot \hat{\mathbf{r}} | 1S_{3/2}M \rangle_v \right|^2 \right\rangle.$$

The *observed* optical Stark shift ($\delta E_{1S_e,1S_{3/2}}^{\text{obs}}$) is defined as the uniform shift of all transitions in the $1S_{3/2}1S_e$ manifold that yields the same value of $\Delta\alpha_{1S_{3/2}1S_e}(\hbar\omega)$ as measured in DA, so that $\delta E_{1S_e,1S_{3/2}}^{\text{obs}}$ satisfies

$$\Delta\alpha_{1S_{3/2}1S_e}(\hbar\omega) \propto \delta E_{1S_e,1S_{3/2}}^{\text{obs}} \sum_{\beta,M} \left\langle \left| \langle 1S_e\beta | \mathbf{e} \cdot \hat{\mathbf{r}} | 1S_{3/2}M \rangle_v \right|^2 \right\rangle,$$

or equivalently

$$\delta E_{1S_e,1S_{3/2}}^{\text{obs}} = \frac{\left\langle \sum_{i,\beta,M} \left(\delta E_{1S_e\beta}^i - \delta E_{1S_{3/2}M}^i \right) \left| \langle 1S_e\beta | \mathbf{e} \cdot \hat{\mathbf{r}} | 1S_{3/2}M \rangle_v \right|^2 \right\rangle}{\left\langle \sum_{\beta,M} \left| \langle 1S_e\beta | \mathbf{e} \cdot \hat{\mathbf{r}} | 1S_{3/2}M \rangle_v \right|^2 \right\rangle},$$

which is Eq. 6.4.

We can choose to pull a factor of

$$\frac{|F|^2}{\epsilon_0 n_s c} I_0 \tilde{\Delta}_{1S_e,1S_{3/2}}^{-1} \left\langle \sum_{\beta,M} \left| \langle 1S_e\beta | \mathbf{e} \cdot \hat{\boldsymbol{\mu}} | 1S_{3/2}M \rangle_v \right|^2 \right\rangle,$$

out of the right side of Eq. 6.4 and write what remains as a size- and Stark-pump-energy-dependent factor $\gamma(d, E_p)$:

$$\delta E_{1S_e,1S_{3/2}}^{\text{obs}} = \gamma(d, E_p) \frac{|F|^2}{\epsilon_0 n_s c} I_0 \tilde{\Delta}_{1S_e,1S_{3/2}}^{-1} \left\langle \sum_{\beta,M} \left| \langle 1S_e\beta | \mathbf{e} \cdot \hat{\boldsymbol{\mu}} | 1S_{3/2}M \rangle_v \right|^2 \right\rangle,$$

which is Eq. 6.5. This will simply be convenient as a way of characterizing the relative contributions of different transitions to the OSS of the $1S_{3/2}1S_e$ absorption peak.

D.2 Calculation of the observed optical Stark shift

We calculate $\delta E_{1S_e, 1S_{3/2}}^{\text{obs}}$ using the effective mass approximation for the single-particle states. For clarity in the following, we reproduce the essential elements of the treatment by Ekimov et al.[67] For spherical NQDs, the electron states are labeled in terms of the orbital angular momentum, l ; its projection along the c axis, m ; and the spin β :

$$\Psi_{nlm\beta}^c(\vec{r}) = A_{ln} Y_l^m(\theta, \phi) j_l(k_{ln}r) u_{\beta}^c, \quad (\text{D.1})$$

where A_{ln} is a normalization constant, $Y_l^m(\theta, \phi)$ are spherical harmonics, $j_l(k_{ln}r)$ is the spherical Bessel function, k_{ln} is the n^{th} solution of the eigenvalue problem for the states with angular momentum l , and u_{β}^c is the conduction-band-edge Bloch function. For an infinite potential, $j_l(k_{ln}r) = 0$ at $r = a$, where a is the radius of the NQD. However, we follow Norris and Bawendi in employing a finite electron confinement potential for which the electron wave functions outside the NQD take a similar form as above but with a different wave vector, k_m , in the matrix surrounding the NQD[68]. The values of the eigenenergies and consequently k_c and k_m are determined by solution of the boundary condition expressed by Eq. 1 of Ref. [68].

The hole states are more complicated than the electron states due to the multiple valence bands. The hole states are expressed in terms of the total angular momentum, N , which is the sum of the angular momenta of the Bloch and envelope wave functions, and its projection along the c axis, M :

$$\Psi_{N,M}^{v,\pm}(\vec{r}) = \sqrt{2N+1} \left[\sum_{l^{\pm}=N\pm\frac{1}{2}, N\mp\frac{3}{2}} (-1)^{l-\frac{3}{2}+M} R_l^{\pm}(r) \sum_{\mu=-3/2}^{3/2} \begin{pmatrix} l & \frac{3}{2} & N \\ m & \mu & -M \end{pmatrix} Y_l^m(\theta, \phi) u_{3/2,\mu}^v \right. \\ \left. + (-1)^{N\pm 1/2 - 1/2 + M} R_s^{\pm}(r) \sum_{\mu=-1/2}^{1/2} \begin{pmatrix} N\pm\frac{1}{2} & \frac{1}{2} & N \\ m & \mu & -M \end{pmatrix} Y_{N\pm\frac{1}{2}}^m(\theta, \phi) u_{1/2,\mu}^v \right], \quad (\text{D.2})$$

where $m + \mu = M$, the $R_{l(s)}^{\pm}(r)$ are radial envelopes for the $J = 3/2$ ($J = 1/2$) holes, the 2×3 arrays are the Wigner $3j$ symbols, $u_{3/2,\mu}^v$ are the zone-center Bloch functions of the heavy and light hole bands, $u_{1/2,\mu}^v$ are the zone-center Bloch functions of the split-off band, and the superscript \pm refers

to the parity of the wave function. The conduction- and valence-electron Bloch functions are

$$\begin{aligned}
u_{\uparrow}^c &= S \uparrow, & u_{\downarrow}^c &= S \downarrow, \\
u_{3/2,3/2}^v &= \frac{1}{\sqrt{2}}(X + iY) \uparrow, & u_{3/2,-3/2}^v &= \frac{i}{\sqrt{2}}(X - iY) \downarrow, \\
u_{3/2,1/2}^v &= \frac{i}{\sqrt{6}}[(X + iY) \downarrow - 2Z \uparrow], & u_{3/2,-1/2}^v &= \frac{1}{\sqrt{6}}[(X - iY) \uparrow + 2Z \downarrow], \\
u_{1/2,1/2}^v &= \frac{1}{\sqrt{3}}[(X + iY) \downarrow + Z \uparrow], & u_{1/2,-1/2}^v &= \frac{i}{\sqrt{3}}[-(X - iY) \uparrow + Z \downarrow].
\end{aligned}$$

We first calculate $\delta E_{1S_e, 1S_{3/2}}^{\text{obs}}$ in the case that we neglect all transitions except the $1S_{3/2} \rightarrow 1S_e$ transition. The OSS of the $1S_e$ states is then

$$\delta E_{00\beta}^c = \frac{1}{2} \frac{e^2 |F|^2}{\epsilon_0 n_s c} I_0 \tilde{\Delta}_{1S_e, 1S_{3/2}}^{-1} \sum_{M=-3/2}^{3/2} |\langle \Psi_{00\beta}^c | \mathbf{e} \cdot \hat{\mathbf{r}} | \Psi_{\frac{3}{2}M}^{v+} \rangle|^2. \quad (\text{D.3})$$

Similarly, the shift of the hole state $\Psi_{\frac{3}{2}M}^{v+}$ is given by

$$\delta E_{\frac{3}{2}M}^v = -\frac{1}{2} \frac{e^2 |F|^2}{\epsilon_0 n_s c} I_0 \tilde{\Delta}_{1S_e, 1S_{3/2}}^{-1} \sum_{\beta} |\langle \Psi_{00\beta}^c | \mathbf{e} \cdot \hat{\mathbf{r}} | \Psi_{\frac{3}{2}M}^{v+} \rangle|^2. \quad (\text{D.4})$$

For light polarized linearly at an angle θ relative to the crystalline c axis, the wave functions of Eqs. D.1 and D.2 yield

$$\sum_{M=-3/2}^{3/2} |\langle \Psi_{00\beta}^c | \mathbf{e} \cdot \hat{\mathbf{r}} | \Psi_{\frac{3}{2}M}^{v+} \rangle|^2 = \frac{2}{3} \frac{1}{m_0^2 \omega_{1S_e, 1S_{3/2}}^2} K_0 P^2, \quad (\text{D.5})$$

where

$$P \equiv P_x = -i \langle s | \hat{p}_x | x \rangle = -i \langle s | \hat{p}_y | y \rangle = -i \langle s | \hat{p}_z | z \rangle$$

is the Kane interband matrix element and K_0 is the squared magnitude of the radial overlap integral:

$$K_0 = \left| A_{00} \int_{r=0}^a dr r^2 R_0^+(r) j_0(k_{00} r) \right|^2.$$

Although the shift of the electron states is orientation-independent, the valence band states undergo orientation-dependent Stark shifts, since

$$\sum_{\beta} |\langle \Psi_{00\beta}^c | \mathbf{e} \cdot \hat{\mathbf{r}} | \Psi_{\frac{3}{2}M}^{v+} \rangle|^2 = \frac{K_0 P^2}{m_0^2 \omega_{1S_e, 1S_{3/2}}^2} \times \begin{cases} \frac{1}{2} \sin^2 \theta, & \text{if } M = \pm \frac{3}{2} \\ \frac{2}{3} \cos^2 \theta + \frac{1}{6} \sin^2 \theta, & \text{if } M = \pm \frac{1}{2} \end{cases}. \quad (\text{D.6})$$

Using Eqs. D.3–D.6 in Eq. 6.4 yields

$$\begin{aligned}\delta E_{1S_e, 1S_{3/2}}^{\text{obs}} &= \frac{8}{15} \frac{e^2 |F|^2}{\epsilon_0 n_s c} \frac{1}{m_0^2 \omega_{1S_e, 1S_{3/2}}^2} I_0 \tilde{\Delta}_{1S_e, 1S_{3/2}}^{-1} K_0 P^2 \\ &= \gamma_0 \frac{|F|^2}{\epsilon_0 n_s c} I_0 \tilde{\Delta}_{1S_e, 1S_{3/2}}^{-1} \sum_{\beta, M} |\langle \Psi_{00\beta}^c | \mathbf{e} \cdot \hat{\boldsymbol{\mu}} | \Psi_{\frac{3}{2}M}^{\nu+} \rangle|^2,\end{aligned}\quad (\text{D.7})$$

which is Eq. 6.5 with $\gamma(d, E_p) = \gamma_0 \equiv 2/5$.

In considering all contributions to $\delta E_{1S_e, 1S_{3/2}}^{\text{obs}}$, we distinguish between interband and intraband transitions. Qualitatively, the primary difference between these terms in calculations of $\delta E_{1S_e, 1S_{3/2}}^{\text{obs}}$ is the transition matrix element in Eq. 6.1. In calculating the OSS of an electronic state due to an interband transition $i \rightarrow j$, it is easiest to calculate the matrix element $\vec{\mu}_{ji}$ in Eq. 6.1 by replacing \vec{r}_{ji} by $-i\vec{p}_{ji}/m_0\omega_{ji}$. In interband transitions, \vec{p}_{ji} yields a matrix element between Bloch wave functions, and the envelope wave functions simply yield the squared magnitude of a radial overlap integral, $K_{i,j}$, in the same way that K_0 appeared in the first line of Eq. D.7. Conversely, when calculating the OSS of an electronic state due to an intraband transition, it is easiest to calculate \vec{r}_{ji} , which yields a radial matrix element, rather than a radial overlap integral, between the envelope wave functions. For example, when calculating the OSS of the $1S_e$ state due to an intraband transition, there appears instead of $K_{i,j}$ a term

$$\tilde{K}_{1S_e, i} = \left| A_i^* A_{00} \int_{r=0}^a dr r^3 j_{l_i}(k_{c, l_i} r) j_0(k_{c, 00} r) \right|^2.$$

In \tilde{K} there appears in the integrand a factor of r^3 , rather than the factor of r^2 that appears in the integrand of $K_{i,j}$.

Using the single-particle, effective-mass approach outlined above, we have calculated the OSS due to all transitions making significant contributions to $\delta E_{1S_{3/2} 1S_e}^{\text{obs}}$. CdSe NQD size was assigned according to the sizing curve of Jasieniak et al.[71]. Past calculations of the electronic structure of CdSe NQDs using the effective mass approximation have typically assumed an infinite confinement potential[67] or a finite but unrealistically large confinement[68]. We have chosen an electron confinement potential of 4 eV based on calculations of valence band offsets[226] and experimental

cyclic voltammetry and one- and two-photon photoemission[227]. In general, high-energy states are expected to have highly oscillatory wave functions and so will have small radial integrals with the $1S_e$ and $1S_{3/2}$ states. Therefore, for all types of transitions, we set cutoffs for the energies of the transitions that we consider. These cutoffs correspond to electron confinement energies greater than about 1.6 eV, hole confinement energies greater than about 0.8 eV, and interband transition energies greater than 3.5 eV.

The contribution of transition $i \rightarrow j$ to $\delta E_{1S_{3/2}1S_e}^{\text{obs}}$ can be expressed in terms of a contribution $\gamma_{i,j}(d, E_p)$ to the total $\gamma(d, E_p)$. The interband contributions depend on the electron and hole radial functions ($j_i(r)$ and $R_l^\pm(r)$, respectively) through the radial overlap integral $K_{i,k}^{eh}$. Since the radial functions do not undergo large changes in shape with respect to r/a , these contributions are not expected to depend very sensitively on details such as the magnitudes of the confinement potentials; for a 4 eV electron confinement potential, the radial integral for the $1S_{3/2}1S_e$ transition ranges from 0.61 in our smallest NQDs to 0.76 in our largest. This can be compared to a nearly size-independent value of 0.93 for an infinite electron confinement potential.

We consider the electron and hole intraband transitions separately. The electron intraband contributions to the OSS depend on the electron radial functions via $\tilde{K}_{1S_e, j}^{ee}$ above, which leads to a $\sim a^2$ dependence of $K_{i,j}^{ee}$ on NQD radius, a . The far largest such integral is for the $1S_e \rightarrow 1P_e$ transition. In the case of an infinite confinement potential, $|\int_0^a dr r^3 f_{1S_e}(r) f_{1P_e}(r)|^2 = 0.28a^2$ [215]. For a 4 eV confinement potential, the electron wave function has a greater amplitude at larger r compared to the case of infinite confinement, so that the integral for a 4 eV confinement potential is $\sim 50\%$ larger than for an infinite confinement potential in the largest dots and $\sim 85\%$ larger in the smallest dots. However, in the OSS, the growth in the radial integral for intraband transitions is substantially offset by the diameter-dependence of the intraband transition energies. The intraband transition energies scale as $\sim a^{-2}$, so that for large, blue detunings of the Stark pump from the intraband transitions, $\tilde{\Delta}_{j, 1S_e}^{-1}$ scales approximately as a^{-2} and the product $\tilde{K}_{1S_e, j}^{ee} \tilde{\Delta}_{j, 1S_e}^{-1}$ is only weakly size-dependent.

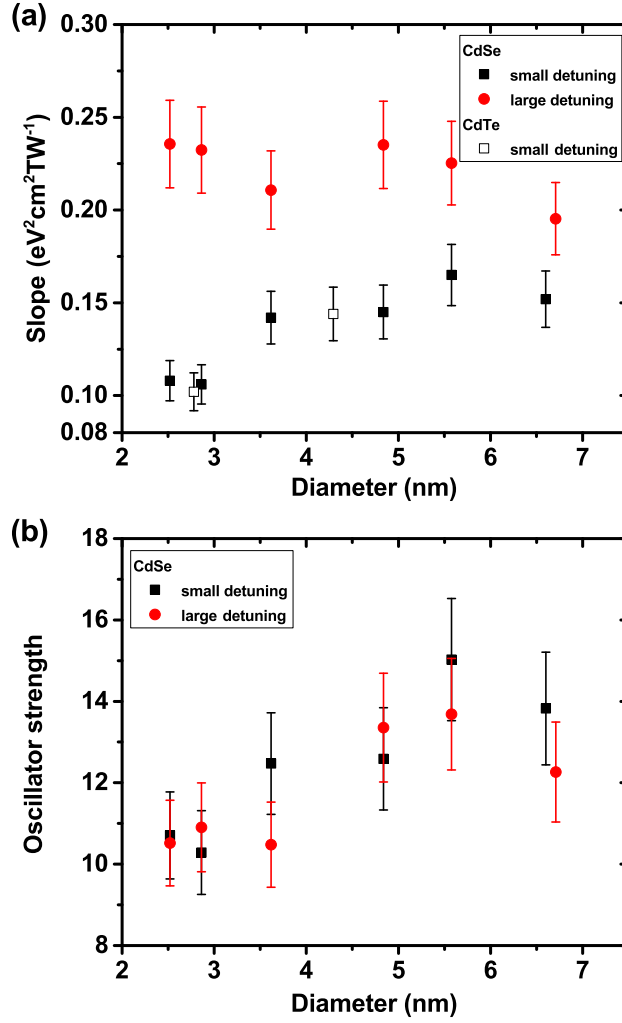


Figure D.1 **Optical Stark slopes and oscillator strengths.** Panel (a) shows the slope of the OSS, i.e., $\delta E_{1S_e,1S_{3/2}}^{\text{obs}}$ versus $I_0 \tilde{\Delta}_{1S_e,1S_{3/2}}^{-1}$, for CdSe and CdTe NQDs of different size. “Small detuning” refers to detunings for which $E_{1S_e,1S_{3/2}} - E_p < 0.3$ eV in Table D.1. The slopes and values of γ from Table D.1 yield the oscillator strengths for CdSe NQDs shown in panel (b).

We treat the hole intraband transitions somewhat differently than the electron intraband transitions. The holes are markedly heavier than the electrons and so are more sensitive to variations in the potential energy across the dot, including surface variations, core defects, and room-temperature phonon populations. Notably, the Coulomb energy is expected to exceed the hole confinement energy in all but the two smallest NQDs we have studied. This is in contrast to the

electrons for which, despite the use of a finite confinement potential in our calculations, the electron confinement energy dominates the Coulomb energy for all dot sizes studied here. Our approach is then to use the values of the hole-hole radial integrals, \tilde{K} , for the NQDs with smallest diameter in calculating the contributions in all dots of the hole intraband transitions to $\delta E_{1S_{3/2}1S_e}^{\text{obs}}$. In this case, changes of the intraband contributions with dot size are due to the change in energy spacings, which are estimated experimentally, where possible, or calculated.

For calculations of the local field factor, we assume spherical NQDs, for which

$$F = \frac{3\varepsilon_s}{\varepsilon_{\text{NQD}} + 2\varepsilon_s},$$

where ε_s and ε_{NQD} are the relative permittivities of the solvent and NQD, respectively. For energies below the $1S_{3/2} \rightarrow 1S_e$ transition, we use $\varepsilon_{\text{NQD}} = \varepsilon_{\infty, \text{pp}} + \delta\varepsilon_{\text{res}}$, where $\varepsilon_{\infty, \text{pp}}$ is the size-dependent high-frequency, non-resonant relative permittivity obtained from pseudopotential calculations[228] and where $\delta\varepsilon_{\text{res}}$ is a size-independent resonant electronic contribution to the permittivity equal to $\varepsilon_{\text{bulk}}(\hbar\omega) - \varepsilon_{\infty, \text{pp}, \text{bulk}}$, and $\varepsilon_{\text{bulk}}(\hbar\omega)$ is the measured relative permittivity for bulk CdSe[229].

The calculated values of γ , the dominant contributions $\gamma_{i,j}$, and $|F|^2$ are presented in Table D.1. Also shown in Table D.1 and Fig. D.1a is the slope, S , obtained from linear fits to the experimentally measured values of $\delta E_{1S_{3/2}1S_e}^{\text{obs}}$ versus $I_0 \tilde{\Delta}_{1S_e, 1S_{3/2}}^{-1}$ shown in Fig. 6.5a as well as the corresponding data for a Stark pump of 1.55 eV (not shown). Our values of γ and S yield the oscillator strength of the $1S_{3/2} \rightarrow 1S_e$ transition shown in Table D.1 and Figs. 6.5b and D.1b. In particular, we note that despite the different OSS measured for moderate ($-0.2 - -0.3$ eV) and large ($-0.4 - -0.9$ eV) detunings shown in Fig. D.1a, the values of the oscillator strength $f_{1S_{3/2}1S_e}$ determined from the two sets of measurements are in agreement.

Also shown in Fig. D.1a are the OSS slopes for a pair of CdTe samples comparable in size (we use the CdTe sizing curves given by Yu et al.[66]) to CdSe NQDs in the smallest and intermediate size ranges. The CdTe OSS data are very similar to the CdSe data, as expected given the similar bulk parameters (band gap, Kane parameter, and electron and hole effective masses). Given that

for CdTe NQDs of 3–7 nm diameter $f_{1S_{3/2}1S_e}^{\text{QD}} \approx 11$ [205], one would again expect an oscillator strength in strongly confined CdSe NQDs similar to what we have obtained.

$E_{1S_{3/2}1S_e}$ (eV)	diameter (nm)[71]	E_p (eV)	$\gamma_{1S_{3/2},1S_e}$	$\gamma_{1S_e,2S_{3/2}}$	$\gamma_{1S_e,1S_{1/2}}$	$\gamma_{1S_e,2S_{1/2}}$	$\gamma_{1S_e,3S_{3/2}}$	$\gamma_{1S_e,1P_e}$	γ	$ F ^2$	S ($\text{eV}^2\text{TW}^{-1}$ cm^2)	$f_{1S_{3/2}1S_e}$
2.455	2.493	2.156	0.40	0.023	0.041	0.015	0.00	0.087	0.62	0.412	0.264	10.7
2.332	2.865	2.073	0.40	0.027	0.035	0.018	0.001	0.083	0.62	0.402	0.247	10.3
2.181	3.616	1.904	0.40	0.032	0.015	0.036	0.000	0.011	0.66	0.389	0.310	12.5
2.049	4.838	1.784	0.40	0.031	0.001	0.039	0.000	0.13	0.65	0.376	0.297	12.6
1.997	5.577	1.784	0.40	0.032	0.000	0.036	0.002	0.11	0.61	0.371	0.330	15.0
1.937	6.708	1.741	0.40	0.033	0.000	0.012	0.022	0.11	0.603	0.366	0.295	13.8
2.455	2.493	1.55	0.40	0.032	0.061	0.027	0.002	0.27	1.27	0.446	0.239	10.7
2.332	2.865	1.55	0.40	0.036	0.053	0.032	0.001	0.41	1.18	0.435	0.232	10.9
2.181	3.616	1.55	0.40	0.039	0.020	0.054	0.001	0.36	1.08	0.420	0.211	10.5
2.049	4.838	1.55	0.40	0.036	0.001	0.055	0.000	0.31	0.92	0.405	0.228	13.0
1.997	5.577	1.55	0.40	0.038	0.000	0.055	0.003	0.28	0.85	0.399	0.225	13.7
1.937	6.708	1.55	0.40	0.038	0.000	0.018	0.033	0.26	0.81	0.393	0.387	12.3

Table D.1 Calculated contributions to the $1S_{3/2}1S_e$ oscillator strength. The primary contributions to γ from transitions involving the $1S_e$ state are shown for CdSe NQDs of different diameter under varying Stark pump detuning. The total value of $\gamma(d, E_p)$ is the sum of the $\gamma_{i,j}$ shown as well as the calculated contributions from intraband hole transitions and minor contributions from other electron transitions. The measured values of S , the observed OSS versus $I_0\tilde{\Delta}_{1S_e,1S_{3/2}}^{-1}$, and the square of the calculated local field factor, $|F|^2$, are used in calculating $f_{1S_{3/2}1S_e}$ from γ . Within a given row, the difference between γ and the sum of the $\gamma_{i,j}$ is primarily due to the sum of $\gamma_{1S_{3/2},j}$ over the various hole states, j .

D.3 Comparisons to previous reports

The derivation of the oscillator strength of the $1S_{3/2}1S_e$ excitons, $f_{1S_{3/2}1S_e}$, of previous studies (Fig. 6.5b) is based on the reported peak value, $\sigma(\omega_{1S_e,1S_{3/2}})$, and the corresponding energy half-width-half-maximum, Δ_{HWHM} , determined from the spectrum of the absorption cross section per NQD. Combined with Eq. 6.3, these yield

$$\sigma(\omega_{1S_e,1S_{3/2}}) = \frac{\sqrt{\ln 2}}{\Delta_{\text{HWHM}}\sqrt{\pi}} \frac{\pi e^2 \hbar |F(\omega_{1S_e,1S_{3/2}})|^2}{2\epsilon_0 n_s m_0 c} f_{1S_{3/2}1S_e}.$$

Likewise, this equation yields $\sigma(\omega_{1S_e,1S_{3/2}})$ from our values of $f_{1S_{3/2}1S_e}$ and our measured $1S_{3/2}1S_e$ linewidths. In previous studies [71, 70, 76, 66], the sizing curve affects the value of the oscillator strength. Therefore, for analyzing all studies we corrected the oscillator strength by multiplying by a factor of $(d^*/d)^3$ where d^* and d are the corrected (from Ref. [71]) and originally

reported sizes, respectively. In Fig. 6.1b, we convert $f_{1S_{3/2}1S_e}$ to $\sigma(\omega_{1S_e,1S_{3/2}})$ in a similar way and scale the absorption spectrum to match $\sigma(\omega_{1S_e,1S_{3/2}})$.

D.4 $1S_{3/2}1S_e$ Stark shift: exciton picture

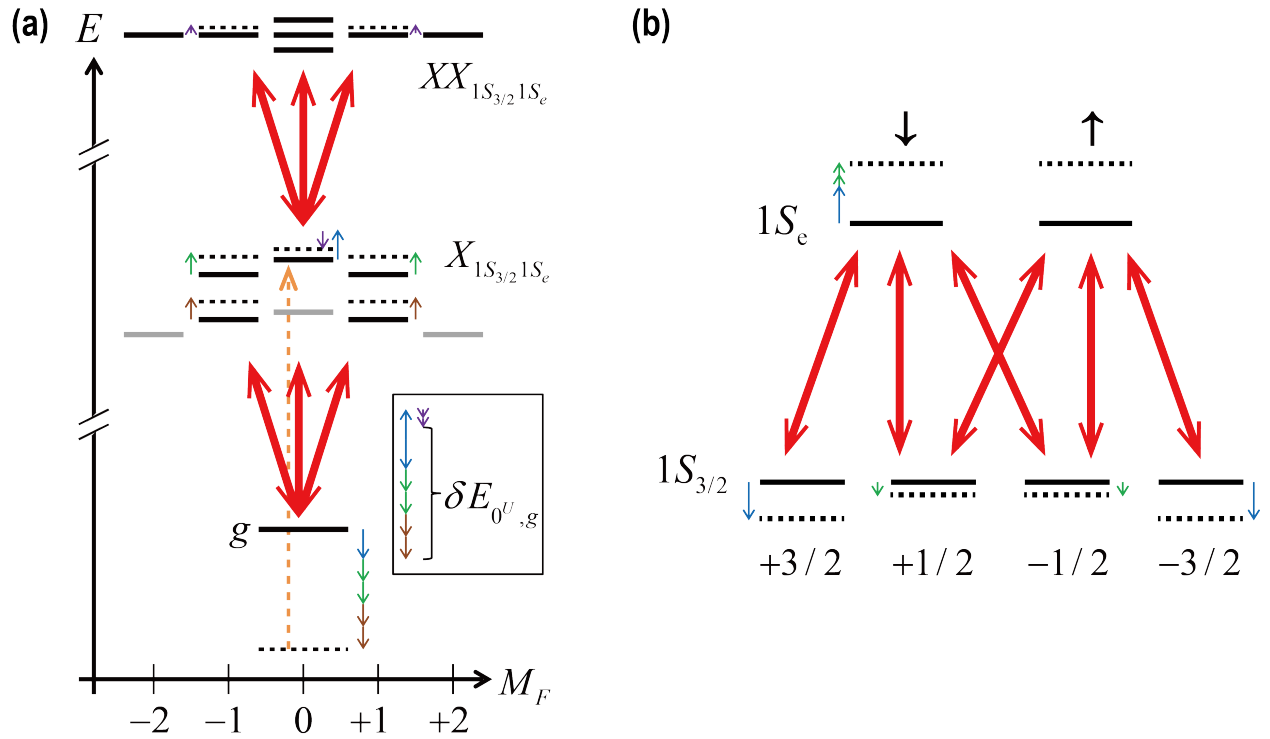


Figure D.2 $1S_{3/2}1S_e$ contributions to $1S_{3/2}1S_e$ optical Stark effect in CdSe NQDs. Excitonic (a) and single-particle (b) pictures of the optical Stark shift of the $1S_{3/2}1S_e$ states. In (a) we show the fine structure states due to transitions between the ground state and the single excitons (X) and between single and biexcitons (XX) formed from the $1S_{3/2}$ and $1S_e$ single-particle states. States (excitons in (a) or electrons and holes in (b)) are identified along the horizontal direction by the projection of the total angular momentum along the crystal c axis. Solid (dashed) horizontal lines indicate the energies of the states in the absence (presence) of the Stark pump. Gray horizontal lines indicate exciton states that are dipole-forbidden from the ground state. Thick, red arrows represent the Stark pump. Orange, dashed arrow represents one of the transitions ($G \rightarrow 0^U$ in (a) and $|J = 3/2, m_J = 1/2\rangle_v \rightarrow |L = 0, \alpha = \uparrow\rangle$ in (b)) seen by the probe beam. Thin solid arrows indicate the magnitude of the Stark shift associated with different transitions. The inset of panel (a) shows the OSS of the $G \rightarrow 0^U$ transition. This is given by the downward shift of the ground state due to all the transitions from the ground state to single excitons and the net shift of the state 0^U due to the transition $G \rightarrow 0^U$ as well as the three allowed transitions from 0^U to biexcitons.

The energy-integrated oscillator strength of the $1S_{3/2}1S_e$ peak is affected by the size-dependent $1S_{3/2}1S_e$ exciton fine structure. For simplicity, we consider only the contribution of the $1S_{3/2} \rightarrow 1S_e$ transition to the OSS of the $1S_{3/2}1S_e$ peak.

As illustrated in Fig. D.2a, the The OSS of a transition from the ground-state, G , to a given exciton fine-structure state, X_n , is determined by the shift of X_n due to the OSE through the $G \rightarrow X_n$ transition, the shift of G due to the OSE through *all* transitions out of the ground state, and the shift of X_n due to transitions from X_n to all optically allowed biexcitons, XX_k [212]:

$$\delta E_{X_n,G} = \frac{1}{2} \frac{e^2 |F|^2}{\epsilon_0 n_s c} I_0 \left\{ |\langle X_n | \mathbf{e} \cdot \hat{\mathbf{r}} | G \rangle|^2 \tilde{\Delta}_{X_n,G}^{-1} + \sum_j |\langle X_j | \mathbf{e} \cdot \hat{\mathbf{r}} | G \rangle|^2 \tilde{\Delta}_{X_j,G}^{-1} + \sum_k |\langle XX_k | \mathbf{e} \cdot \hat{\mathbf{r}} | X_n \rangle|^2 \tilde{\Delta}_{XX_k,X_n}^{-1} \right\}$$

In the case that the fine-structure splittings and biexciton binding are small compared to the Stark field detuning, we can approximate $\tilde{\Delta}_{XX_k,X_n}^{-1} \approx \tilde{\Delta}_{X_j,G}^{-1} \approx \tilde{\Delta}_{X_n,G}^{-1}$, so that

$$\delta E_{X_n,G} = \frac{1}{2} \frac{e^2 |F|^2}{\epsilon_0 n_s c} I_0 \tilde{\Delta}_{X_n,G}^{-1} \left(|\langle X_n | \mathbf{e} \cdot \hat{\mathbf{r}} | G \rangle|^2 + \sum_j |\langle X_j | \mathbf{e} \cdot \hat{\mathbf{r}} | G \rangle|^2 + \sum_k |\langle XX_k | \mathbf{e} \cdot \hat{\mathbf{r}} | X_n \rangle|^2 \right). \quad (\text{D.8})$$

In addressing the exciton fine structure, we follow the treatment of Efros et al.[69] The four $1S_{3/2}$ and two $1S_e$ states give rise to eight exciton states (the exciton fine structure), which are illustrated in Fig. D.2a. These are labeled by the projection of their total angular momentum along the c axis: the bright (dipole-allowed) states $X = 0^U$, $1^{\pm U}$, and $1^{\pm L}$ and the dark states $X = 0^L$ and $X = \pm 2$. The exciton wave functions can be expressed as products of radial envelope functions and Bloch functions of the conduction and valence bands. Using single-particle, electron(e)-hole(h) basis functions $|e, h\rangle$ and dropping explicit reference to the radial functions and the total angular

momentum of the single-particle states, the exciton states can be written

$$\begin{aligned}
|0^U\rangle &= \frac{1}{\sqrt{2}} \left(-i|\uparrow; -1/2\rangle + |\downarrow; +1/2\rangle \right) \\
|+1^{U,L}\rangle &= \mp iC_{\pm}|\uparrow; +1/2\rangle + C_{\mp}|\downarrow; +3/2\rangle \\
|-1^{U,L}\rangle &= \mp iC_{\mp}|\uparrow; -3/2\rangle + C_{\pm}|\downarrow; -1/2\rangle
\end{aligned}$$

where $|\beta; m\rangle$ refers to the electron-hole pair state consisting of a spin β electron in the conduction band and a $|J = 3/2, m\rangle$ hole, the upper(lower) sign of the \pm and \mp pairs are associated with the $U(L)$ states,

$$C_{\pm} = \sqrt{\frac{\sqrt{\psi^2 + 3\eta^2} \pm \psi}{2\sqrt{\psi^2 + 3\eta^2}}},$$

$\psi = (\Delta - 2\eta)/2$, Δ is the total splitting of the hole state and is the sum of crystal field and shape splitting, and η is given by

$$\eta = \left(\frac{a_B}{a}\right)^3 \hbar\omega_{ST}\chi(\beta),$$

where $a_B = 5.6$ nm is the bulk exciton Bohr radius, $\hbar\omega_{ST} = 0.13$ meV is the singlet-triplet splitting of the lowest-energy exciton in bulk, $\beta = 0.28$ is the ratio of heavy-hole to light-hole masses, and $\chi(\beta)$ describes the radial overlap of the electron and hole envelope functions.

For light with linear polarization at an angle θ to the NQD c axis, the squared magnitude of the momentum matrix elements, $p_{X_n,G}$, between the ground state (G) and the bright $1S_{3/2}1S_e$ excitons (X_n) are then given by

$$\begin{aligned}
|p_{0U,G}|^2 &= \frac{4}{3}K_0P^2 \cos^2 \theta \\
|p_{-1^{U,L},G}|^2 &= |p_{+1^{U,L},G}|^2 = \frac{1}{6} \left(1 + 2C_{\mp}^2 \pm \frac{3\eta}{\sqrt{\psi^2 + 3\eta^2}} \right) K_0P^2 \sin^2 \theta.
\end{aligned}$$

To calculate the impact of biexcitons (the third term in Eq. D.8) in the OSS we follow the treatment by Rodina and Efros of the biexciton fine structure derived from the $1S_{3/2}$ and $1S_e$ states [214]. There are only six possible biexciton states derived from the $1S_{3/2}$ and $1S_e$ states: a four-fold degenerate set of states with total angular momentum $N = 2$ and labeled by the projection of angular momentum onto the c axis of $M_N = \pm 2$ and $M_N = \pm 1$, and two non-degenerate states

of $M_N = 0$, labeled 0^+ and 0^- . The relative probabilities for transitions from each of the $1S_{3/2}1S_e$ excitons to each of the $1S_{3/2}1S_e$ biexcitons is given in Table 1 of Ref. [214]. For example, the sum of squared momentum matrix elements for transitions from 0^U to the various biexciton states is

$$\begin{aligned}\sum_i |p_{XX_i,0^U}|^2 &= \left| \langle XX_{0^-} | \mathbf{e} \cdot \hat{\mathbf{p}} | 0^U \rangle \right|^2 + \left| \langle XX_{0^+} | \mathbf{e} \cdot \hat{\mathbf{p}} | 0^U \rangle \right|^2 + \left| \langle XX_{+1} | \mathbf{e} \cdot \hat{\mathbf{p}} | 0^U \rangle \right|^2 \\ &\quad + \left| \langle XX_{-1} | \mathbf{e} \cdot \hat{\mathbf{p}} | 0^U \rangle \right|^2 \\ &= \left(\frac{1}{2} \sin^2 \theta + \frac{4}{3} \cos^2 \theta \right) K_0 P^2.\end{aligned}$$

Similarly, the momentum matrix elements for the biexciton transitions from the other bright single excitons yield

$$\begin{aligned}\sum_i |p_{XX_i,\pm 1^U}|^2 &= \frac{1}{3} \left(2 - 2C_+^2 \cos^2 \theta + \sqrt{3} C_+ C_- \sin^2 \theta \right) K_0 P^2 \\ \sum_i |p_{XX_i,\pm 1^L}|^2 &= \frac{1}{3} \left(2 - 2C_-^2 \cos^2 \theta - \sqrt{3} C_+ C_- \sin^2 \theta \right) K_0 P^2.\end{aligned}$$

With the relative probabilities for all of the ground-to-single-exciton transitions and single-to-biexciton transitions, we can calculate the OSS for each of the transitions from the ground to single-exciton states associated with the $1S_{3/2}1S_e$ peak. The OSS of the ground state is given by

$$\begin{aligned}\delta E_G &= -\frac{1}{2} \xi \left(2|p_{+1^U,G}|^2 + 2|p_{+1^L,G}|^2 + |p_{0^U,G}|^2 \right) \\ &= -\frac{2}{3} \xi K_0 P^2,\end{aligned}$$

where, from Eq. D.8 and the relationship $\vec{p}_{kj} = im_0 \omega_k j \vec{r}_{kj}$,

$$\xi \equiv \frac{1}{m_0^2 \omega_{1S_e,1S_{3/2}}^2} \frac{e^2 |F|^2}{\epsilon_0 n_{sc}} I_0 \tilde{\Delta}_{1S_e,1S_{3/2}}^{-1}.$$

The shift of the ground state is independent of orientation. The OSSs of the transitions from G to the bright $1S_{3/2}1S_e$ excitons are given by

$$\begin{aligned}\delta E_{\pm 1^U,G} &= \frac{1}{2} \xi \left(|p_{\pm 1^U}|^2 - |p_{\pm XX,1^U}|^2 \right) - \delta E_G \\ \delta E_{\pm 1^L,G} &= \frac{1}{2} \xi \left(|p_{\pm 1^L}|^2 - |p_{XX,\pm 1^L}|^2 \right) - \delta E_G \\ \delta E_{0^U,G} &= \frac{1}{2} \xi \left(|p_{0^U}|^2 - |p_{XX,0^U}|^2 \right) - \delta E_G\end{aligned}$$

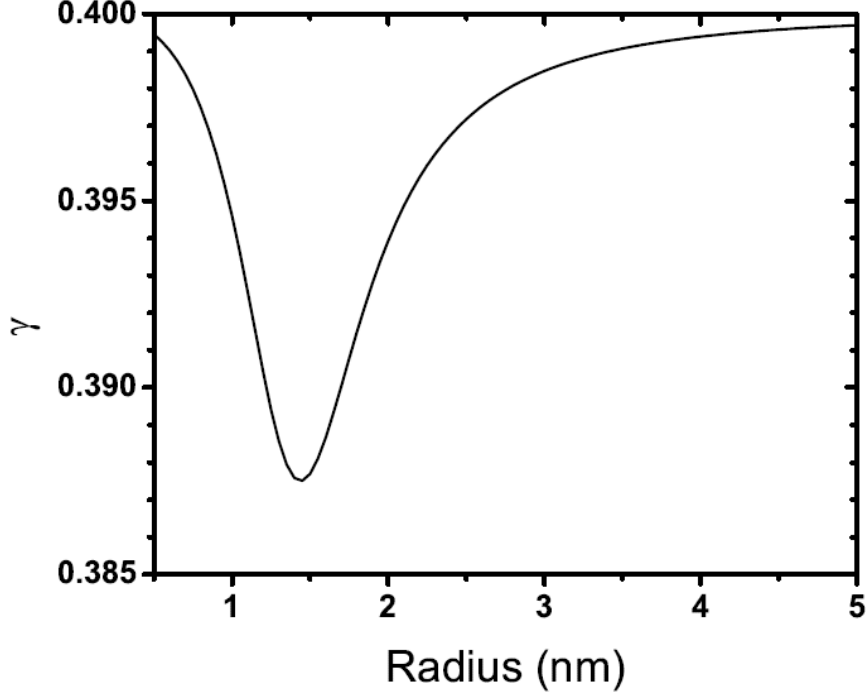


Figure D.3 **Size-dependent scaling factor γ relating the magnitude of the observed optical Stark shift of the $1S_{3/2}1S_e$ peak to the total oscillator strength of the $1S_{3/2}1S_e$ peak.**

Since the $1S_{3/2}1S_e$ absorption peak is broad compared to the splittings between the excitons, then as shown in the Appendix D.1, the experimentally observed OSS is an average of the OSS of all the transitions that comprise the $1S_{3/2}1S_e$ peak weighted by the relative strength of each transition:

$$\begin{aligned} \delta E_{1S_e, 1S_{3/2}}^{\text{obs}} &= \frac{\left\{ \int_0^\pi \left(2\delta E_{+1U,G} |p_{+1U,G}|^2 + 2\delta E_{+1L,G} |p_{+1L,G}|^2 + \delta E_{0U,G} |p_{0U,G}|^2 \right) \sin \theta d\theta \right\}}{\left\{ \int_0^\pi \left(2|p_{+1U,G}|^2 + 2|p_{+1L,G}|^2 + |p_{0U,G}|^2 \right) \sin \theta d\theta \right\}} \\ &= \frac{8}{15} \xi K_0 P^2 \left\{ 1 - \frac{1}{12} \left[C_+^2 C_-^2 - \frac{\sqrt{3}}{2} (C_-^2 - C_+^2) C_+ C_- \right] \right\}. \end{aligned} \quad (\text{D.9})$$

Noting that angular averaging of $|\mathbf{e} \cdot \vec{\mu}_{n,G}|^2$ over all orientations yields

$$\begin{aligned} \sum_n \langle |\mathbf{e} \cdot \vec{\mu}_{n,G}|^2 \rangle &= e^2 \sum_{\beta, M} |\langle \Psi_{00\beta}^c | \mathbf{e} \cdot \hat{\mathbf{r}} | \Psi_{\frac{3}{2}M}^{\nu+} \rangle|^2 \\ &= \frac{e^2}{m^2 \omega_{1S_e, 1S_{3/2}}^2} \frac{4}{3} K_0 P^2, \end{aligned} \quad (\text{D.10})$$

we can rewrite Eq. D.9 as

$$\delta E_{1S_e, 1S_{3/2}}^{\text{obs}} = \gamma \frac{|F|^2}{\epsilon_0 n_s c} \frac{I_0}{\bar{\Delta}_{1S_e, 1S_{3/2}}} \sum_n \langle |\langle X_n | \mathbf{e} \cdot \hat{\mu} | G \rangle|^2 \rangle, \quad (\text{D.11})$$

where

$$\gamma \equiv \frac{2}{5} \left\{ 1 - \frac{1}{12} \left[C_+^2 C_-^2 - \frac{\sqrt{3}}{2} (C_-^2 - C_+^2) C_+ C_- \right] \right\}.$$

Using the fact that $|C_+ C_-|^2 < 1/4$ and $|(C_-^2 - C_+^2) C_+ C_-| \leq 1/4$, we find that $\gamma \approx 2/5$, which is the value of γ_0 found in the single-particle picture. In Figure D.3, we plot γ , which shows deviations of $\lesssim 3\%$ from the value of $\gamma_0 = 2/5$. In other words, for large detunings, γ is nearly equal to the size-independent single-particle value.

BIBLIOGRAPHY

BIBLIOGRAPHY

- [1] K. v. Klitzing, G. Dorda, and M. Pepper. New method for high-accuracy determination of the fine-structure constant based on quantized hall resistance. *Phys. Rev. Lett.*, 45:494–497, 1980.
- [2] H. Y. Hwang, Y. Iwasa, M. Kawasaki, B. Keimer, N. Nagaosa, and Y. Tokura. Emergent phenomena at oxide interfaces. *Nat. Mater.*, 11(2):103–113, 2012.
- [3] K. S. Novoselov, A. K. Geim, S. V. Morozov, D. Jiang, Y. Zhang, S. V. Dubonos, I. V. Grigorieva, and A. A. Firsov. Electric field effect in atomically thin carbon films. *Science*, 306(5696):666–669, 2004.
- [4] A. H. Castro Neto, F. Guinea, N. M. R. Peres, K. S. Novoselov, and A. K. Geim. The electronic properties of graphene. *Rev. Mod. Phys.*, 81:109–162, 2009.
- [5] K.I. Bolotin, K.J. Sikes, Z. Jiang, M. Klima, G. Fudenberg, J. Hone, P. Kim, and H.L. Stormer. Ultrahigh electron mobility in suspended graphene. *Solid State Communications*, 146(9–10):351 – 355, 2008.
- [6] L. Wang, I. Meric, P. Y. Huang, Q. Gao, Y. Gao, H. Tran, T. Taniguchi, K. Watanabe, L. M. Campos, D. A. Muller, J. Guo, P. Kim, J. Hone, K. L. Shepard, and C. R. Dean. One-dimensional electrical contact to a two-dimensional material. *Science*, 342(6158):614–617, 2013.
- [7] K. S. Novoselov, A. K. Geim, S. V. Morozov, D. Jiang, M. I. Katsnelson, I. V. Grigorieva, S. V. Dubonos, and A. A. Firsov. Two-dimensional gas of massless Dirac fermions in graphene. *Nature*, 438(7065):197–200, 2005.
- [8] Yuanbo Zhang, Yan-Wen Tan, Horst L. Stormer, and Philip Kim. Experimental observation of the quantum Hall effect and Berry’s phase in graphene. *Nature*, 438(7065):201–204, 2005.
- [9] Richard Balog, Bjarke Jorgensen, Louis Nilsson, Mie Andersen, Emile Rienks, Marco Bianchi, Mattia Fanetti, Erik Laegsgaard, Alessandro Baraldi, Silvano Lizzit, Zeljko Sljivancanin, Flemming Besenbacher, Bjork Hammer, Thomas G. Pedersen, Philip Hofmann, and Liv Hornekaer. Bandgap opening in graphene induced by patterned hydrogen adsorption. *Nat. Mater.*, 9(4):315–319, 2010.
- [10] Xiaodong Xu, Wang Yao, Di Xiao, and Tony F. Heinz. Spin and pseudospins in layered transition metal dichalcogenides. *Nat. Phys.*, 10(5):343–350, 2014.
- [11] Hualing Zeng, Junfeng Dai, Wang Yao, Di Xiao, and Xiaodong Cui. Valley polarization in MoS2 monolayers by optical pumping. *Nat. Nano.*, 7(8):490–493, 2012.
- [12] Ting Cao, Gang Wang, Wenpeng Han, Huiqi Ye, Chuanrui Zhu, Junren Shi, Qian Niu, Pingheng Tan, Enge Wang, Baoli Liu, and Ji Feng. Valley-selective circular dichroism of monolayer molybdenum disulphide. *Nat. Commun.*, 3:887, 2012.

- [13] Kin Fai Mak, Keliang He, Jie Shan, and Tony F. Heinz. Control of valley polarization in monolayer mos2 by optical helicity. *Nat. Nano.*, 7(8):494–498, 2012.
- [14] Jonghwan Kim, Xiaoping Hong, Chenhao Jin, Su-Fei Shi, Chih-Yuan S. Chang, Ming-Hui Chiu, Lain-Jong Li, and Feng Wang. Ultrafast generation of pseudo-magnetic field for valley excitons in WSe₂ monolayers. *Science*, 346(6214):1205–1208, 2014.
- [15] Edbert J. Sie, James W. McIver, Yi-Hsien Lee, Liang Fu, Jing Kong, and Nuh Gedik. Valley-selective optical Stark effect in monolayer WS₂. *Nat. Mater.*, 14(3):290–294, 2015.
- [16] Ziliang Ye, Dezheng Sun, and Tony F. Heinz. Optical manipulation of valley pseudospin. *Nat. Phys.*, 13(1):26–29, 2017.
- [17] Jieun Lee, Kin Fai Mak, and Jie Shan. Electrical control of the valley Hall effect in bilayer mos2 transistors. *Nat. Nano.*, 11(5):421–425, 2016.
- [18] Alexey Chernikov, Timothy C. Berkelbach, Heather M. Hill, Albert Rigosi, Yilei Li, Ozgur Burak Aslan, David R. Reichman, Mark S. Hybertsen, and Tony F. Heinz. Exciton binding energy and nonhydrogenic Rydberg series in monolayer WS₂. *Phys. Rev. Lett.*, 113:076802, 2014.
- [19] Radisavljevic B., Radenovic A., Brivio J., Giacometti V., and Kis A. Single-layer MoS₂ transistors. *Nat. Nano.*, 6(3):147–150, 2011.
- [20] Likai Li, Fangyuan Yang, Guo Jun Ye, Zuocheng Zhang, Zengwei Zhu, Wenkai Lou, Xiaoying Zhou, Liang Li, Kenji Watanabe, Takashi Taniguchi, Kai Chang, Yayu Wang, Xian Hui Chen, and Yuanbo Zhang. Quantum Hall effect in black phosphorus two-dimensional electron system. *Nat. Nano.*, 11(7):593–597, 2016.
- [21] R. Dean C., F. Young A., Meric I., Lee C., Wang L., Sorgenfrei S., Watanabe K., Taniguchi T., Kim P., L. Shepard K., and Hone J. Boron nitride substrates for high-quality graphene electronics. *Nat. Nano.*, 5(10):722–726, 2010.
- [22] Xiaoxiang Xi, Liang Zhao, Zefang Wang, Helmuth Berger, László Forró, Jie Shan, and Kin Fai Mak. Strongly enhanced charge-density-wave order in monolayer NbSe₂. *Nat. Nano.*, 10(9):765–769, 2015.
- [23] Xiaoxiang Xi, Zefang Wang, Weiwei Zhao, Ju-Hyun Park, Kam Tuen Law, Helmuth Berger, Laszlo Forro, Jie Shan, and Kin Fai Mak. Ising pairing in superconducting NbSe₂ atomic layers. *Nat. Phys.*, 12(2):139–143, 2016.
- [24] Hongming Weng, Xi Dai, and Zhong Fang. Transition-metal pentatelluride ZrTe₅ and HfTe₅: A paradigm for large-gap quantum spin Hall insulators. *Phys. Rev. X*, 4:011002, 2014.
- [25] Valentin G Dmitriev, Gagik G Gurzadyan, and David N Nikogosyan. *Handbook of Nonlinear Optical Crystals*, volume 64. Springer, 2013.

- [26] N. C. Fernelius. Properties of gallium selenide single crystal. *Prog. Crystal Growth and Charact. Mater.*, 28(4):275–353, 1994.
- [27] Alexander Sell, Alfred Leitenstorfer, and Rupert Huber. Phase-locked generation and field-resolved detection of widely tunable terahertz pulses with amplitudes exceeding 100 MV/cm. *Opt. Lett.*, 33(23):2767–2769, 2008.
- [28] Wei Shi and Yujie J. Ding. A monochromatic and high-power terahertz source tunable in the ranges of 2.7–38.4 and 58.2–3540 μm for variety of potential applications. *Applied Physics Letters*, 84(10):1635–1637, 2004.
- [29] E. M. Gamarts, E. L. Ivchenko, M. I. Karaman, V. P. Mushinskii, G. E. Pikus, B. S. Razbirin, and A. N. Starukhin. Optical orientation and alignment of free excitons in GaSe during resonance excitation. Experiment. *Sov. Phys. JETP*, 46:590, 1977.
- [30] E. L. Ivchenko, G. E. Pikus, B. S. Razbirin, and A. I. Starukhin. Optical orientation and alignment of free excitons in GaSe under resonant excitation. Theory. *Sov. Phys. JETP*, 45(6):1172–1180, 1977.
- [31] L. Schultheis, J. Kuhl, A. Honold, and C. W. Tu. Picosecond phase coherence and orientational relaxation of excitons in gaas. *Phys. Rev. Lett.*, 57:1797–1800, 1986.
- [32] E. O. Göbel, K. Leo, T. C. Damen, J. Shah, S. Schmitt-Rink, W. Schäfer, J. F. Müller, and K. Köhler. Quantum beats of excitons in quantum wells. *Phys. Rev. Lett.*, 64:1801–1804, 1990.
- [33] H. L. Zhuang and R. G. Hennig. Single-layer group-III monochalcogenide photocatalysts for water splitting. *Chem. Mater.*, 25(15):3232–3238, 2013.
- [34] Dat T. Do, Subhendra D. Mahanti, and Chih Wei Lai. Spin splitting in 2d monochalcogenide semiconductors. *Scientific Reports*, 5:17044, 2015.
- [35] Pengke Li and Ian Appelbaum. Symmetry, distorted band structure, and spin-orbit coupling of Group-III metal-monochalcogenide monolayers. *Phys. Rev. B*, 92:195129, 2015.
- [36] Ting Cao, Zhenglu Li, and Steven G. Louie. Tunable magnetism and half-metallicity in hole-doped monolayer GaSe. *Phys. Rev. Lett.*, 114:236602, 2015.
- [37] Zs. Rak, S.D. Mahanti, Krishna C. Mandal, and N.C. Fernelius. Electronic structure of substitutional defects and vacancies in GaSe. *Journal of Physics and Chemistry of Solids*, 70(2):344 – 355, 2009.
- [38] E. Mooser and M. Schlüter. The band-gap excitons in gallium selenide. *Nuovo Cimento B*, 18(1):164–208, 1973.
- [39] P. Fielding, G. Fischer, and E. Mooser. Semiconductors of the type III-VI. *Journal of Physics and Chemistry of Solids*, 8:434 – 437, 1959.

- [40] E. Aulich, J. L. . L. Brebner, and E. Mooser. Indirect energy gap in GaSe and GaS. *Phys. Status Solidi B*, 31(1):129–131, 1969.
- [41] A. Mercier, E. Mooser, and J. P. Voitchovsky. Resonant exciton in GaSe. *Phys. Rev. B*, 12:4307–4311, 1975.
- [42] Le Chi Thanh and C. Depeursinge. Absorption and electroabsorption near the indirect edge of GaSe. *Solid State Communications*, 21(3):317 – 321, 1977.
- [43] Vito Capozzi, Lorenzo Pavesi, and Jean Louis Staehli. Exciton-carrier scattering in gallium selenide. *Phys. Rev. B*, 47:6340–6349, 1993.
- [44] M. O. D. Camara, A. Mauger, and I. Devos. Electronic structure of the layer compounds GaSe and InSe in a tight-binding approach. *Phys. Rev. B*, 65:125206, 2002.
- [45] George F Koster. *Properties of the Thirty-Two Point Groups*, volume 24. The MIT Press, 1963.
- [46] M. Schlüter, J. Camassel, S. Kohn, J. P. Voitchovsky, Y. R. Shen, and Marvin L. Cohen. Optical properties of GaSe and GaS_xSe_{1-x} mixed crystals. *Phys. Rev. B*, 13(8):3534–3547, 1976.
- [47] Y. Sasaki and Y. Nishina. Photoluminescence studies of indirect bound excitons in ϵ -GaSe. *Phys. Rev. B*, 23(8):4089–4096, 1981.
- [48] Y. Sasaki, C. Hamaguchi, and J. Nakai. Electroreflectance of GaSe. I. Around 3.4 eV. *J. Phys. Soc. Jpn.*, 38(1):162–168, 1975.
- [49] Y. Sasaki, C. Hamaguchi, and J. Nakai. Electroreflectance of GaSe. II. 3.5-4.1 eV region. *J. Phys. Soc. Jpn.*, 38(1):169–174, 1975.
- [50] Alexey I. Ekimov and Alexei A. Onushchenko. Quantum size effect in three-dimensional microscopic semiconductor crystals. *JETP Lett.*, 34(6):345–349, 1981.
- [51] Al. L. Efros and Al. L. Efros. Interband absorption of light in a semiconductor sphere. *Soviet Physics Semiconductors*, 16(7):772–775, 1982.
- [52] Tadashi Itoh and Toshio Kirihara. Excitons in CuCl microcrystals embedded in NaCl. *Journal of Luminescence*, 31:120 – 122, 1984.
- [53] R. Rossetti, S. Nakahara, and L. E. Brus. Quantum size effects in the redox potentials, resonance Raman spectra, and electronic spectra of CdS crystallites in aqueous solution. *The Journal of Chemical Physics*, 79(2):1086–1088, 1983.
- [54] L. E. Brus. Electron-electron and electron-hole interactions in small semiconductor crystallites: The size dependence of the lowest excited electronic state. *J. Chem. Phys.*, 80(9):4403–4409, 1984.
- [55] Louis Brus. Electronic wave functions in semiconductor clusters: experiment and theory. *The Journal of Physical Chemistry*, 90(12):2555–2560, 1986.

- [56] D. Leonard, K. Pond, and P. M. Petroff. Critical layer thickness for self-assembled InAs islands on GaAs. *Phys. Rev. B*, 50:11687–11692, 1994.
- [57] K. Kash. Optical properties of III–V semiconductor quantum wires and dots. *Journal of Luminescence*, 46(2):69 – 82, 1990.
- [58] Yadong Yin and A. Paul Alivisatos. Colloidal nanocrystal synthesis and the organic-inorganic interface. *Nature*, 437(7059):664–670, 2005.
- [59] Jin Young Kim, Oleksandr Voznyy, David Zhitomirsky, and Edward H. Sargent. 25th anniversary article: Colloidal quantum dot materials and devices: A quarter-century of advances. *Advanced Materials*, 27(26):3849–3849, 2015.
- [60] C. B. Murray, D. J. Norris, and M. G. Bawendi. Synthesis and characterization of nearly monodisperse CdE (E = sulfur, selenium, tellurium) semiconductor nanocrystallites. *Journal of the American Chemical Society*, 115(19):8706–8715, 1993.
- [61] V.S. Dneprovskii, V.I. Klimov, D.K. Okorokov, and Yu.V. Vandyshv. Strong optical nonlinearities and laser emission of semiconductor microcrystals. *Solid State Communications*, 81(3):227 – 230, 1992.
- [62] V. I. Klimov, A. A. Mikhailovsky, Su Xu, A. Malko, J. A. Hollingsworth, C. A. Leatherdale, H.-J. Eisler, and M. G. Bawendi. Optical gain and stimulated emission in nanocrystal quantum dots. *Science*, 290(5490):314–317, 2000.
- [63] Victor I. Klimov. Multicarrier interactions in semiconductor nanocrystals in relation to the phenomena of Auger recombination and carrier multiplication. *Annu. Rev. Condens. Matter Phys.*, 5(1):285–316, 2014.
- [64] Victor I. Klimov, Sergei A. Ivanov, Jagjit Nanda, Marc Achermann, Ilya Bezel, John A. McGuire, and Andrei Piryatinski. Single-exciton optical gain in semiconductor nanocrystals. *Nature*, 447(7143):441–446, 2007.
- [65] Dmitri V. Talapin, Jong-Soo Lee, Maksym V. Kovalenko, and Elena V. Shevchenko. Prospects of colloidal nanocrystals for electronic and optoelectronic applications. *Chemical Reviews*, 110(1):389–458, 2010.
- [66] W. William Yu, Lianhua Qu, Wenzhuo Guo, and Xiaogang Peng. Experimental determination of the extinction coefficient of CdTe, CdSe, and CdS nanocrystals. *Chem. Mater.*, 15(14):2854–2860, 2003.
- [67] A. I. Ekimov, F. Hache, M. C. Schanne-Klein, D. Ricard, C. Flytzanis, I. A. Kudryavtsev, T. V. Yazeva, A. V. Rodina, and Al. L. Efros. Absorption and intensity-dependent photoluminescence measurements on CdSe quantum dots: Assignment of the first electronic transitions. *J. Opt. Soc. Am. B*, 10(1):100–107, 1993.
- [68] D. J. Norris and M. G. Bawendi. Measurement and assignment of the size-dependent optical spectrum in CdSe quantum dots. *Phys. Rev. B*, 53:16338–16346, 1996.

- [69] Al. L. Efros, M. Rosen, M. Kuno, M. Nirmal, D. J. Norris, and M. Bawendi. Band-edge exciton in quantum dots of semiconductors with a degenerate valence band: Dark and bright exciton states. *Phys. Rev. B*, 54:4843–4856, 1996.
- [70] C.A. Leatherdale, W.-K. Woo, F. V. Mikulec, and M. G. Bawendi. On the absorption cross section of CdSe nanocrystal quantum dots. *J. Phys. Chem. B*, 106(31):7619–7622, 2002.
- [71] Jacek Jasieniak, Lisa Smith, Joel van Embden, Paul Mulvaney, and Marco Califano. Re-examination of the size-dependent absorption properties of CdSe quantum dots. *J. Phys. Chem. C*, 113(45):19468–19474, 2009.
- [72] R. K. Čapek, I. Moreels, K. Lambert, D. De Muynck, Q. Zhao, A. Vantomme, F. Vanhaecke, and Z. Hens. Optical properties of zincblende cadmium selenide quantum dots. *J. Phys. Chem. C*, 114(14):6371–6376, 2010.
- [73] Yong-Nian Xu and W. Y. Ching. Electronic, optical, and structural properties of some wurtzite crystals. *Phys. Rev. B*, 48:4335–4351, 1993.
- [74] Otfried Madelung. II-VI Compounds. In *Semiconductors: Data Handbook*, pages 173–244. Springer, 2004.
- [75] E. Hanamura. Very large optical nonlinearity of semiconductor microcrystallites. *Phys. Rev. B*, 37(3):1273–1279, 1988.
- [76] Victor I. Klimov. Optical nonlinearities and ultrafast carrier dynamics in semiconductor nanocrystals. *J. Phys. Chem. B*, 104(26):6112–6123, 2000.
- [77] Robert A. Kaindl, Matthias Wurm, Klaus Reimann, Peter Hamm, Andrew M. Weiner, and Michael Woerner. Generation, shaping, and characterization of intense femtosecond pulses tunable from 3 to 20 micrometers. *J. Opt. Soc. Am. B*, 17(12):2086–2094, 2000.
- [78] S. Arzhantsev and M. Maroncelli. Design and characterization of a femtosecond fluorescence spectrometer based on optical Kerr gating. *Appl. Spectrosc.*, 59(2):206–220, 2005.
- [79] J. Takeda, K. Nakajima, S. Kurita, S. Tomimoto, S. Saito, and T. Suemoto. Time-resolved luminescence spectroscopy by the optical Kerr-gate method applicable to ultrafast relaxation processes. *Phys. Rev. B*, 62:10083–10087, 2000.
- [80] Desmond O’Connor. *Time-Correlated Single Photon Counting*. Academic Press, 2012.
- [81] M.I. Dyakonov and V.I. Perel. {CHAPTER} 2 - Theory of optical spin orientation of electrons and nuclei in semiconductors. In F. Meier and B.P. Zakharchenya, editors, *Optical Orientation*, volume 8 of *Modern Problems in Condensed Matter Sciences*, pages 11 – 71. Elsevier, 1984.
- [82] M. I. Dyakonov, editor. *Spin Physics in Semiconductors*, volume 157 of *Springer Series in Solid-State Science*. Springer, 2008.

- [83] G.E. Pikus and A.N. Titkov. {CHAPTER} 3 - spin relaxation under optical orientation in semiconductors. In F. Meier and B.P. Zakharchenya, editors, *Optical Orientation*, volume 8 of *Modern Problems in Condensed Matter Sciences*, pages 73 – 131. Elsevier, 1984.
- [84] M. W. Wu, J. H. Jiang, and M. Q. Weng. Spin dynamics in semiconductors. *Phys. Rep.*, 493(2–4):61 – 236, 2010.
- [85] I. Žutić, J. Fabian, and S. Das Sarma. Spintronics: Fundamentals and applications. *Rev. Mod. Phys.*, 76(2):323–410, 2004.
- [86] D. D. Awschalom, L. C. Bassett, A. S. Dzurak, E. L. Hu, and J. R. Petta. Quantum spintronics: Engineering and manipulating atom-like spins in semiconductors. *Science*, 339(6124):1174–9, 3 2013.
- [87] D. J. Hilton and C. L. Tang. Optical orientation and femtosecond relaxation of spin-polarized holes in GaAs. *Phys. Rev. Lett.*, 89:146601, 2002.
- [88] J. M. Kikkawa, I. P. Smorchkova, N. Samarth, and D. D. Awschalom. Room-temperature spin memory in two-dimensional electron gases. *Science*, 277(5330):1284–1287, 1997.
- [89] Y. Ohno, R. Terauchi, T. Adachi, F. Matsukura, and H. Ohno. Spin relaxation in GaAs(110) quantum wells. *Phys. Rev. Lett.*, 83(20):4196–4199, 1999.
- [90] R. Winkler. *Spin-orbit coupling effects in two-dimensional electron and hole systems*. Number 191. Springer, 2003.
- [91] M. Kohl, M. R. Freeman, D. D. Awschalom, and J. M. Hong. Femtosecond spectroscopy of carrier-spin relaxation in GaAs-Al_xGa_{1-x}As quantum wells. *Phys. Rev. B*, 44(11):5923, 1991.
- [92] T. Amand, B. Dareys, B. Baylac, X. Marie, J. Barrau, M. Brousseau, D. J. Dunstan, and R. Planel. Exciton formation and hole-spin relaxation in intrinsic quantum wells. *Phys. Rev. B*, 50(16):11624–11628, 1994.
- [93] S. Pfalz, R. Winkler, T. Nowitzki, D. Reuter, A. D. Wieck, D. Hägele, and M. Oestreich. Optical orientation of electron spins in GaAs quantum wells. *Phys. Rev. B*, 71(16):165305, 2005.
- [94] T. C. Damen, L. Viña, J. E. Cunningham, J. Shah, and L. J. Sham. Subpicosecond spin relaxation dynamics of excitons and free carriers in GaAs quantum wells. *Phys. Rev. Lett.*, 67(24):3432–3435, 1991.
- [95] L. Muñoz, E. Pérez, L. Viña, and K. Ploog. Spin relaxation in intrinsic GaAs quantum wells: Influence of excitonic localization. *Phys. Rev. B*, 51(7):4247–4257, 1995.
- [96] W. Yao, D. Xiao, and Q. Niu. Valley-dependent optoelectronics from inversion symmetry breaking. *Phys. Rev. B*, 77(23):235406, 2008.

- [97] B. Zhu, H. Zeng, J. Dai, Z. Gong, and X. Cui. Anomalously robust valley polarization and valley coherence in bilayer WS_2 . *Proc. Natl. Acad. Sci. U.S.A.*, 111(32):11606–11611, 2014.
- [98] Y. J. Zhang, T. Oka, R. Suzuki, J. T. Ye, and Y. Iwasa. Electrically switchable chiral light-emitting transistor. *Science*, 344(6185):725–728, 2014.
- [99] K. F. Mak, K. L. McGill, J. Park, and P. L. McEuen. The valley Hall effect in MoS_2 transistors. *Science*, 344(6191):1489–1492, 2014.
- [100] D. Lagarde, L. Bouet, X. Marie, C. R. Zhu, B. L. Liu, T. Amand, P. H. Tan, and B. Urbaszek. Carrier and polarization dynamics in monolayer MoS_2 . *Phys. Rev. Lett.*, 112(4):047401, 2014.
- [101] M. M. Glazov, T. Amand, X. Marie, D. Lagarde, L. Bouet, and B. Urbaszek. Exciton fine structure and spin decoherence in monolayers of transition metal dichalcogenides. *Phys. Rev. B*, 89(20):201302, 2014.
- [102] A. Splendiani, L. Sun, Y. B. Zhang, T. S. Li, J. Kim, C. Y. Chim, G. Galli, and F. Wang. Emerging photoluminescence in monolayer MoS_2 . *Nano Lett.*, 10(4):1271–1275, 2010.
- [103] K. F. Mak, C. Lee, J. Hone, J. Shan, and T. F. Heinz. Atomically thin MoS_2 : A new direct-gap semiconductor. *Phys. Rev. Lett.*, 105:136805, 2010.
- [104] P. Tonndorf, R. Schmidt, P. Böttger, X. Zhang, J. Börner, A. Liebig, M. Albrecht, C. Kloc, O. Gordan, D. R. T. Zahn, S. M. de Vasconcellos, and R. Bratschitsch. Photoluminescence emission and Raman response of monolayer MoS_2 , $MoSe_2$, and WSe_2 . *Opt. Express*, 21(4):4908–4916, 2013.
- [105] Yanhao Tang, Wei Xie, Krishna C. Mandal, John A. McGuire, and C. W. Lai. Optical and spin polarization dynamics in GaSe nanoslabs. *Phys. Rev. B*, 91:195429, 2015.
- [106] Yanhao Tang, Wei Xie, Krishna C. Mandal, John A. McGuire, and Chih Wei Lai. Exciton spin dynamics in GaSe. *Journal of Applied Physics*, 118(11):113103, 2015.
- [107] K. C. Mandal, A. Mertiri, G. W. Pabst, R. G. Roy, Y. Cui, P. Battacharya, M. Groza, A. Burger, A. M. Conway, and R. J. Nikolic. Layered III-VI chalcogenide semiconductor crystals for radiation detectors. In *Proc. SPIE*, volume 7079, page 70790O, 2008.
- [108] L. Pavesi, J. L. Staehli, and V. Capozzi. Mott transition of the excitons in GaSe. *Phys. Rev. B*, 39:10982–10994, 1989.
- [109] E. A. Donley, T. P. Heavner, F. Levi, M. O. Tataw, and S. R. Jefferts. Double-pass acousto-optic modulator system. *Review of Scientific Instruments*, 76(6):063112, 2005.
- [110] R. Le Toullec, N. Piccioli, M. Mejatty, and M. Balkanski. Optical constants of ϵ -GaSe. *II Nuovo Cimento B Series 11*, 38(2):159–167, 1977.

- [111] R. Le Toullec, N. Piccioli, and J. C. Chervin. Optical properties of the band-edge exciton in GaSe crystals at 10 k. *Phys. Rev. B*, 22:6162–6170, 1980.
- [112] N. Piccioli, R. Le Toullec, M. Mejatty, and M. Balkanski. Refractive index of GaSe between 0.45 μm and 330 μm . *Appl. Opt.*, 16(5):1236–1238, 1977.
- [113] Sadao Adachi and Yōichi Shindo. Optical constants of ϵ -GaSe. *Journal of Applied Physics*, 71(1):428–431, 1992.
- [114] S. Nüsse, P. Haring Bolivar, H. Kurz, V. Klimov, and F. Levy. Carrier cooling and exciton formation in GaSe. *Phys. Rev. B*, 56(8):4578–4583, 1997.
- [115] L. C. Andreani, F. Tassone, and F. Bassani. Radiative lifetime of free excitons in quantum wells. *Solid State Commun.*, 77(9):641–645, 1991.
- [116] D. E. Aspnes. Recombination at semiconductor surfaces and interfaces. *Surf. Sci.*, 132(1-3):406–421, 1983.
- [117] T. T. Zhang, P. Barate, C. T. Nguyen, A. Balocchi, T. Amand, P. Renucci, H. Carrere, B. Urbaszek, and X. Marie. L-valley electron spin dynamics in GaAs. *Phys. Rev. B*, 87(4):041201, 2013.
- [118] J. M. Luttinger and W. Kohn. Motion of electrons and holes in perturbed periodic fields. *Phys. Rev.*, 97(4):869, 1955.
- [119] E. O. Kane. Band structure of indium antimonide. *J. Phys. Chem. Solids*, 1(4):249–261, 1957.
- [120] G. Fishman and G. Lampel. Spin relaxation of photoelectrons in p-type gallium arsenide. *Phys. Rev. B*, 16(2):820, 1977.
- [121] K. Zerrouati, F. Fabre, G. Bacquet, J. Bandet, J. Frandon, G. Lampel, and D. Paget. Spin-lattice relaxation in p-type gallium arsenide single crystals. *Phys. Rev. B*, 37(3):1334–1341, 1988.
- [122] Z. G. Yu, S. Krishnamurthy, Mark van Schilfgaarde, and N. Newman. Spin relaxation of electrons and holes in zinc-blende semiconductors. *Phys. Rev. B*, 71(24):245312, 2005.
- [123] K. Shen and M. W. Wu. Hole spin relaxation in intrinsic and p-type bulk GaAs. *Phys. Rev. B*, 82(11):115205, 2010.
- [124] T. Amand and X. Marie. *Exciton Spin Dynamics in Semiconductor Quantum Wells*, pages 55–89. Springer, 2008.
- [125] P. Boross, B. Dóra, A. Kiss, and F. Simon. A unified theory of spin-relaxation due to spin-orbit coupling in metals and semiconductors. *Sci. Rep.*, 3:3233, 2013.
- [126] M. I. D’yakonov and V. I. Perel’. Spin orientation of electrons associated with the interband absorption of light in semiconductors. *Sov. Phys. JETP*, 33:1053, 1971.

- [127] M. I. D'yakonov and V. I. Perel'. Spin relaxation of conduction electrons in noncentrosymmetric semiconductors. *Sov. Phys. Solid State*, 13(12):3023–3026, 1972.
- [128] R. J. Elliott. Theory of the effect of spin-orbit coupling on magnetic resonance in some semiconductors. *Phys. Rev.*, 96(2):266–279, 1954.
- [129] Y. Yafet. *g Factors and Spin-Lattice Relaxation of Conduction Electrons*, volume 14 of *Solid State Physics*, pages 1–98. Academic Press, 1963.
- [130] G. L. Bir and G. E. Pikus. Optical orientation of excitons in uniaxial crystals. Large exchange splitting. *Sov. Phys. JETP*, 37:1116, 1973.
- [131] G. E. Pikus and G. L. Bir. Optical orientation of excitons in cubic crystals. *Sov. Phys. JETP*, 40(2):390–395, 1974.
- [132] G. L. Bir, A. G. Aronov, and G. E. Pikus. Spin relaxation of electrons due to scattering by holes. *Sov. Phys. JETP*, 42(4):705–712, 1975.
- [133] A. G. Aronov, G. E. Pikus, and A. N. Titkov. Spin relaxation of conduction electrons in p-type III-V compounds. *Sov. Phys. JETP*, 57:680, 1983.
- [134] F. Meier and B. P. Zakharchenya. Optical orientation. Elsevier, 1984.
- [135] J. Hu, L.-S. Li, W. Yang, L. Manna, L.-W. Wang, and A. P. Alivisatos. Linearly polarized emission from colloidal semiconductor quantum rods. *Science*, 292(5524):2060–2063, 2001.
- [136] J. Wang, M. S. Gudixsen, X. Duan, Y. Cui, and C. M. Lieber. Highly polarized photoluminescence and photodetection from single indium phosphide nanowires. *Science*, 293(5534):1455–1457, 2001.
- [137] J. C. Johnson, H. Yan, P. Yang, and R. J. Saykally. Optical cavity effects in ZnO nanowire lasers and waveguides. *J. Phys. Chem. B*, 107(34):8816–8828, 2003.
- [138] T. Takagahara. Effects of dielectric confinement and electron-hole exchange interaction on excitonic states in semiconductor quantum dots. *Phys. Rev. B*, 47(8):4569–4585, 1993.
- [139] D. Gammon, E. S. Snow, B. V. Shanabrook, D. S. Katzer, and D. Park. Homogeneous linewidths in the optical spectrum of a single gallium arsenide quantum dot. *Science*, 273(5271):87–90, 1996.
- [140] R. I. Dzhiyev, B. P. Zakharchenya, E. L. Ivchenko, V. L. Korenev, Y. G. Kusraev, N. N. Ledentsov, V. M. Ustinov, A. E. Zhukov, and A. F. Tsatsul'nikov. Optical orientation and alignment of excitons in quantum dots. *Phys. Solid State*, 40(5):790–793, 1998.
- [141] M. Paillard, X. Marie, P. Renucci, T. Amand, A. Jbeli, and J. M. Gerard. Spin relaxation quenching in semiconductor quantum dots. *Phys. Rev. Lett.*, 86(8):1634–1637, 2001.

- [142] Jon A. Schuller, Sinan Karaveli, Theanne Schiros, Keliang He, Shyuan Yang, Ioannis Kymissis, Jie Shan, and Rashid Zia. Orientation of luminescent excitons in layered nanomaterials. *Nat. Nano.*, 8(4):271–276, 2013.
- [143] A. M. Jones, H. Yu, N. J. Ghimire, S. Wu, G. Aivazian, J. S. Ross, B. Zhao, J. Yan, D. G. Mandrus, D. Xiao, W. Yao, and X. Xu. Optical generation of excitonic valley coherence in monolayer WSe₂. *Nature Nanotechnol.*, 8(9):634, 2013.
- [144] A. M. Jones, H. Yu, J. S. Ross, P. Klement, N. J. Ghimire, J. Yan, D. G. Mandrus, W. Yao, and X. Xu. Spin–layer locking effects in optical orientation of exciton spin in bilayer WSe₂. *Nat. Phys.*, 10(2):130–134, 2014.
- [145] M. Schlüter. The electronic structure of GaSe. *Nuovo Cimento B*, 13(2):313–360, 1973.
- [146] A. Bourdon and F. Khelladi. Selection rule in the fundamental direct absorption of GaSe. *Solid State Commun.*, 9(20):1715 – 1717, 1971.
- [147] A. Mercier, E. Mooser, and J. P. Voitchovsky. Near edge optical absorption and luminescence of GaSe, GaS and of mixed crystals. *J. Lumin.*, 7(0):241 – 266, 1973.
- [148] Yanhao Tang, Wei Xie, Krishna C. Mandal, John A. McGuire, and Chih Wei Lai. Linearly polarized remote-edge luminescence in GaSe nanoslabs. *Phys. Rev. Applied*, 4:034008, 2015.
- [149] D. Marcuse. *The Asymmetric Slab Waveguide*, pages 1–59. 1991.
- [150] T. Moriya and T. Kushida. Luminescence spectra due to exciton-exciton collisions in semiconductors. II. Stimulated emission spectra. *J. Phys. Soc. Jpn.*, 40(6):1676–1683, 1976.
- [151] P. Dey, J. Paul, G. Moody, C. E. Stevens, N. Glikin, Z. D. Kovalyuk, Z. R. Kudrynskiy, A. H. Romero, A. Cantarero, D. J. Hilton, and D. Karaiskaj. Biexciton formation and exciton coherent coupling in layered GaSe. *J Chem Phys*, 142(21):212422, 2015.
- [152] C. Weisbuch and B. Vinter. *Quantum Semiconductor Structures: Fundamentals and Applications*. Academic press, London, 1991.
- [153] R. Sooryakumar, D. S. Chemla, A. Pinczuk, A. C. Gossard, W. Wiegmann, and L. J. Sham. Valence band mixing in GaAs-(AlGa)As heterostructures. *Solid State Commun.*, 54(10):859–862, 1985.
- [154] R. Sooryakumar, A. Pinczuk, A. C. Gossard, D. S. Chemla, and L. J. Sham. Tuning of the valence-band structure of GaAs quantum wells by uniaxial stress. *Phys. Rev. Lett.*, 58(11):1150, 1987.
- [155] J. S. Weiner, D. S. Chemla, D. A. B. Miller, H. A. Haus, A. C. Gossard, W. Wiegmann, and C. A. Burrus. Highly anisotropic optical properties of single quantum well waveguides. *Appl. Phys. Lett.*, 47(7):664, 1985.

- [156] K. Ogawa, T. Katsuyama, and H. Nakamura. Polarization dependence of excitonic-polariton propagation in a GaAs quantum-well waveguide. *Phys. Rev. Lett.*, 64(7):796, 1990.
- [157] S. Pfalz, R. Winkler, N. Ubbelohde, D. Hägele, and M. Oestreich. Electron spin orientation under in-plane optical excitation in GaAs quantum wells. *Phys. Rev. B*, 86(16):165301, 2012.
- [158] S. Wu, S. Buckley, J. R. Schaibley, L. Feng, J. Yan, D. G. Mandrus, F. Hatami, W. Yao, J. Vučković, A. Majumdar, and X. Xu. Monolayer semiconductor nanocavity lasers with ultralow thresholds. *Nature*, 520(7545):69, 2015.
- [159] Yu Ye, Zi Jing Wong, Xiufang Lu, Xingjie Ni, Hanyu Zhu, Xianhui Chen, Yuan Wang, and Xiang Zhang. Monolayer excitonic laser. *Nat Photon*, 9(11):733–737, November 2015.
- [160] S. Schwarz, S. Dufferwiel, P. M. Walker, F. Withers, A. A. P. Trichet, M. Sich, F. Li, E. A. Chekhovich, D. N. Borisenko, N. N. Kolesnikov, K. S. Novoselov, M. S. Skolnick, J. M. Smith, D. N. Krizhanovskii, and A. I. Tartakovskii. Two-dimensional metal–chalcogenide films in tunable optical microcavities. *Nano Lett.*, 14(12):7003–7008, 2014.
- [161] X. Liu, T. Galfsky, Z. Sun, F. Xia, E-C Lin, Y-H Lee, S. Kéna-Cohen, and V. M. Menon. Strong light–matter coupling in two-dimensional atomic crystals. *Nat. Photon.*, 9(1):30–34, 2014.
- [162] X. Gan, Y. Gao, K. F. Mak, X. Y. R.-J. Shiue, A. van der Zande, M. E. Trusheim, F. Hatami, T. F. Heinz, J. Hone, and D. Englund. Controlling the spontaneous emission rate of monolayer MoS₂ in a photonic crystal nanocavity. *Appl. Phys. Lett.*, 103(18):181119, 2013.
- [163] S. Wu, S. Buckley, A. M. Jones, J. S. Ross, N. J. Ghimire, J. Yan, D. G. Mandrus, W. Yao, F. Hatami, J. Vučković, A. Majumdar, and X. Xu. Control of two-dimensional excitonic light emission via photonic crystal. *2D Mater.*, 1(1):011001, 2014.
- [164] C. Gärtner, C. Karnutsch, U. Lemmer, and C. Pflumm. The influence of annihilation processes on the threshold current density of organic laser diodes. *J. Appl. Phys.*, 101(2):023107, 2007.
- [165] B. E. Little and S. T. Chu. Toward very large-scale integrated photonics. *Opt. Photonics News*, 11(11):24, 2000.
- [166] R. Nagarajan, C. H. Joyner, Jr Schneider, R. P., J. S. Bostak, T. Butrie, A. G. Dentai, V. G. Dominic, P. W. Evans, M. Kato, M. Kauffman, D. J. H. Lambert, S. K. Mathis, A. Mathur, R. H. Miles, M. L. Mitchell, M. J. Missey, S. Murthy, A. C. Nilsson, F. H. Peters, S. C. Pennypacker, J. L. Pleumeekers, R. A. Salvatore, R. K. Schlenker, R. B. Taylor, H-S . S. Tsai, M. F. Van Leeuwen, J. Webjorn, M. Ziari, D. Perkins, J. Singh, S. G. Grubb, M. S. Reffle, D. G. Mehuys, F. A. Kish, and D. F. Welch. Large-scale photonic integrated circuits. *IEEE J. Sel. Top. Quantum Electron.*, 11(1):50–65, 2005.
- [167] R. G. Beausoleil. Large scale integrated photonics for twenty-first century information technologies. *Found. Phys.*, 44(8):856–872, 2014.

- [168] W. Jie, X. Chen, D. Li, L. Xie, Y. Y. Hui, S. P. Lau, X. Cui, and J. Hao. Layer-dependent nonlinear optical properties and stability of non-centrosymmetric modification in few-layer GaSe sheets. *Angew. Chem. Int. Ed.*, 54(4):1185–1189, 2015.
- [169] X. Zhou, J. Cheng, Y. Zhou, T. Cao, H. Hong, Z. Liao, S. Wu, H. Peng, K. Liu, and D. Yu. Strong second-harmonic generation in atomic layered GaSe. *J. Am. Chem. Soc.*, 137(25):7994–7997, 2015.
- [170] Yanhao Tang, Krishna C. Mandal, John A. McGuire, and Chih Wei Lai. Layer- and frequency-dependent second harmonic generation in reflection from GaSe atomic crystals. *Phys. Rev. B*, 94:125302, 2016.
- [171] Yuan Huang, Eli Sutter, Norman N. Shi, Jiabao Zheng, Tianzhong Yang, Dirk Englund, Hong-Jun Gao, and Peter Sutter. Reliable exfoliation of large-area high-quality flakes of graphene and other two-dimensional materials. *ACS Nano*, 9(11):10612–10620, 2015. PMID: 26336975.
- [172] m Mechler, Judit Kopniczky, Janos Kokavecz, Anders Hoel, Claes-Goran Granqvist, and Peter Heszler. Anomalies in nanostructure size measurements by afm. *Phys. Rev. B*, 72:125407, 2005.
- [173] P. Nemes-Incze, Z. Osvath, K. Kamaras, and L.P. Biro. Anomalies in thickness measurements of graphene and few layer graphite crystals by tapping mode atomic force microscopy. *Carbon*, 46(11):1435 – 1442, 2008.
- [174] Xiaobo Yin, Ziliang Ye, Daniel A. Chenet, Yu Ye, Kevin O’Brien, James C. Hone, and Xiang Zhang. Edge nonlinear optics on a MoS₂ atomic monolayer. *Science*, 344(6183):488–490, 2014.
- [175] G. Wang, X. Marie, I. Gerber, T. Amand, D. Lagarde, L. Bouet, M. Vidal, A. Balocchi, and B. Urbaszek. Giant enhancement of the optical second-harmonic emission of WSe₂ monolayers by laser excitation at exciton resonances. *Phys. Rev. Lett.*, 114:097403, 2015.
- [176] D. C. Haueisen and Herbert Mahr. Nonlinear electronic dispersion in CuCl. *Phys. Rev. Lett.*, 26:838–840, 1971.
- [177] M. Lafrentz, D. Brunne, A. V. Rodina, V. V. Pavlov, R. V. Pisarev, D. R. Yakovlev, A. Bakin, and M. Bayer. Second-harmonic generation spectroscopy of excitons in ZnO. *Phys. Rev. B*, 88:235207, 2013.
- [178] Nardeep Kumar, Sina Najmaei, Qiannan Cui, Frank Ceballos, Pulickel M. Ajayan, Jun Lou, and Hui Zhao. Second harmonic microscopy of monolayer MoS₂. *Phys. Rev. B*, 87:161403, 2013.
- [179] Yilei Li, Yi Rao, Kin Fai Mak, Yumeng You, Shuyuan Wang, Cory R. Dean, and Tony F. Heinz. Probing symmetry properties of few-layer MoS₂ and h-BN by optical second-harmonic generation. *Nano Lett.*, 13(7):3329–3333, 2013.

- [180] Leandro M. Malard, Thonimar V. Alencar, Ana Paula M. Barboza, Kin Fai Mak, and Ana M. de Paula. Observation of intense second harmonic generation from MoS₂ atomic crystals. *Phys. Rev. B*, 87:201401, 2013.
- [181] Robert W Boyd. Nonlinear Optics. In *Handbook of Laser Technology and Applications (Three-Volume Set)*, pages 161–183. Taylor & Francis, 2003.
- [182] B. F. Levine. Exciton contributions to the nonlinear optical susceptibility. *Phys. Rev. Lett.*, 33:368–371, 1974.
- [183] C. Hirlimann, J-F. Morhange, and A. Chevy. Excitonic resonant second harmonic in GaSe. *Solid State Communications*, 69(11):1019 – 1022, 1989.
- [184] K. Allakhverdiev, N. Akhmedov, Z. Ibragimov, Ş Ellialtıođlu, K. Lothar, and D. Haarer. Low-temperature second harmonic generation in gallium selenide under resonant excitation of the direct free excitons. *Solid State Communications*, 93(2):147–150, 1995.
- [185] R. Beaulac, L. Schneider, P. I. Archer, G. Bacher, and D. R. Gamelin. Light-induced spontaneous magnetization in doped colloidal quantum dots. *Science*, 325(5943):973–976, 2009.
- [186] C Jackson Stolle, Taylor B Harvey, and Brian A Korgel. Nanocrystal photovoltaics: A review of recent progress. *Current Opinion in Chemical Engineering*, 2(2):160 – 167, 2013.
- [187] Yasuhiro Shirasaki, Geoffrey J. Supran, Mounqi G. Bawendi, and Vladimir Bulovic. Emergence of colloidal quantum-dot light-emitting technologies. *Nat. Photon.*, 7(1):13–23, 2013.
- [188] Marcel Bruchez, Mario Moronne, Peter Gin, Shimon Weiss, and A. Paul Alivisatos. Semiconductor nanocrystals as fluorescent biological labels. *Science*, 281(5385):2013–2016, 1998.
- [189] H. X. Fu, L. W. Wang, and A. Zunger. Comparison of the k-p and the direct diagonalization approaches for describing the electronic structure of quantum dots. *Appl. Phys. Lett.*, 71(23):3433–3435, 1997.
- [190] A. L. Efros and M. Rosen. Comment on “Comparison of the k-p and the direct diagonalization approaches for describing the electron structure of quantum dots”. *Appl. Phys. Lett.*, 73(8):1155–1156, 1998.
- [191] H. X. Fu, L. W. Wang, and A. Zunger. Comment on "comparison of the k center dot p and the direct diagonalization approaches for describing the electron structure of quantum dots" - response. *Appl. Phys. Lett.*, 73(8):1157–1158, 1998.
- [192] H. X. Fu, L. W. Wang, and A. Zunger. Applicability of the k-p method to the electronic structure of quantum dots. *Phys. Rev. B*, 57(16):9971–9987, 1998.
- [193] M. Nirmal, D. J. Norris, M. Kuno, M. G. Bawendi, A. L. Efros, and M. Rosen. Observation of the dark exciton in CdSe quantum dots. *Phys. Rev. Lett.*, 75(20):3728–3731, 1995.

- [194] Yosuke Kayanuma. Quantum-size effects of interacting electrons and holes in semiconductor microcrystals with spherical shape. *Phys. Rev. B*, 38:9797–9805, 1988.
- [195] J. Voigt, F. Spiegelberg, and M. Senoner. Band parameters of CdS and CdSe single-crystals determined from optical exciton spectra. *Physica Status Solidi B-Basic Research*, 91(1):189–199, 1979.
- [196] K. Gong, Y. H. Zeng, and D. F. Kelley. Extinction coefficients, oscillator strengths, and radiative lifetimes of CdSe, CdTe, and CdTe/CdSe nanocrystals. *J. Phys. Chem. C*, 117(39):20268–20279, 2013.
- [197] Oliver Schmelz, Alf Mews, Thomas Basché, Andreas Herrmann, and Klaus Müllen. Supramolecular complexes from CdSe nanocrystals and organic fluorophors. *Langmuir*, 17(9):2861–2865, 2001.
- [198] Celso de Mello Donegá and Rolf Koole. Size dependence of the spontaneous emission rate and absorption cross section of CdSe and CdTe quantum dots. *J. Phys. Chem. C*, 113(16):6511–6520, 2009.
- [199] Jiatao Zhang, Yun Tang, Kwan Lee, and Min Ouyang. Tailoring light-matter-spin interactions in colloidal hetero-nanostructures. *Nature*, 466(7302):91–95, 2010.
- [200] Y. Tang, M. Saniepay, C. Mi, R. Beaulac, and J. A. McGuire. Optical stark metrology of CdSe quantum dots: Reconciling the size-dependent oscillator strength with theory. *arXiv:1703.00530*, 2017.
- [201] Lin-Wang Wang, , and Alex Zunger. High-energy excitonic transitions in CdSe quantum dots. *The Journal of Physical Chemistry B*, 102(34):6449–6454, 1998.
- [202] A. Franceschetti, H. Fu, L. W. Wang, and A. Zunger. Many-body pseudopotential theory of excitons in InP and CdSe quantum dots. *Phys. Rev. B*, 60:1819–1829, 1999.
- [203] T. Vossmeier, L. Katsikas, M. Giersig, I. G. Popovic, K. Diesner, A. Chemseddine, A. Eychmueller, and H. Weller. CdS nanoclusters: Synthesis, characterization, size dependent oscillator strength, temperature shift of the excitonic transition energy, and reversible absorbance shift. *The Journal of Physical Chemistry*, 98(31):7665–7673, 1994.
- [204] Tijana Rajh, Olga I. Micic, and Arthur J. Nozik. Synthesis and characterization of surface-modified colloidal cadmium telluride quantum dots. *The Journal of Physical Chemistry*, 97(46):11999–12003, 1993.
- [205] John Sundar Kamal, Abdoulghafar Omari, Karen Van Hoecke, Qiang Zhao, André Van-tomme, Frank Vanhaecke, Richard Karel Čapek, and Zeger Hens. Size-dependent optical properties of zinc blende cadmium telluride quantum dots. *J. Phys. Chem. C*, 116(8):5049–5054, 2012.

- [206] A. Striolo, J. Ward, J. M. Prausnitz, W. J. Parak, D. Zanchet, D. Gerion, D. Milliron, and A. P. Alivisatos. Molecular weight, osmotic second virial coefficient, and extinction coefficient of colloidal CdSe nanocrystals. *The Journal of Physical Chemistry B*, 106(21):5500–5505, 2002.
- [207] A. F. van Driel, G. Allan, C. Delerue, P. Lodahl, W. L. Vos, and D. Vanmaekelbergh. Frequency-dependent spontaneous emission rate from CdSe and CdTe nanocrystals: Influence of dark states. *Phys. Rev. Lett.*, 95:236804, 2005.
- [208] A.M. Bonch-Bruевич and V.A. Khodovoĭ. Current methods for the study of the Stark effect in atoms. *Soviet Physics Uspekhi*, 10(5):637, 1968.
- [209] Christophe Delerue Delerue and Michel Lannoo. *Nanostructures-Theory and Modeling*. Springer Berlin Heidelberg, 2004.
- [210] Poulami Dutta and Rémi Beaulac. Photoluminescence quenching of colloidal CdSe and CdTe quantum dots by nitroxide free radicals. *Chem. Mater.*, 28(4):1076–1084, 2016.
- [211] Z. Adam Peng and Xiaogang Peng. Formation of high-quality cdte, cdse, and cds nanocrystals using cdo as precursor. *Journal of the American Chemical Society*, 123(1):183–184, 2001. PMID: 11273619.
- [212] Monique Combescot and Roland Combescot. Optical Stark effect of the exciton: Biexcitonic origin of the shift. *Phys. Rev. B*, 40:3788–3801, 1989.
- [213] Monique Combescot. Optical Stark effect of the exciton. II. Polarization effects and exciton splitting. *Phys. Rev. B*, 41:3517–3533, 1990.
- [214] A. V. Rodina and A. L. Efros. Band-edge biexciton in nanocrystals of semiconductors with a degenerate valence band. *Physical Review B*, 82(12):125324, 2010.
- [215] P. Guyot-Sionnest and M. A. Hines. Intraband transitions in semiconductor nanocrystals. *Applied Physics Letters*, 72(6):686–688, 1998.
- [216] A. L. Efros and M. Rosen. Quantum size level structure of narrow-gap semiconductor nanocrystals: Effect of band coupling. *Phys. Rev. B*, 58(11):7120–7135, 1998.
- [217] A. Imamoğlu, D. D. Awschalom, G. Burkard, D. P. DiVincenzo, D. Loss, M. Sherwin, and A. Small. Quantum information processing using quantum dot spins and cavity QED. *Phys. Rev. Lett.*, 83:4204–4207, 1999.
- [218] Pochung Chen, C. Piermarocchi, L. J. Sham, D. Gammon, and D. G. Steel. Theory of quantum optical control of a single spin in a quantum dot. *Phys. Rev. B*, 69:075320, 2004.
- [219] C. E. Pryor and M. E. Flatté. Predicted ultrafast single-qubit operations in semiconductor quantum dots. *Appl. Phys. Lett.*, 88(23):233108, 2006.
- [220] M Kuno, M Nirmal, M.G. Bawendi, Alexander Efros, and Mervine Rosen. Magnetic circular dichroism study of CdSe quantum dots. *J. Chem. Phys.*, 108(10):4242–4247, 1998.

- [221] S. Tsuda and C.H. Brito Cruz. Femtosecond dynamics of the optical Stark effect in semiconductor-doped glass. *Appl. Phys. Lett.*, 68(8):1093–1095, 1996.
- [222] J. A. Gupta and D. D. Awschalom. Spin precession and the optical Stark effect in a semiconductor-doped glass. *Phys. Rev. B*, 63(8):085303, 2001.
- [223] R.C.C. Leite, E.A. Meneses, N. Jannuzzi, and J.G.P. Ramos. Carrier assisted radiative recombination of free excitons in GaSe. *Solid State Communications*, 11(12):1741 – 1744, 1972.
- [224] T. Ugmori, K. Masuda, and S. Namba. Spontaneous and stimulated emission in GaSe under intense excitation. *Solid State Communications*, 12(5):389 – 391, 1973.
- [225] A. Mercier and J. P. Voitchovsky. Exciton-exciton and exciton-carrier scattering in GaSe. *Phys. Rev. B*, 11:2243–2250, 1975.
- [226] S. H. Wei and A. Zunger. Calculated natural band offsets of all II-VI and III-V semiconductors: Chemical trends and the role of cation d orbitals. *Appl. Phys. Lett.*, 72(16):2011–2013, 1998.
- [227] T. Z. Markus, M. Wu, L. Wang, D. H. Waldeck, D. Oron, and R. Naaman. Electronic structure of CdSe nanoparticles adsorbed on Au electrodes by an organic linker: Fermi level pinning of the HOMO. *J. Phys. Chem. C*, 113(32):14200–14206, 2009.
- [228] L. W. Wang and A. Zunger. Pseudopotential calculations of nanoscale CdSe quantum dots. *Phys. Rev. B*, 53(15):9579–9582, 1996.
- [229] S. Logothetidis, M. Cardona, P. Lautenschlager, and M. Garriga. Temperature-dependence of the dielectric function and the interband critical-points of CdSe. *Phys. Rev. B*, 34(4):2458–2469, 1986.